## *Exploring Holographic Chaos and Complexity*

REYNOLDS, ALAN,PAUL

# Exploring Holographic Chaos and Complexity

Alan Paul Reynolds

A Thesis presented for the degree of
Doctor of Philosophy


Department of Mathematical Sciences
Durham University
United Kingdom

June 2018

# Exploring Holographic Chaos and Complexity

Alan Paul Reynolds

Submitted for the degree of Doctor of Philosophy
June 2018

**Abstract:** In principle, holography provides a well-defined non-perturbative formulation of quantum gravity, but to really use it to address questions about the nature of spacetime, we need to understand the emergence of the bulk spacetime from the dual field theory description. A number of field theory properties are believed to be dual to aspects of the geometry, ranging from simple two-point correlation functions, known to be approximately dual to the length of geodesics, to the quantum complexity, which is conjectured to be dual to either the size of a maximal volume slice of the bulk, or to the action of a patch of the bulk spacetime.

In this thesis, we use the duality between correlation functions and geodesics (and to a lesser extent, that between entanglement entropy and bulk surfaces proposed by Ryu and Takayanagi) to extend a holographic analysis of quantum chaos initiated by Shenker and Stanford. We then explore the more speculative holographic complexity conjectures, analysing the divergence of complexity in general and testing the conjectures in a number of specific spacetimes. For certain cases, we obtain qualitatively different results for the two conjectures, raising questions for future research.

# Declaration

The work in this thesis is based on research carried out in the Department of Mathematical Sciences at Durham University. The results are based on the following collaborative works:

- Alan P. Reynolds and Simon F. Ross. Butterflies with rotation and charge. *Class. Quant. Grav.*, 33:215008, 2016, `arXiv:1604.04099`
- Alan Reynolds and Simon F. Ross. Divergences in holographic complexity. *Class. Quant. Grav.*, 33:105004, 2017, `arXiv:1612.05439`
- Alan P. Reynolds and Simon F. Ross. Complexity in de Sitter space. *Class. Quant. Grav.*, 34:175013, 2017, `arXiv:1706.03788`
- Alan P. Reynolds and Simon F. Ross. Complexity of the AdS soliton. *Class. Quant. Grav.*, 35:095006, 2018, `arXiv:1712.03732`

No part of this thesis has been submitted elsewhere for any degree or qualification.

# Acknowledgements

I would like to thank Simon for his patience in supervisions and Corrin for her patience the rest of the time.

# Contents

# Chapter 1

# Introduction

## 1.1 AdS/CFT and bulk reconstruction

Since the introduction of the AdS/CFT correspondence by Maldacena [50], researchers have sought to use the tools of gauge/gravity duality, or holography, to provide insight into a range of physical phenomena[1]. On the one hand, the duality may be used to rephrase questions in strongly coupled quantum systems (including condensed matter systems that might be realised in the laboratory) in terms of a more computationally tractable, weakly coupled, gravitational theory [35]. On the other hand, we may attempt to use knowledge of the boundary field theory (which does not explicitly involve gravity), to tackle questions in quantum gravity. The research outlined herein belongs in this second category, with particular focus on the relationship between the geometry of the gravitational theory and the properties of the dual field theory.

In its original setting, the strongest form of the AdS/CFT correspondence posits a complete correspondence between type II-B string theory on $\mathrm{AdS}_5 \times \mathrm{S}_5$ and $N = 4$ Super Yang-Mills — a conformal theory (CFT) — in 4 dimensions. It is conjectured that such a correspondence applies more generally, i.e. that given a theory of quantum gravity on $\mathrm{AdS}_{d+1} \times X$, where $X$ is some compact, positively curved, Einstein manifold, then this is dual to a CFT in $d$ dimensions. Performing Kaluza-Klein reduction on the compact ($\mathrm{S}_5$ or $X$) dimensions, the conformal theory may be (loosely) considered to live on the boundary of the remaining AdS spacetime. Hence, as is standard, the AdS spacetime will be referred to as the 'bulk', with the gravitational (string) theory being the 'bulk theory', while the CFT will be referred to as the 'boundary' theory. Typically, the boundary theory is considered as living in flat Minkowski space, though as will be seen in chapter 4, we may consider other

[1] In addition to the original research papers, the student of gauge/gravity duality may now refer to two textbooks [4, 57] and a number of overview papers [44, 56, 39, 61, 56, 24]

boundary spacetimes. In either case, the boundary theory is not gravitational, that is, the boundary spacetime merely provides the theatre in which the boundary theory acts and is not a dynamic object in its own right.

Researchers in AdS/CFT refer to the still growing 'holographic dictionary' that relates properties of one theory to the other. A basic entry in the holographic dictionary indicates a correspondence between fields in the bulk and (sources for) local operators in the field theory. In particular, a scalar field $\phi$ in the bulk is dual to (a source for) a scalar primary operator $\mathcal{O}$ on the boundary. The mass, $m$, of the scalar field is related to the scaling dimension, $\Delta$, of the operator via

$$\Delta = \frac{d}{2} + \sqrt{\frac{d^2}{4} + m^2 l^2}, \tag{1.1.1}$$

where $l$ is the AdS radius and $d$ is the dimensionality of the boundary theory [85]. The boundary condition for the bulk scalar field is given, up to a divergent factor, by the source for the operator on the boundary. In detail, in Poincaré coordinates where $z \to 0$ denotes the boundary,

$$\phi(z, x) \to z^{d-\Delta}\phi_0(x) \text{ as } z \to 0, \tag{1.1.2}$$

where $\phi_0$ is a source for operator $\mathcal{O}$, i.e.

$$\mathcal{L}_{\text{CFT}} = \mathcal{L}_0 + \int d^d x\, \phi_0(x)\mathcal{O}(x). \tag{1.1.3}$$

The relationship between correlators in the bulk and on the boundary can be inferred from the equivalence of the partition functions, proposed by Witten [85] and Gubser et al. [31]:

$$Z_{\text{CFT}}(\phi_0) = Z_{\text{string}}(\phi, \phi_0) \simeq e^{-S_{\text{sugra}}(\phi,\phi_0)}. \tag{1.1.4}$$

Here $\phi$ gives the bulk field solution satisfying the boundary conditions (1.1.2) imposed by the boundary source $\phi_0$. The intractability of the second expression here leads us to consider a limiting case where the string theory is approximated by classical supergravity, giving the third expression. This leads [10] to two-point correlation functions in the field theory being related to those in the bulk (anchored at two points on the cutoff surface $z = \epsilon$), via

$$\langle \mathcal{O}(x_1)\mathcal{O}(x_2)\rangle = \epsilon^{-2\Delta} \langle \phi(x_1, \epsilon)\phi(x_2, \epsilon)\rangle \,. \tag{1.1.5}$$

For non-causally related points, the semi-classical, leading order approximation to the right hand side is then given by a sum over geodesics [49]

$$\langle \phi(x_1, \epsilon)\phi(x_2, \epsilon)\rangle = \sum_g e^{-L_g\Delta}, \tag{1.1.6}$$

where $g$ runs over the geodesics connecting $(x_1, \epsilon)$ and $(x_2, \epsilon)$ and $L_g$ is the geodesic length. This is then dominated by the shortest geodesic when the field mass $m$ (and hence scaling dimension $\Delta$) is large.

The relationship between correlators in the CFT and geodesic length in the bulk marks the start of attempts to reconstruct bulk geometry from properties of the dual field theory, and is used in chapter 2 in the context of quantum chaos, where a small perturbation in the distant past can have a significant impact on correlation functions and hence, it must be inferred, on the geometry of the bulk solution. A second such relationship considered here is that proposed by Ryu and Takayanagi [70, 69] and extended by Hubeny et al. [40], whereupon the entanglement entropy of a region, $A$, in the boundary theory is proposed to be related to the area of a particular co-dimension 2 surface in the bulk. Given a state in the field theory represented by the density matrix $\rho$, the entanglement entropy of a region $A$ provides a measure of the 'amount of entanglement' between $A$ and its complement $B = A^C$, provided the state $\rho$ is pure. It is given by the von-Neumann entropy of the reduced density matrix $\rho_A$, i.e.

$$S_A = -\operatorname{tr}_A \rho_A \log \rho_A, \tag{1.1.7}$$

where $\rho_A = \operatorname{tr}_B \rho$. Direct calculation of this quantity is far from straightforward, involving the calculation of related quantities — the Renyi entropies — via the calculation of path integrals over a Riemann surface consisting of multiple sheets, carefully stitched together, followed by the application of analytic continuation and the taking of a limit. This is referred to as the 'replica trick' [19]. The proposal, by Ryu and Takayanagi [70, 69], that this complex calculation might be replaced by the determination of a minimal surface in the bulk therefore offered a considerable simplification. In the original proposal, the bulk spacetime is presumed to be static and the required surface is the minimal (co-dimension 1) surface in the timeslice of the bulk that has the boundary $\partial A$ and that is homologous to $A$, as shown in figure 1.1. Entanglement entropy is then given by

$$S_A = \frac{\text{Area}(\gamma(A))}{4G_{\text{N}}}, \tag{1.1.8}$$

where $\gamma(A)$ is the minimal surface. Hubeny et al. [40] produce a covariant version of holographic entanglement entropy, valid for non-static spacetime, by considering co-dimension 2 surfaces in the bulk as a whole but otherwise satisfying the same conditions.[2]

For reasons to be described in section 1.3, the correspondences between geometric

[2]Note that, for $2+1$ dimensional bulk spacetimes such as those considered in chapter 2, the minimal co-dimension 2 surfaces are, again, simply geodesics.

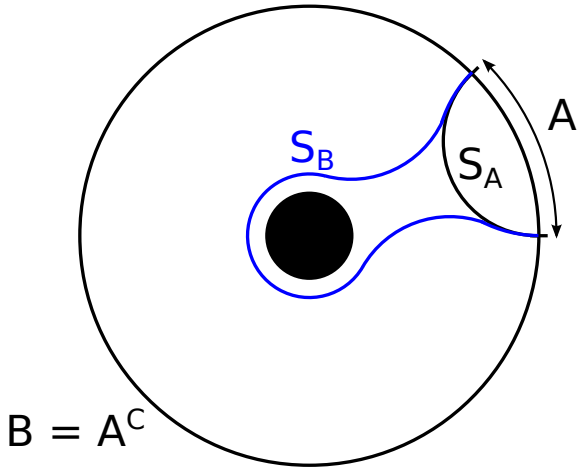


Figure 1.1: Schematic diagram of the minimal surfaces used in the calculation of entanglement entropy. Without the black hole, the surface, labelled $S_A$, that gives the entanglement entropy of $A$ would also be the correct surface for $B = A^C$. However, with the presence of the black hole, this surface is not homologous to $B$ and hence a larger surface must be selected.

objects in the bulk and properties of the field theory described thus far were found to be insufficient for bulk reconstruction. Certain properties of the bulk spacetime, in particular the increasing behind-the-horizon volume of the bulk spacetime for black hole solutions, could not be explained using two-point correlation functions and entanglement entropy. This led to the more speculative complexity conjectures first suggested by Susskind [81], who conjectured that there may be a relation between the bulk geometry and the complexity of the dual boundary state. Here, the quantum computational complexity of a state is loosely defined as the minimal number of quantum gates required to construct the state from some specified simple state. This conjecture was refined, first into the complexity-volume (CV) conjecture, where the complexity is supposed to be dual to the volume of a co-dimension 1 surface in the bulk [79, 83, 82] and then into the alternative complexity-action (CA) conjecture, where the holographic complexity is given by the action of a co-dimension 0 patch of the spacetime [18, 17]. These complexity conjectures are described in more detail in section 1.3.

This thesis summarizes our research into different aspects of the relationships, described briefly above, between geometric properties of the bulk spacetime and properties of the field theory state on the boundary. The first component of this research, introduced in section 1.2 and described in detail in chapter 2, involves an extension of the work of Shenker and Stanford [72] in holographic chaos — a study of how chaotic effects in the field theory are mirrored in the dual bulk solution. The second, larger component, explores the holographic complexity conjectures in a

number of different spacetimes, where we obtained apparently contradictory results. An introduction to the complexity conjectures is given in section 1.3, with our research presented in detail in chapters 3–5.

## 1.2 Scrambling, chaos and holography

In gauge/gravity duality, black hole bulk solutions are dual to thermal states in the boundary field theory [85]. For example, the BTZ black hole is dual to the thermofield double state (TFD) — a pure but entangled state on two copies of a CFT, described in more detail in chapter 2 [51, 41]. While the overall state is pure, the density matrix produced by considering only a single copy of the CFT is that of the thermal state, i.e. $\frac{1}{Z}\sum_i e^{-\beta E_i} |E_i\rangle \langle E_i|$. Such systems exhibit the property of 'scrambling' [71]. Starting from a state that is, in some way, 'special', time evolution results in a change to more disordered 'typical' states.

Of course, to refine this definition of scrambling, we need to describe what is meant by 'typical' and 'special' states. Indeed, in some sense, every state has some distinguishing property, so it is perhaps better, initially, to consider typical *properties* of states. That is, properties that one expects, with high probability, a randomly selected state (according to an appropriate measure) to possess. Here, where we consider purifications of the thermal state, a key such property is that density matrices for small subsystems (by which we mean any subsystem smaller than half the whole system) are approximately thermal and the associated von-Neumann entropy is maximized. Distinguishing two such randomly selected states requires (with high probability) an observable that probes at least half of the degrees of freedom.

The concept of scrambling is well illustrated by the thermofield double state, dual to the BTZ black hole. At time $t = 0$, the state exhibits an unusual, local entanglement structure, in that small subsystems of the two CFTs may be found to be highly entangled. This special structure is revealed in calculations of the mutual information

$$I(A;B) = S_A + S_B - S_{A\cup B} \tag{1.2.1}$$

of the two subsystems [37] and in calculations of two point correlation functions between the two CFTs. For a randomly selected purification of the thermal state, one would expect both the mutual information of small subsystems and the two point correlation functions to be close to zero, while for the TFD this is not the case. However, this atypical entanglement structure is destroyed under time evolution, as the state evolves into a more typical purification of the thermal state.

It is conjectured that black holes are the fastest 'scramblers' in nature [36, 71, 80,

45]. The scrambling time is roughly defined to be the time required to render the density matrix of a small subsystem $A$, in a state such as the TFD, thermal. The scrambling time, for the fastest scramblers, is conjectured to be $t_s = \beta \log S$, where $S$ is the entropy of the system.

One may also consider evolving such states backward in time, in which case a special state such as the TFD, still evolves into a more disordered 'typical' state, $|\psi\rangle$. At least, the state $|\psi\rangle$ *appears* to be a typical state until one evolves forward in time, whereupon the special structure of the TFD at $t = 0$ is again revealed. One may think of the state $|\psi\rangle$ as being very carefully set up so as to produce the TFD upon applying time evolution. However, it is difficult to distinguish (without evolving forward in time) such a state from other typical states that apparently change very little over time — as discussed above, one requires an observable that probes at least half of the degrees of freedom. Hence there is the sensitive dependence on initial conditions that is referred to as chaos. Applying the smallest perturbation to the state at a point far enough in the past can destroy the special features of the state at $t = 0$.

In the context of gauge/gravity duality, this chaotic behaviour in the boundary field theory must be mirrored, in some way, in the bulk spacetime. However, it is initially surprising that a small perturbation in the bulk, near the boundary, could possibly lead to changes to the bulk geometry sufficient to significantly affect the geodesics and extremal surfaces dual to the two-point correlators and entanglement entropy of the field theory. A closer examination, performed by Shenker and Stanford [72], reveals that, in the $t = 0$ frame in the bulk, the quanta released in the distant past at the boundary have exponentially blue-shifted energy. The result is a shock-wave geometry [26], with an associated lengthening of the wormhole resulting in the decay of the correlations and local entanglement.

In chapter 2, we extend the results of Shenker and Stanford [72] to consider the behaviour in the presence of chemical potentials for charge or angular momentum. This means considering charged or rotating black holes in the bulk. We wished to explore the question of how the chaotic effects would be modified by the presence of the additional scale introduced. In particular, if chaos is signalled, in the bulk, by the lengthening of the wormhole, how would this be affected in the cases where the wormhole is already long, for example, when considering near-extremal charged or rotating black holes?

Motivation for examining holographic chaos may be fairly direct — one may wish to determine what holography can tell us about quantum chaos. For example, Maldacena et al. [54] use holography to propose a bound on the rate of growth of chaos in thermal quantum systems. Alternatively, one's motivation may be less direct. From the publication of Shenker and Stanford's paper [72], research into quantum

chaos has been linked to research into the firewall proposal [3, 2]. As summarized by Shenker and Stanford, Almheiri et al. "argue that the existence of a smooth region connecting the outside and inside of the horizon requires special entanglement of degrees of freedom on the two sides. But during the evaporation of the black hole the system scrambles, and these delicate correlations are destroyed. No smooth region can remain." Subsequent work [73] is also linked to the ER = EPR conjecture of Maldacena and Susskind [53]. While Marolf and Polchinski [55] argued that, for truly typical, highly entangled states, the small correlations (of order $e^{-S}$) between the two field theories could not be interpreted geometrically, Shenker and Stanford [73] attempt to create such a state via the application of multiple perturbations to the TFD. While the resulting state has features that makes it atypical, the small correlations are explained by the extremely long wormhole that results from the perturbations.

## 1.3 Holographic complexity

As briefly mentioned above, the duality between minimal surfaces in the bulk and the entanglement entropy of regions in the boundary field theory may be insufficient for the purposes of bulk reconstruction. In this section, we briefly outline two reasons for this: entanglement shadows and the growth, behind the horizon, of Einstein-Rosen bridges. While the first issue might be solvable through considerations of properties closely related to entanglement, such as entwinement [8], the second issue led directly to the consideration of computational complexity by Susskind [81]. This section then proceeds to provide the details of the holographic complexity conjectures required for the subsequent chapters 3–5.

An entanglement shadow is simply a region of the bulk spacetime that is not probed by the minimal surfaces described by the Ryu-Takayanagi proposal. A simple (though perhaps somewhat artificial) example, given by [8], is provided by the bulk spacetime $AdS_3/\mathbb{Z}_n$ and is illustrated, for $n = 3$ in figure 1.2. Here, entanglement surfaces for small regions are as for $AdS_3$, but for larger regions, an alternative smaller surface becomes available, connecting the right hand boundary with a copy of the left hand boundary in an adjacent copy of the spacetime. The result is that certain minimal surfaces for $AdS_3$, required if the aim is to cover the spacetime, become non-minimal for $AdS_3/\mathbb{Z}_3$, with the result that an entanglement shadow is present. While this is an artificial example, such shadows also occur in more natural situations, such as in AdS black holes and the BTZ spacetime [27].

Proposals for penetrating such shadows include the idea of entwinement [8], that is, considering not just entanglement between spatial regions (as the the Ryu-

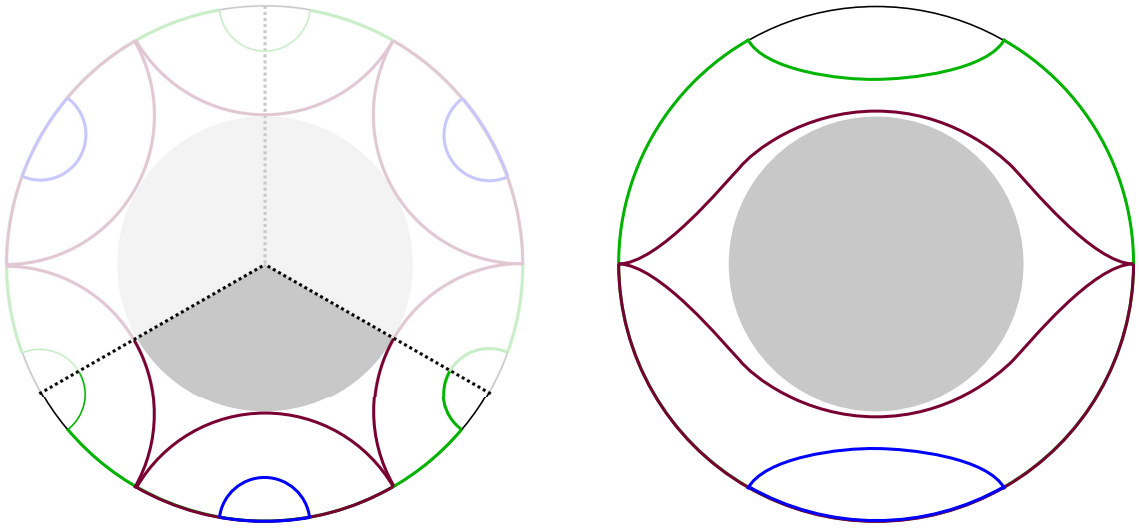

Figure 1.2: Entanglement surfaces in $AdS_3/\mathbb{Z}_3$. The left hand diagram shows the entanglement surfaces of $AdS_3/\mathbb{Z}_3$ but in the covering space $AdS_3$, while the right hand diagram illustrates just $AdS_3/\mathbb{Z}_3$. For the small blue region, the entangling surface is the same as that one would obtain in plain $AdS_3$. As the region is increased in size, becoming the red region (partially obscured by the blue), an alternative minimal surface appears, with the right boundary of the region being connected to the identification of the left boundary in an adjacent copy of the spacetime. For larger regions, such as that in green, this becomes the smaller surface. The result is an entanglement shadow, shown in grey.

Takayanagi proposal) but also between internal degrees of freedom. However, a possibly greater challenge is posed by the continued growth of Einstein-Rosen bridges. In, for example, the case of the Schwarzschild-AdS black hole, the volume of the Einstein-Rosen bridge continues to grow linearly, long after the boundary field theory has thermalized and hence ceased to evolve in any obvious way. So Susskind [81] asked the question, what is dual to this volume increase? It cannot be the entanglement entropy (or indeed entwinement) as this becomes maximal as the boundary theory thermalizes. A more subtle measure of the scrambling of quantum information is required. The suggestion is that quantum computational complexity — the minimum number of quantum gates required to produce the state from some simple, unentangled reference state — satisfies the requirements. In particular, it can continue to increase linearly after thermalization.

This proposal was later refined by Stanford and Susskind [79] into the conjecture that the computational complexity, $\mathcal{C}$, of the boundary state at a given time — i.e. on some spacelike slice $\Sigma$ of the boundary — could be identified with the volume, $V$, of the maximal co-dimension 1 spacelike slice, $B$, in the bulk ending on the boundary

slice,

$$\mathcal{C}_{\mathrm{V}} \propto \frac{V(B)}{G_{\mathrm{N}} l_{\mathrm{AdS}}}. \tag{1.3.1}$$

This is commonly referred to as the complexity-volume, or CV conjecture, further developed by Susskind and Zhao [83] and Susskind [82]. Note that this measure of holographic complexity has a UV divergence proportional to the volume of $\Sigma$, in much the same way that the holographic entanglement entropy of a region $A$ has a divergence proportional to the size of the boundary of $A$. Earlier analyses of the complexity conjectures considered the rate of increase of the complexity, the calculation of which resulted in the elimination of this divergence. Comparison of this rate of increase with a proposed bound [48, 17],

$$\frac{d\mathcal{C}}{dt} \leq \frac{2M}{\pi\hbar}, \tag{1.3.2}$$

expected to be saturated in the case of black hole spacetimes, provided evidence for the veracity of the CV proposal. The structure of the divergences in the complexity calculation were, comparatively, ignored. Here, however, in chapter 3, we consider the divergences more seriously, both as a physical component of the field theory complexity (just as divergences in holographic entanglement entropy can be identified with a physical UV contribution in the field theory) and because we will explore, in chapter 4, situations where the cancellation of divergences in the calculation of the rate of change of complexity no longer occurs.

More recently [18, 17], an alternative conjecture, referred to as the complexity-action or CA conjecture, was proposed. This identifies the complexity of a state in the boundary field theory with the action of the Wheeler-DeWitt (WdW) patch: the domain of development of the slice $B$ considered previously, illustrated in figure 1.3. The proposal is that

$$\mathcal{C}_{\mathrm{A}} = \frac{S_{\mathrm{W}}}{\pi\hbar},$$

where $S_{\mathrm{W}}$ is the action of the Wheeler-DeWitt patch. This proposal has the advantage that it is more universal, containing no explicit reference to any bulk length scale. It may also be easier to calculate, as there is no maximization problem to solve — finding the Wheeler-DeWitt patch is easier than finding the maximal volume timeslice.

While we avoid the task of solving a maximization problem, until recently it was not known how to determine the appropriate boundary terms of the action for null boundaries and for corners between boundaries when one or both are null. Clearly, the action of the WdW patch will include both such terms. Inspired by the CA proposal, Lehner et al. [46] constructed a prescription for the action including such terms, by requiring that the variation of the action vanish on-shell when the

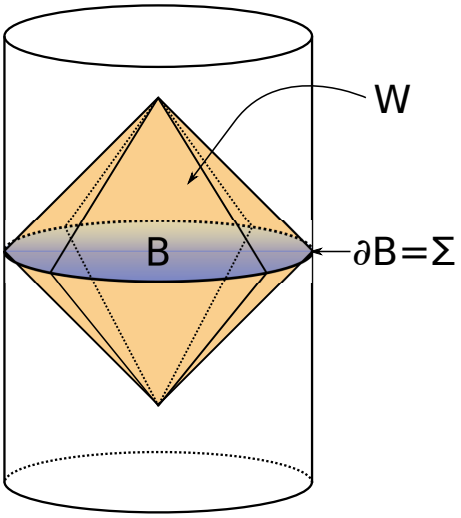


Figure 1.3: The maximal co-dimension 1 surface, $B$ (in blue), and the Wheeler-DeWitt patch, $W$ (in orange), in global AdS. The maximal surface is anchored on the boundary timeslice we wish to calculate the complexity for, while the WdW patch is the domain of development of $B$.

variation of the metric vanishes on the boundary of the region. The resulting form for the action for a general region, with timelike, spacelike and null boundaries, is

$$S_{\mathcal{V}} = \int_{\mathcal{V}} (R - 2\Lambda)\sqrt{-g}\, dV + 2\sum_{T_i} \int_{T_i} K\, d\Sigma + 2\sum_{S_i} \text{sign}(S_i) \int_{S_i} K\, d\Sigma$$
$$- 2\sum_{N_i} \text{sign}(N_i) \int_{N_i} \kappa\, dS\, d\lambda + 2\sum_{j_i} \text{sign}(j_i) \oint \eta_{j_i}\, dS + 2\sum_{m_i} \text{sign}(m_i) \oint a_{m_i}\, dS. \tag{1.3.3}$$

In this expression

- $T_i$ and $S_i$ are respectively timelike and spacelike components of the boundary of the region $\mathcal{V}$, and $K$ is the trace of the extrinsic curvature of the boundary. For $T_i$, the normal is taken outward-directed from $\mathcal{V}$. For $S_i$, the normal is always taken future-directed, and $\text{sign}(S_i) = 1(-1)$ if $\mathcal{V}$ lies to the future (past) of $S_i$, that is if the normal vector points into (out of) the region of interest.
- $N_i$ are null components of the boundary of $\mathcal{V}$, $\lambda$ is a parameter on null generators of $N_i$, increasing to the future, $dS$ is an area element on the cross-sections of constant $\lambda$, and $k^\alpha \nabla_\alpha k^\beta = \kappa k^\beta$, where $k^\alpha = \partial x^\alpha / \partial \lambda$ is the tangent to the generators. $\text{sign}(N_i) = 1(-1)$ if $N_i$ lies to the future (past) of $\mathcal{V}$.
- $j_i$ are junctions between non-null boundary components, where $\eta$ is the logarithm of the dot product of normals. We do not give the rules in detail as such junctions do not occur for Wheeler-DeWitt patches; see Lehner et al. [46] for full detail.

- $m_i$ are junctions where one or both of the boundary components are null. We have a null surface with future-directed tangent $k^\alpha$ and either a spacelike surface with future directed unit normal $n^\alpha$, a timelike surface with outward directed unit normal $s^\alpha$, or another null surface with future-directed tangent $\bar{k}^\alpha$, and

$$a = \begin{cases} \ln|k \cdot n| \\ \ln|k \cdot s| \\ \ln|k \cdot \bar{k}/2| \end{cases} \tag{1.3.4}$$

  respectively. We set $\text{sign}(m_i) = +1$ if $\mathcal{V}$ lies to the future (past) of the null boundary component and $m_i$ is at the past (future) end of the null component, and $\text{sign}(m_i) = -1$ otherwise.

While this action is diffeomorphism invariant under changes of coordinates in the bulk and on the timelike and spacelike boundaries, Lehner et al. [46] show that it depends on the choice of coordinate $\lambda$ on the null boundary components. This coordinate dependence seems a highly undesirable feature. Fortunately, they also found that the coordinate dependence could be eliminated by adding to the action a term

$$\Delta S = -2 \sum_{N_i} \text{sign}(N_i) \int_{N_i} \Theta \ln|c\Theta| dS d\lambda, \tag{1.3.5}$$

where $\Theta$ is the expansion of the null generators of $N_i$,

$$\Theta = \frac{1}{\sqrt{\gamma}} \frac{\partial \sqrt{\gamma}}{\partial \lambda}, \tag{1.3.6}$$

$\gamma$ is the metric on the cross-sections of constant $\lambda$ and $c$ is a constant. We will therefore use $S = S_{\mathcal{V}} + \Delta S$ as our definition of the action for a region with null boundaries. We will find, in chapter 3, that the adoption of this counterterm will also result in additional advantages.

Note that, due to the presence of the constant $c$, the counterterm does not remove all ambiguity from the action. Alternatively, as noted by Lehner et al. [46], there is a freedom to add an arbitrary function independent of the bulk metric to $a_{m_i}$. We see this as a subcase of a general freedom in the action: the requirement that the variation of the action vanish fixes the form of the boundary terms only up to contributions whose variations vanish under variations of the metric. Since the metric variation vanishes on the boundary, this includes the freedom to add arbitrary functions of the intrinsic geometry of the boundary. If we ignored the requirement of coordinate independence, this freedom would include the freedom to add terms like (1.3.5), as its variation under metric variations (with the metric fixed on the boundary) vanishes. Since we want to insist on coordinate independence, the coefficient in (1.3.5) is fixed, but we still have freedom to add terms which are scalars

on the null boundary, such as $\int_{N_i} \Theta f(\gamma)\, dS\, d\lambda$, where $f(\gamma)$ is any scalar function of the cross-section metric $\gamma$ and curvature invariants built from this metric such as its Ricci scalar. Also we have the freedom to add such scalar terms at the corners.

As with the CV conjecture, the CA conjecture produces a holographic complexity that is UV divergent. The nature of this divergence and the interplay between the divergence structure and the presence of the counterterm in the action are described in detail in chapter 3.

Given the recent introduction of the complexity conjectures and the existence of two different forms of conjecture, it seemed natural to test the conjectures in previously unconsidered scenarios. In particular, we explored the application of the conjectures for asymptotically AdS spacetimes in a de Sitter slicing, and hence a de Sitter boundary rather than a flat one. The results of this exploration are described in detail in chapter 4, after the examination of divergences, presented in chapter 3, that this work required. The nature of these results, in particular the unexpected quantitative differences between the CV and CA results obtained for 'bubble of nothing' spacetimes, led us to attempt to replicate the findings in a simpler scenario: that of the AdS soliton. The holographic complexity calculations for the AdS soliton are given in detail in chapter 5. This includes an attempt to calculate complexity directly in the field theory — a fermionic theory on a torus with antiperiodic boundary conditions in one direction — based on the circuit complexity work of Jefferson and Myers [42].

# Chapter 2

# The Butterfly Effect for Rotating and Charged Black Holes

## 2.1 Introduction

Recent holographic studies [72, 73, 54] have produced new insights regarding quantum chaos and the behavior of entanglement in near-thermal systems. In particular, Shenker and Stanford [72] examined how a perturbation, applied at some early time, affects the entanglement structure of the thermofield double (TFD) state,

$$|\psi\rangle = \frac{1}{\sqrt{Z}} \sum_i e^{-\beta E_i/2} \, |E_i\rangle_{\mathrm{L}} \otimes |E_i\rangle_{\mathrm{R}} \, . \tag{2.1.1}$$

This is a state over two entangled quantum subsystems, labelled here as being 'left' or 'right', with isomorphic Hilbert spaces, $\mathcal{H}_{\mathrm{L}}$ and $\mathcal{H}_{\mathrm{R}}$. Energy eigenstates for each system are represented by $|E_i\rangle$, while $Z = \mathrm{tr}\, e^{-\beta H}$ is the partition function. Note that this is a purification of the thermal density matrix: tracing out over either of the component Hilbert spaces produces the thermal state.

The thermofield double state exhibits a specific entanglement structure. Given regions $A \subset L$ and $B \subset R$, these may be found to be highly entangled, according to mutual information measures, even if they are small subsystems of $L$ and $R$, with non-zero correlations $\langle O_1 O_2 \rangle$ between operators in the two subsystems $L$ and $R$. However, time evolution of the state (under $H_{\mathrm{L}} + H_{\mathrm{R}}$) results in a dissipation of this entanglement: the entanglement spreads out to larger regions linearly in time (as studied holographically by Hartman and Maldacena [34]), while the two-sided correlators decay. This dissipation of the entanglement structure also occurs if one evolves backwards in time. Hence the state at time $-t_w$ in the distant past does not have the correlations or the short-scale entanglement of the TFD state at $t = 0$. However, it can be thought of as being carefully set up so as to evolve into the TFD

state with all of its atypical entanglement structure. One therefore expects that a small perturbation applied at time $-t_w$ would destroy the entanglement structure present at $t = 0$. The question, answered by Shenker and Stanford [72], is: how is this effect manifested in the holographic dual?

The holographic dual to the thermofield double state is an eternal black hole, where the two copies, $\mathcal{H}_{\rm L}$ and $\mathcal{H}_{\rm R}$, of the Hilbert space are associated with the two asymptotic boundaries of the black hole spacetime [51]. Adding a perturbation to the left hand CFT corresponds with adding a few quanta to the left hand boundary of the spacetime. Naively, this might be expected to make little difference to the bulk geometry. However, relative to the $t = 0$ frame, these quanta have exponentially blue-shifted energy and hence their back-reaction on the metric must be considered. The result, as will be reviewed in section 2.2 of this chapter, is a shock wave in the geometry near the horizon of the black hole. Shenker and Stanford [72] consider this effect specifically for $1 + 1$ dimensional conformal field theories, for which the dual of the TFD state is given by the BTZ black hole solution, and show how this results in a lengthening of geodesics that pass through the wormhole between the two boundaries. This in turn results in the loss of entanglement between small regions $A \subset L$ and $B \subset R$, via the Ryu-Takayanagi proposal [70], and also in the decay in the correlation functions.

These results were extended to include multiple shocks [73], localized shocks [68] and stringy corrections [74], while field theory arguments have been used to show that these results apply not only to CFT's with a holographic dual, but more generally [54, 66, 13, 33, 78].

Here we focus on extending these results to include the presence of chemical potentials for charge or angular momentum. The thermofield double state is then generalized to

$$|\psi\rangle = \frac{1}{\sqrt{Z}} \sum_i e^{-\beta(E_i+\mu Q_i)/2} \, |E_i, Q_i\rangle_{\rm L} \otimes |E_i, -Q_i\rangle_{\rm R} \,, \tag{2.1.2}$$

with the holographic dual being a charged or a rotating black hole. The holographic correspondence for eternal charged black holes was studied by Brecher et al. [16] and Andrade et al. [5]. The entanglement structure of these states is similar to that of the TFD, but as $T = 1/\beta$ decreases, the entanglement becomes more non-local. In the extremal limit, $T \to 0$, the wormhole in the holographic dual becomes infinitely long. As before, this means correlators between the two copies of the CFT typically[1] decay to nothing, as does the entanglement between all but the largest regions $A \subset L$ and $B \subset R$. $L$ and $R$, however, remain entangled, while there are classes of operators

[1]There may be 'extremally-charged' operators whose two-point functions remain finite in the $T \to 0$ limit.

with two-sided correlation functions that remain finite.

It is therefore interesting to ask how small perturbations to (2.1.2) behave, given that, near extremality, the associated wormhole has already been lengthened with respect to the non-rotating, uncharged case. How is the sensitive dependence on initial conditions in the basic case modified by the introduction of charge or rotation. This chapter explores this question holographically, in the simple context of $1+1$ dimensional CFTs, dual to $2+1$ dimensional black hole solutions.[2]

Section 2.2 reviews the calculations for the uncharged non-rotating case — here the length of geodesics connecting the two boundaries in the perturbed solution at $t=0$ is given by

$$\frac{d}{l} = 2\log\frac{r}{r_+} + 2\log\left(1+\frac{\alpha}{2}\right), \tag{2.1.3}$$

where $l$ is the AdS scale, $r$ is a large-distance cutoff, $r_+$ is the radius of the black hole horizon[3] and

$$\alpha \sim \frac{E}{M} e^{2\pi t_w/\beta} = \frac{E}{M} e^{\kappa t_w} \tag{2.1.4}$$

is a parameter controlling the strength of the shock and hence the lengthening of the geodesics. Here, $E$ is the asymptotic energy of the perturbation, $M$ is the mass of the black hole, while $\kappa = 2\pi/\beta$ is the surface gravity. In section 2.3, we generalize to the rotating case, finding that the growth of the geodesics is still controlled by the temperature:

$$\alpha = \frac{\Delta r_+}{2\kappa l^2} e^{\kappa t_w} = \frac{r_+^2}{(r_+^2 - r_-^2)^2}\left(\frac{E}{4M}(r_+^2 + r_-^2) - \frac{L}{2J} r_-^2\right) \exp\left(\frac{r_+^2 - r_-^2}{l^2 r_+} t_w\right). \tag{2.1.5}$$

Here $L$ is the angular momentum of the perturbation while $J$ is that for the original black hole. $\Delta r_+$ is the change in the outer momentum radius. This is consistent with the results of Leichenauer [47]. The Lyapunov exponent characteristic of quantum chaos is thus still $\lambda_L = \kappa$, as in the simple thermal system, while the prefactor is also controlled by the surface gravity (or the temperature). Hence the dynamics are only sensitive to the additional scale associated with the angular momentum via the surface gravity. In the extremal limit, at fixed mass, the temperature goes to zero and the decorrelation slows down. The same slowing of time evolution controlled entirely by the temperature is seen in correlation functions on unperturbed charged black holes [16, 5]. In contrast, in the limit of vanishing rotation, the results reduce

[2] After completing this work, we realised that this extension had been previously considered by Leichenauer [47]. (More recent related work in this area has also been performed by Sircar et al. [75] and by Roberts and Swingle [67].) While there is some overlap with our work, that paper focuses on the mutual information and higher dimensional black holes, while here we focus on correlation functions in $2+1$ dimensional spacetimes.

[3] We use $r_+$ for the horizon radius rather than the $R$ of Shenker and Stanford [72] to be consistent with the rotating and charged cases to be considered later.

to the previous analysis of Shenker and Stanford [72], as expected.

In section 2.4, we consider the charged case. In this case, it is not possible to proceed as far analytically, though numerical results are consistent with those found for the other cases. The Lyapunov exponent is again controlled solely by the temperature, with the decorrelation slowing down in the extremal limit. As expected, as the charge vanishes we smoothly recover the previous analysis. In section 2.5, we comment on the extension to higher dimensions, where we argue that holographic analysis of correlation functions requires the consideration of geodesics in the complexified spacetime. Further exploration of this is a matter for future research.

## 2.2 A review of the uncharged, non-rotating case

We first review the work of Shenker and Stanford [72] which, for simplicity, considers the effect of a spherically symmetric perturbation on the uncharged, non-rotating BTZ black hole in $2+1$ dimensions. The unperturbed metric is simply

$$ds^2 = -f(r)\,dt^2 + \frac{dr^2}{f(r)} + r^2\,d\phi^2, \tag{2.2.1}$$

where[4]

$$f(r) = \frac{r^2 - r_+^2}{l^2} = \frac{r^2}{l^2} - M. \tag{2.2.2}$$

Here the horizon radius is $r_+$, while $l$ is the AdS scale and $M$ is the black hole mass.

To more easily analyse the effect of adding a perturbation, it is necessary to use Kruskal coordinates. For $r > r_+$ we define

$$\begin{aligned} U &= -e^{-\kappa u}, \\ V &= e^{\kappa v}, \end{aligned} \tag{2.2.3}$$

where $\kappa = r_+/l^2$ is the surface gravity[5], and $u, v = t \mp r_*$, with the tortoise coordinate

$$r_* = -\int_r^\infty \frac{dr'}{f(r')} = \frac{l^2}{2r_+} \log\left(\frac{r - r_+}{r + r_+}\right). \tag{2.2.4}$$

This gives

$$UV = -\frac{r - r_+}{r + r_+} \tag{2.2.5}$$

[4]Shenker and Stanford [72] have an extra factor of $8G_N$ here, which we absorb into the mass $M$.

[5]This factor of $\kappa$ in the definitions of $U$ and $V$ is necessary to eliminate the coordinate singularity at $r = r_+$.

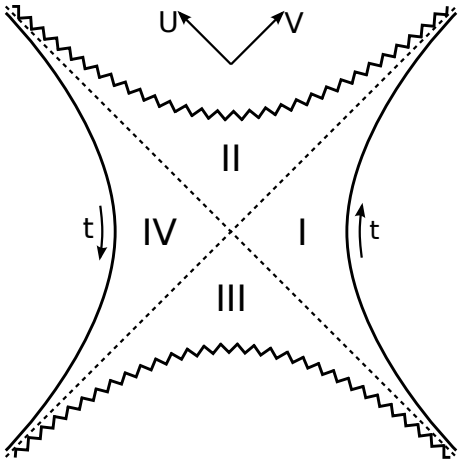


Figure 2.1: Regions I to IV in Kruskal coordinates.

and

$$ds^2 = \frac{-4l^2\, dU\, dV + r_+^2(1-UV)^2\, d\phi^2}{(1+UV)^2}, \tag{2.2.6}$$

defining the relation between the ordinary BTZ coordinates and the Kruskal coordinates in region I of figure 2.1. For $r < r_+$ we can perform a similar coordinate transformation, arranging for $U$ to be positive and $V$ to be negative, resulting in the same metric as in (2.2.6), but for region II of figure 2.1. Region III corresponds to a second copy of $r < r_+$, while region IV is a second copy of $r > r_+$. In the new coordinate system, the two boundaries of the spacetime correspond to $UV = -1$, while the two singularities occur at $UV = 1$. Between these extremes, the metric is manifestly non-singular.

We add energy to the system on the left boundary at some early time, i.e. at a large value, $t_w$, of the $t$ coordinate. For simplicity, it is assumed that the perturbation is spherically symmetric, while the asymptotic energy of the perturbation, $E$, is assumed to be small compared with the black hole mass $M$. Formally, we take the limit $E/M \to 0$, $t_w \to \infty$ with $Ee^{\kappa t_w}/M$ fixed.

In this limit, the perturbation approximately follows null geodesics along the surface $U_w = e^{-\kappa t_w}$. The perturbed geometry is then obtained by gluing a BTZ solution, with mass $M$ to the right/past of the perturbation, to another with mass $M+E$ to the left/future. To the right of the shock, we have coordinates $U$, $V$ and $\phi$, with parameter $M$ or $r_+$. To the left, we have $\tilde{U}$, $\tilde{V}$, $\phi$ and parameter $\tilde{M} = M + E$ or $\tilde{r}_+ = \sqrt{\frac{M+E}{M}} r_+$. The relationship between the two coordinate systems on the shock is fixed by imposing two conditions:

1. The time coordinate $t$ is required to be continuous at the boundary, i.e. at $r = \infty$. This fixes a relative boost ambiguity.

2. The size of the $S^1$ must be continuous across the shock.

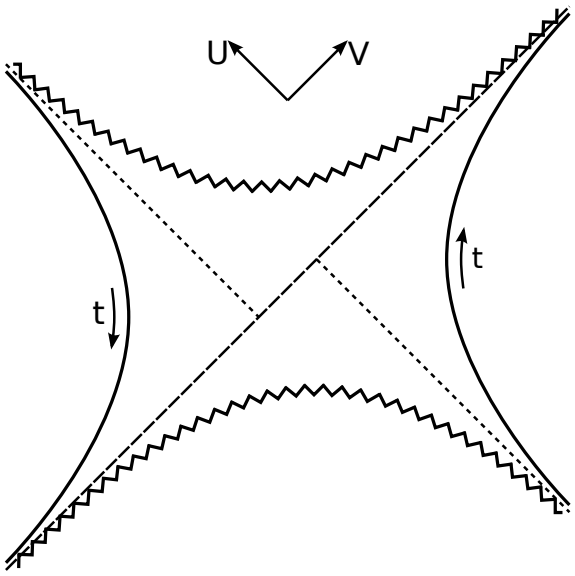


Figure 2.2: Kruskal coordinates and the perturbed BTZ solution.

The first of these conditions means that, to the left of the shock, $\tilde{U}_w = e^{-\tilde{\kappa} t_w}$, where $\tilde{\kappa} = \tilde{r}_+/l^2$. In the limit we get $\tilde{U}_w = U_w(1 - t_w \Delta\kappa)$, where $t_w \Delta\kappa$ is small. Using this result in combination with the second condition then gives

$$\tilde{V} = V + \alpha, \tag{2.2.7}$$

where

$$\alpha = \frac{\Delta r_+}{2\kappa l^2} e^{\kappa t_w} = \frac{E}{4M} e^{r_+ t_w / l^2}. \tag{2.2.8}$$

This is illustrated in figure 2.2.

Note that the positivity of $\alpha$, the step change in the $V$ coordinate, is simply related to the second law of thermodynamics for black holes. We can make $\alpha$ as large as desired by pushing the perturbation further back in time, i.e. by increasing $t_w$.

The essential features of the above calculation — the derivation of Kruskal coordinates in terms of the tortoise coordinate and the matching conditions across the shock — will be the same in the other cases that we will consider, as will the general form of the perturbation $\alpha$.

As BTZ is locally $AdS_3$, geodesic length is conveniently calculated by using the embedding coordinates in a flat $2+2$ dimensional spacetime, in which the length of geodesics between points $p$ and $p'$ is given by

$$\cosh \frac{d}{l} = \frac{1}{l^2} \left( T_1 T_1' + T_2 T_2' - X_1 X_1' - X_2 X_2' \right). \tag{2.2.9}$$

These coordinates are related to the Kruskal and BTZ coordinates by

$$\begin{aligned} T_1 &= l\frac{V+U}{1+UV} = \frac{l}{r_+}\sqrt{r^2-r_+^2}\sinh\frac{r_+t}{l^2}, \\ T_2 &= l\frac{1-UV}{1+UV}\cosh\frac{r_+\phi}{l} = \frac{lr}{r_+}\cosh\frac{r_+\phi}{l}, \\ X_1 &= l\frac{V-U}{1+UV} = \frac{l}{r_+}\sqrt{r^2-r_+^2}\cosh\frac{r_+t}{l^2}, \\ X_2 &= l\frac{1-UV}{1+UV}\sinh\frac{r_+\phi}{l} = \frac{lr}{r_+}\sinh\frac{r_+\phi}{l}, \end{aligned} \tag{2.2.10}$$

in region I. (Since rotating BTZ is also locally $AdS_3$, we will be able to use the same method for this case later. The case of charged BTZ will require an alternative approach.)

Geodesics between points on opposite boundaries of the perturbed spacetime must necessarily cross the shock. To calculate distances between such points, it is necessary to

1. Calculate the geodesic distance between a general location, $U = 0$, $V = V_{\text{shock}}$, on the shock and each of the two boundary points.

2. Extremize the sum over $V_{\text{shock}}$.

This is illustrated in figure 2.3. We use the coordinates to the right of the shock to

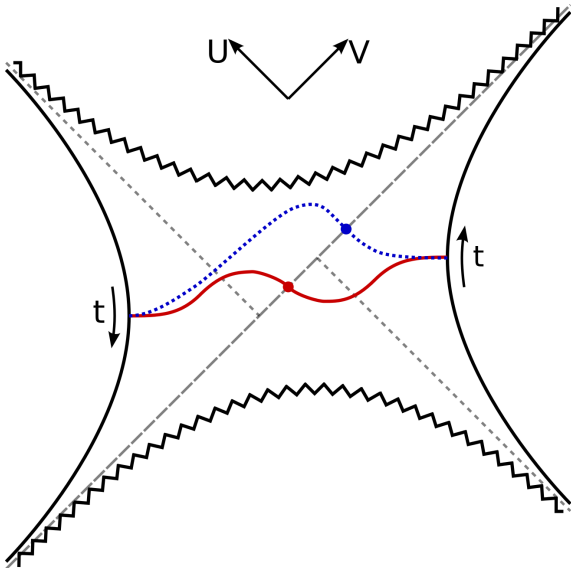


Figure 2.3: Geodesics through the perturbed wormhole are found by gluing geodesics from each side at a general location on the shock and extremizing the total length over this location. The blue, dashed line shows two geodesics glued at an arbitrary location. The red, solid line, passing through the centre of the conformal diagram, extremizes the total length and is therefore the geodesic required.

label the point on the shock. If the two boundary points are both at $t = 0$ and at equal angular coordinate $\phi$, we find that the geodesic crosses the shock at the centre of the conformal diagram at $V_{\text{shock}} = -\alpha/2$, as one would expect from symmetry. Regulating the overall divergence in the length of the geodesic by taking the distance between points at some large fixed radius $r$, we obtain

$$\frac{d}{l} = 2\log\frac{2r}{r_+} + 2\log\left(1+\frac{\alpha}{2}\right). \tag{2.2.11}$$

The second term gives the increase in the length of the geodesic resulting from the addition of the perturbation. This increase may be made arbitrarily large by increasing $t_w$, i.e. by moving the perturbation further back into the past.

As mentioned previously, we can use geodesic length to obtain an approximation to the two-point correlation function of operators inserted on the two boundaries of the black hole. In this case, we obtain

$$\langle W|V_L V_R|W\rangle \sim e^{-\Delta d/l} \sim r^{-2\Delta}\left(1+\frac{\alpha}{2}\right)^{-2\Delta}, \tag{2.2.12}$$

where $|W\rangle$ is the state obtained by acting on the TFD with the perturbation $W(t_w)$ on the left hand Hilbert space, $\mathcal{H}_{\text{L}}$, while $\Delta$ is the scaling dimension of the inserted operators.

## 2.3 The butterfly effect for rotating BTZ

### 2.3.1 Kruskal coordinates for rotating BTZ

The simplest extension of this calculation is to consider the rotating BTZ solution, as the geometry is still locally $\text{AdS}_3$, so geodesic calculations remain simple and a good deal of progress can be made analytically. This generalization introduces an additional length scale associated with the rotation, so it is interesting to examine to what extent the physical effects depend on this scale.

The rotating BTZ metric is [9]

$$ds^2 = -f^2(r)\,dt^2 + f^{-2}(r)\,dr^2 + r^2\left[N^\phi(r)\,dt + d\phi\right]^2 \tag{2.3.1}$$

where

$$f^2(r) = -M + \left(\frac{r}{l}\right)^2 + \frac{J^2}{4r^2}, \tag{2.3.2}$$

and we adopt co-rotating coordinates, since we are interested in the behaviour near the (outer) horizon, so

$$N^\phi(r) = \frac{J}{2}\frac{r^2 - r_+^2}{r^2 r_+^2}. \tag{2.3.3}$$

The horizon radii $r_+$ and $r_-$ are the solutions to $f^2(r) = 0$,

$$r_\pm^2 = \frac{1}{2}\left(Ml^2 \pm \sqrt{(Ml^2)^2 - J^2l^2}\right). \tag{2.3.4}$$

We will find it useful to express the metric entirely in terms of $r_+$ and $r_-$, rather than $M$ and $J$, which are

$$\begin{aligned} M &= \frac{r_+^2 + r_-^2}{l^2}, \\ J &= \frac{2r_+r_-}{l}. \end{aligned} \tag{2.3.5}$$

We will assume without loss of generality that $J$ is positive. The metric functions in terms of $r_\pm$ are

$$N^\phi(r) = \frac{r_-}{r_+}\frac{r^2 - r_+^2}{lr^2} \tag{2.3.6}$$

and

$$f^2(r) = \frac{(r^2 - r_+^2)(r^2 - r_-^2)}{l^2r^2}. \tag{2.3.7}$$

We introduce Kruskal coordinates by writing as before

$$U = -e^{-\kappa u}, \tag{2.3.8}$$

$$V = e^{\kappa v}, \tag{2.3.9}$$

where $u, v = t \mp r_*$ and the tortoise coordinate is

$$r^* = \frac{1}{2\kappa}\log\frac{\sqrt{r^2 - r_-^2} - \sqrt{r_+^2 - r_-^2}}{\sqrt{r^2 - r_-^2} + \sqrt{r_+^2 - r_-^2}} \tag{2.3.10}$$

where $\kappa$ is given by

$$\kappa = \frac{r_+^2 - r_-^2}{l^2r_+}. \tag{2.3.11}$$

This gives the metric

$$ds^2 = \frac{-4l^2\,dU\,dV - 4lr_-(U\,dV - V\,dU)\,d\phi + \left[(1-UV)^2r_+^2 + 4UVr_-^2\right]\,d\phi^2}{(1+UV)^2}. \tag{2.3.12}$$

Note that this derivation of Kruskal coordinates assumes $r > r_+$ and is the equivalent of the calculation for region I in the non-rotating case. As in the basic case, we can extend the coordinate system to cover regions II–IV. In this case, $r > r_+$ gives two regions, I and IV (as in the basic case) while regions II and III have $r_- < r < r_+$. The metric (2.3.12) covers all four regions. These four regions do not cover $r < r_-$, but are sufficient for our purposes. [6]

[6]Note also that the Kruskal coordinates defined here are not those described by Bañados et al. [9].

### 2.3.2 Adding the perturbation

We consider a spherically symmetric shell which meets the boundary at some time $t_w$. For finite $t_w$, the trajectory of this shell in the $U$, $V$ plane depends on the angular momentum it carries, but if we take the limit of large $t_w$, we apply a large boost in the $U$, $V$ plane and the trajectory becomes approximately lightlike, along a line of constant $U$ as in the non-rotating case. (For any small part of the shell, this line is also approximately constant in $\phi$, regardless of the angular momentum of the perturbation.) The matching problem is then very similar to that in the non-rotating case. We glue two copies of the rotating BTZ spacetime together along a shock at $U = e^{-\kappa t_w}$. To the right of the shock, the black hole has mass $M$, angular momentum $J$ and coordinates $U$, $V$ and $\phi$, while to the left of the shock, we have mass $\tilde{M} = M + E$, angular momentum $\tilde{J} = J + L$ and coordinates $\tilde{U}$, $\tilde{V}$ and $\phi$. We impose continuity of $t$ at the boundary and $r$ across the shock. The result is a jump in $V$,

$$\tilde{V} = V + \alpha, \tag{2.3.13}$$

where

$$\alpha = \frac{\Delta r_+}{2\kappa l^2} e^{\kappa t_w} \tag{2.3.14}$$

exactly as in the non-rotating case. In terms of $M$, $J$, $E$ and $L$

$$\alpha = \frac{r_+^2}{(r_+^2 - r_-^2)^2} \left( \frac{E}{4M}(r_+^2 + r_-^2) - \frac{L}{2J} r_-^2 \right) \exp\left( \frac{r_+^2 - r_-^2}{l^2 r_+} t_w \right). \tag{2.3.15}$$

Since the rotating black holes have a throat which grows infinitely long in the extremal limit, one might think that, for near-extremal black holes, it would be possible to add a shock that takes one away from extremality, lowering the length of the wormhole. However, we find that so long as the second law of thermodynamics is obeyed, so that $\Delta r_+ > 0$, the jump $\alpha$ is positive, as indicated by (2.3.14). We will now see that this leads to a longer wormhole.

### 2.3.3 Geodesic lengths

As in the non-rotating case, we calculate the length of the geodesics in embedding coordinates. For our co-rotating coordinates, the relation to the embedding coordinates (adjusted from Bañados et al. [9, section III.B.3] to take into account the co-rotation) is

$$\begin{aligned} T_1 &= \pm\sqrt{\pm B(r)}\sinh\tilde{t}(t,\phi), \\ T_2 &= \sqrt{A(r)}\cosh\tilde{\phi}(t,\phi), \\ X_1 &= \pm\sqrt{\pm B(r)}\cosh\tilde{t}(t,\phi), \\ X_2 &= \sqrt{A(r)}\sinh\tilde{\phi}(t,\phi), \end{aligned} \tag{2.3.16}$$

where

$$\begin{aligned} A(r) &= l^2 \frac{r^2 - r_-^2}{r_+^2 - r_-^2}, \\ B(r) &= l^2 \frac{r^2 - r_+^2}{r_+^2 - r_-^2} \end{aligned} \tag{2.3.17}$$

and

$$\begin{aligned} \tilde{\phi} &= \frac{r_+ \phi}{l} \\ \tilde{t} &= \kappa t - \frac{r_-}{l}\phi. \end{aligned} \tag{2.3.18}$$

Here the first $\pm$ in the formulae is positive for regions I and II and negative for regions III and IV, while the second is positive for regions I and IV and negative for regions II and III. The transformation from the Kruskal coordinates to the embedding coordinates is then easily shown to be

$$\begin{aligned} T_1 &= l\frac{V+U}{1+UV}\cosh\frac{r_-\phi}{l} - l\frac{V-U}{1+UV}\sinh\frac{r_-\phi}{l}, \\ T_2 &= l\frac{1-UV}{1+UV}\cosh\frac{r_+\phi}{l}, \\ X_1 &= l\frac{V-U}{1+UV}\cosh\frac{r_-\phi}{l} - l\frac{V+U}{1+UV}\sinh\frac{r_-\phi}{l}, \\ X_2 &= l\frac{1-UV}{1+UV}\sinh\frac{r_+\phi}{l}, \end{aligned} \tag{2.3.19}$$

with these relationships holding in all four regions.

We first consider a geodesic from a point at $t = 0$, $\phi = 0$ on one boundary to the point $t = 0$, $\phi = 0$ on the other. As before, we must join geodesics from the two boundary points at a general point on the shock and then extremize the geodesic length. The complication relative to the discussion of Shenker and Stanford [72] is that the geodesic may not meet the shock at $\phi = 0$. We must therefore extremize the geodesic length with respect to both the $V$ and the $\phi$ coordinates of the meeting point.

To the left of the shock, we need the distance from $(t, r, \phi) = (0, r, 0)$ (in region IV) to $(U', V', \phi') = (0, V + \alpha, \phi)$. The embedding coordinates of the first point are

$$\begin{aligned} T_1 &= 0, \\ T_2 &= l\sqrt{\frac{r^2 - r_-^2}{r_+^2 - r_-^2}}, \\ X_1 &= -l\sqrt{\frac{r^2 - r_+^2}{r_+^2 - r_-^2}}, \\ X_2 &= 0. \end{aligned} \tag{2.3.20}$$

while for the second point we get

$$\begin{aligned} T_1' &= l(V+\alpha)\cosh\frac{r_-\phi}{l} - l(V+\alpha)\sinh\frac{r_-\phi}{l} = l(V+\alpha)e^{-r_-\phi/l}, \\ T_2' &= l\cosh\frac{r_+\phi}{l}, \\ X_1' &= l(V+\alpha)\cosh\frac{r_-\phi}{l} - l(V+\alpha)\sinh\frac{r_-\phi}{l} = l(V+\alpha)e^{-r_-\phi/l}, \\ X_2' &= l\sinh\frac{r_+\phi}{l} \end{aligned} \tag{2.3.21}$$

If we let $d_1$ be the length of the geodesic to the left of the shock, then

$$\begin{aligned} \cosh\frac{d_1}{l} &= \frac{1}{l^2}(T_2T_2' - X_1X_1') \\ &= \sqrt{\frac{r^2-r_-^2}{r_+^2-r_-^2}}\cosh\frac{r_+\phi}{l} + (V+\alpha)\sqrt{\frac{r^2-r_+^2}{r_+^2-r_-^2}}e^{-r_-\phi/l} \\ &\simeq \frac{r}{\sqrt{r_+^2-r_-^2}}\left(\cosh\frac{r_+\phi}{l} + (V+\alpha)e^{-r_-\phi/l}\right). \end{aligned} \tag{2.3.22}$$

For the geodesic to the right of the shock, the calculation proceeds as above, but with the sign of $X_1$ reversed for the boundary point and $V+\alpha$ replaced by $V$ at the shock. Hence

$$\cosh\frac{d_2}{l} \simeq \frac{r}{\sqrt{r_+^2-r_-^2}}\left(\cosh\frac{r_+\phi}{l} - Ve^{-r_-\phi/l}\right). \tag{2.3.23}$$

To find the value of $V$ that extremizes $d = d_1 + d_2$, we differentiate to get

$$\frac{1}{l}\sinh\left(\frac{d_1}{l}\right)\frac{\partial d_1}{\partial V} = \frac{r}{\sqrt{r_+^2-r_-^2}}e^{-r_-\phi/l}, \tag{2.3.24}$$

$$\frac{1}{l}\sinh\left(\frac{d_2}{l}\right)\frac{\partial d_2}{\partial V} = -\frac{r}{\sqrt{r_+^2-r_-^2}}e^{-r_-\phi/l} \tag{2.3.25}$$

so that

$$\frac{\partial d}{\partial V} = \frac{lr}{\sqrt{r_+^2-r_-^2}}e^{-r_-\phi/l}\left(\frac{1}{\sinh(d_1/l)} - \frac{1}{\sinh(d_2/l)}\right). \tag{2.3.26}$$

This vanishes if $d_1 = d_2$, which gives $V = -\alpha/2$, as we might again have expected from symmetry. Equation (2.3.23) now gives us

$$\frac{d}{2l} = \log\frac{2r}{\sqrt{r_+^2-r_-^2}} + \log\left(\cosh\frac{r_+\phi}{l} + \frac{\alpha}{2}e^{-r_-\phi/l}\right), \tag{2.3.27}$$

where we have used $\cosh^{-1}x \simeq \pm\log(2x)$ for large $x$. Note that since $\alpha > 0$, the perturbation must increase the length of the geodesic.

Extremizing (2.3.27) with respect to $\phi$ gives us

$$r_+\sinh\frac{r_+\phi}{l} = \frac{\alpha r_-}{2}e^{-r_-\phi/l}. \tag{2.3.28}$$

We define $\phi^*$ to be the value of $\phi$ satisfying this equation and we let $p(\alpha)$ be the contribution of the perturbation to the geodesic length $d/l$, i.e.

$$p(\alpha) = 2\log\left(\cosh\frac{r_+\phi^*}{l} + \frac{\alpha}{2}e^{-r_-\phi^*/l}\right), \tag{2.3.29}$$

so that

$$\frac{d}{l} = 2\log\frac{2r}{\sqrt{r_+^2 - r_-^2}} + p(\alpha). \tag{2.3.30}$$

Unfortunately, it appears that we cannot solve (2.3.28) analytically, except in the special cases of non-rotating and extremal black holes. In the first case, we saw earlier that $\phi^* = 0$ and

$$p(\alpha) = 2\log\left(1 + \frac{\alpha}{2}\right), \tag{2.3.31}$$

while for extremal black holes when $r_+ = r_-$ we get

$$\phi^* = \frac{l}{2r_+}\log(1+\alpha) \tag{2.3.32}$$

and

$$p(\alpha) = \log(1+\alpha). \tag{2.3.33}$$

In the general case, it is straightforward to show that both $\phi^*$ and $p(\alpha)$ (and hence the geodesic length) increase with $\alpha$. Given the expressions for $p(\alpha)$ for the two special cases, one would expect similar logarithmic increases in $p(\alpha)$ with respect to $\alpha$ in the general case. The results of numerical calculations, displayed in figure 2.4, would appear to confirm this.

Given the non-trivial behaviour of the angular coordinate for these geodesics, there is the concern that it might be possible to find a shorter geodesic between the boundary points, by allowing $\phi$ to go from zero on one boundary to $\phi = 2\pi$ on the other. Applying the numerical calculations to general values of $\phi$ on the boundaries is straightforward, resulting in figure 2.5. The monotonic increase in geodesic length with the difference in angular coordinate confirms that the shortest geodesic between matching boundary points is that calculated between matching values of $\phi$, not values differing by some multiple of $2\pi$.

As in the non-rotating case, this increase in the length of the geodesics can be interpreted as a decrease in the correlation functions of operators in the state $|W\rangle$ created by acting with the perturbation $W(t_w)$. In the rotating black hole, the initial value of the correlators before the perturbation is smaller, as the presence of the denominator $\sqrt{r_+^2 - r_-^2}$ in (2.3.30), rather than simply $r_+$ as in (2.2.11), increases the length of the geodesics. However, the dynamical evolution is as in the non-rotating case, and the change in the length of the geodesics becomes appreciable when $\alpha$ is of order one, at the scrambling time $t_s = \kappa^{-1}\ln(\kappa/\Delta r_+)$. As in the non-rotating

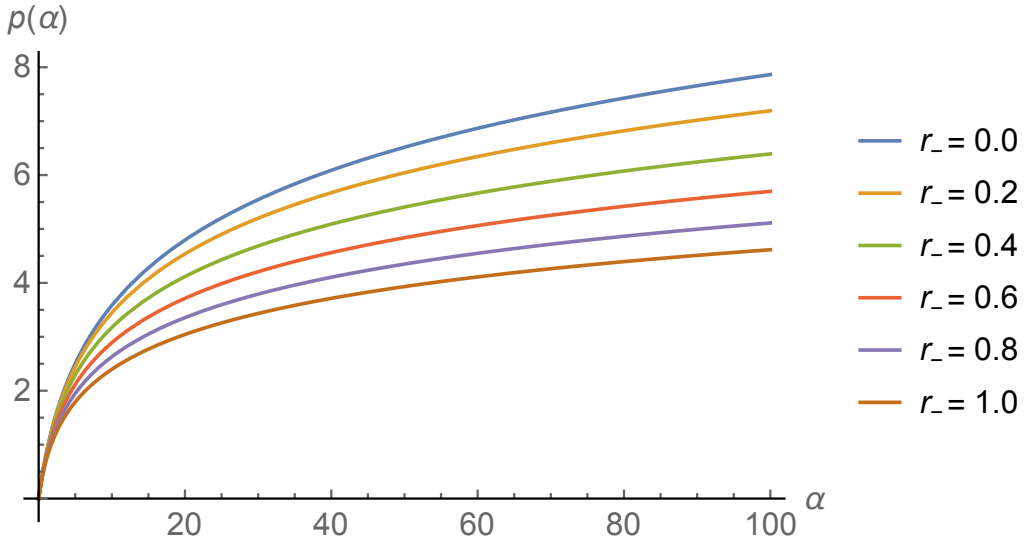


Figure 2.4: Increase in the length of the geodesic, as a function of the size of the jump in $V$ coordinate at the shock. Here $r_+ = 1$, so the plot shows graphs for the non-rotating and extremal black holes and four intermediate cases.

case, this scales logarithmically with the ratio of the energy of the black hole to the energy of the perturbation. If we approach the extremal limit, $\Delta r_+$ could be small compared with $r_+$ but large compared to $\kappa$, but for this to change the scaling form of $t_s$, we would need to go to temperatures $T$ of order of the energy of the perturbation.

We can also consider the implications of the geodesic calculation for the entanglement entropy (as in Leichenauer [47]), which is also similar to the non-rotating case. Consider the mutual information of two matching regions, one on each boundary, with arc length $\phi$ and centred on the same angular coordinate. Firstly, the entanglement entropy of one of the regions is, assuming $\phi < \pi$,

$$S_A = \frac{l}{4G_N}\left(2\log\frac{2r}{\sqrt{r_+^2 - r_-^2}} + \log\sinh\frac{(r_+ + r_-)\phi}{2l} + \log\sinh\frac{(r_+ - r_-)\phi}{2l}\right). \tag{2.3.34}$$

Meanwhile, the entanglement entropy of $A \cup B$ is the smallest of

$$S^{(1)}_{A\cup B} = S_A + S_B, \tag{2.3.35}$$

$$S^{(2)}_{A\cup B} = \frac{l}{2G_N}\left(2\log\frac{2r}{\sqrt{r_+^2 - r_-^2}} + p(\alpha)\right). \tag{2.3.36}$$

Now

$$S^{(1)}_{A\cup B} - S^{(2)}_{A\cup B} = \frac{l}{2G_N}\left(\log\sinh\frac{(r_+ + r_-)\phi}{2l} + \log\sinh\frac{(r_+ - r_-)\phi}{2l} - p(\alpha)\right) \tag{2.3.37}$$

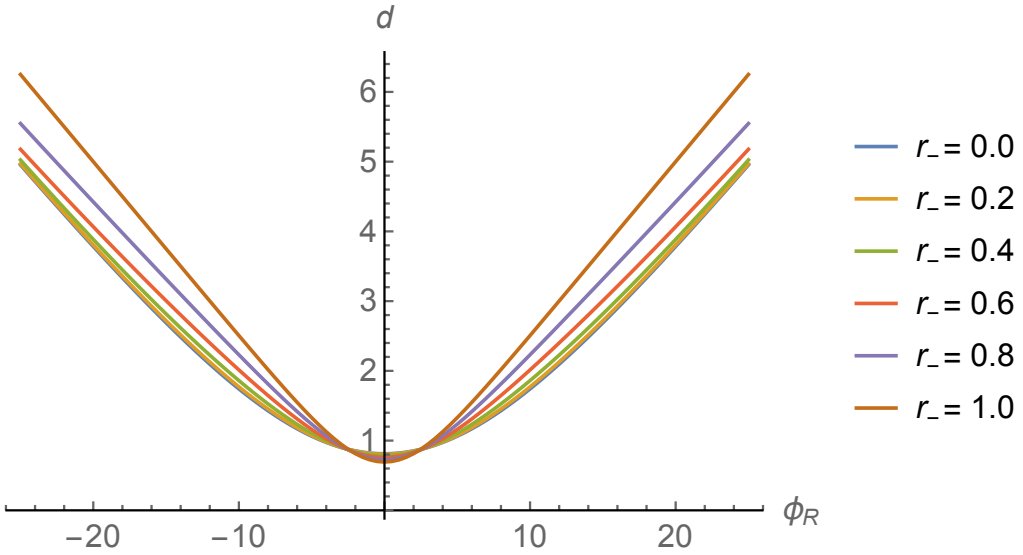


Figure 2.5: Overall geodesic distance plotted against the value of $\phi$ on the right hand boundary, for a range of different $r_-$. Again, $r_+ = 1$, while $\phi$ is set to zero on the left hand boundary.

and if this is positive, then it gives the mutual information, $I(A;B)$. Otherwise, the mutual information is zero and there is no entanglement between the two regions. Near extremality, we need to have large regions to have non-zero mutual information. But our interest here is in the effect of the perturbation, and again the effect becomes significant, decreasing the local entanglement, just when $\alpha$ becomes of order one. Local entanglement is therefore reduced by the perturbation at a rate controlled by the scrambling time.

## 2.4 The butterfly effect for charged BTZ

The calculation for rotating BTZ is interesting, but as the solution is still locally $AdS_3$, this is a rather special case. We would like to extend the above calculation to further examples. As we will discuss in the next section, considering the correlators for black holes in higher dimensions (charged or uncharged) is challenging. Therefore, we consider here the calculation for a charged black hole in $2+1$ dimensions. We consider Einstein-Hilbert gravity coupled to an ordinary Maxwell field. (It is perhaps more common to consider a Chern-Simons gauge field in this context, but then the solution would remain locally AdS.)

The metric is

$$ds^2 = -f(r)\,dt^2 + \frac{dr^2}{f(r)} + r^2\,d\phi^2 \tag{2.4.1}$$

where

$$f(r) = \frac{r^2}{l^2} - M - \frac{Q^2}{2}\log\frac{r}{l}. \tag{2.4.2}$$

This is supported by a gauge field

$$A = Q \log \frac{r}{r_+}\, dt. \tag{2.4.3}$$

We can introduce Kruskal coordinates where

$$U = -e^{-\kappa u}, \tag{2.4.4}$$

$$V = e^{\kappa v}, \tag{2.4.5}$$

where $u, v = t \mp r_*$ with a tortoise coordinate

$$r_* = -\int_r^\infty \frac{dr}{f(r)}, \tag{2.4.6}$$

and $\kappa = f'(r_+)/2$ is the surface gravity. The metric in these coordinates is

$$ds^2 = \frac{f(r)}{\kappa^2 UV}\, dU\, dV + r^2\, d\phi^2, \tag{2.4.7}$$

where $r$ is a function of $U$ and $V$. In this case one cannot evaluate the integral in (2.4.6) for the tortoise coordinate, so we cannot give a simple expression for $r$ in terms of $U$ and $V$. Near the horizon $r = r_+$,

$$\lim_{r \to r_+} r_* = \frac{1}{2\kappa} \ln\left(\frac{r - r_+}{r_+}\right) + \frac{1}{2\kappa} \ln C \tag{2.4.8}$$

for some finite constant $C$. This gives $UV \approx -C(r - r_+)/r_+$, so the metric (2.4.7) is regular there. The constant $C$ can be determined numerically for generic parameter values; in the extremal limit $r_+ \to r_-$, it diverges as $C \sim 1/(r_+ - r_-) \sim 1/\kappa$, as in the rotating case.

We consider perturbing this solution by throwing in a charged spherically symmetric shell from the left boundary at some early time $t_w$. The shell will then approximately follow the null trajectory $U = e^{-\kappa t_w}$. The step change in the $V$ coordinate in the shock is determined by the same matching conditions, which give, as before

$$\tilde{V} = V + \alpha, \tag{2.4.9}$$

where

$$\alpha = C \frac{\Delta r_+}{r_+} e^{\kappa t_w}. \tag{2.4.10}$$

Here the relation between $\Delta r_+$ and the parameters of the shell would need to be determined numerically for finite $\Delta r_+$ — for small perturbations adding $m$ to the black hole mass $M$ and $q$ to the charge $Q$ we have

$$\Delta r_+ \approx \frac{1}{2\kappa} \left(m + Qq \log \frac{r_+}{l}\right). \tag{2.4.11}$$

However, we can see that positivity of the shift $\alpha$ continues to be related to the second law.

### 2.4.1 Geodesic lengths

For this case, we cannot find the lengths of geodesics by using the embedding coordinates, so we need to simply solve the geodesic equations numerically. Using the symmetry of the solution we can reduce the problem to an effective one-dimensional problem, for spacelike geodesics

$$\dot{r}^2 = f(r)\left(1 - \frac{L^2}{r^2}\right) + E^2, \tag{2.4.12}$$

where $E = f(r)\dot{t}$ and $L = r^2\dot{\phi}$ are the constants of motion.

In the unperturbed spacetime, we are interested in geodesics in a constant-time slice (at $t = 0$), so we take $E = 0$. Since $\dot{r}^2 = 0$ only at $r = r_-$, $r = r_+$ or $r = L$ and since our geodesics will start at the boundary, they can only have turning points at either $r = r_+$ or $r = L$, whichever is the larger. For $L > r_+$ we obtain geodesics that return to the boundary from which they started. These will be used in calculations of mutual information. Smaller values of $L$ pass through the wormhole. In either case, half the geodesic length is given by

$$\frac{d}{2} = \lambda_{\text{turn}} = \int_{\infty}^{r_{\text{turn}}} \frac{dr}{\dot{r}} = \int_{r_{\text{turn}}}^{\infty} \frac{dr}{\sqrt{(1 - L^2/r^2)\, f(r)}}, \tag{2.4.13}$$

where we have assumed that the affine parameter $\lambda$ starts at zero on the boundary and that $\dot{r}$ is negative up to the half way point at $\lambda = \lambda_{\text{turn}}$. This integral is clearly divergent. To find the convergent part, we calculate the integral up to some large value $R$ and subtract the divergent part, given by $l \log R$. We also need to determine the change in the angular coordinate,

$$\frac{\Delta\phi}{2} = \int_0^{\lambda_{\text{turn}}} \frac{L}{r^2}\, d\lambda. \tag{2.4.14}$$

For the perturbed spacetime, we consider the geodesics connecting two points at $t = 0, \phi = 0$ on the two boundaries. The symmetry implies the minimal geodesic connecting these points will have $L = 0$. It will run from the first boundary to some point on the shock with arbitrary $V$ coordinate and then to the second boundary; we need to consider general points on the shock and extremise over the position. These geodesics will then have $E \neq 0$. The turning points are solutions to $f(r) + E^2 = 0$. If $E^2$ is large enough then there are no solutions, and the geodesic hits the singularity. Alternatively, there will be two (possibly coincident) solutions to $\dot{r}^2 = 0$, with values

of $r$ between $r_-$ and $r_+$. The geodesic will turn (or rather, start heading out again, with $\dot{r} > 0$) at the larger of these solutions.

The simplest case is when $E > 0$. Then $\dot{t} > 0$ and so the geodesic reaches the shock at $r = r_+$ before reaching a turning point. After solving for $r$, we use

$$\dot{v} = \frac{E - \sqrt{(1 - L^2/r^2)\, f(r) + E^2}}{f(r)}, \tag{2.4.15}$$

valid for $\dot{r} < 0$, and integrate to obtain $v$ at the intersection with the shock. The geodesic for $E = 1$, up to the shock, is shown in figure 2.6.[7]

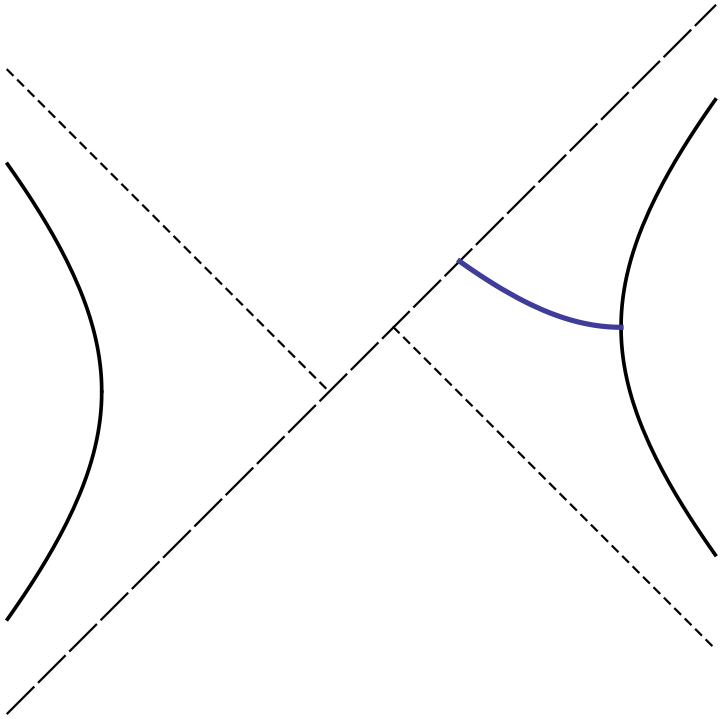

Figure 2.6: Geodesic for $L = 0$, $E = 1$, up to the shock. Note that $r$ remains greater than $r_+$ until the geodesic reaches the shock.

The more important case is when $E < 0$, as it is this case that will produce (half of) the minimal length geodesic through the wormhole. We find that the geodesic passes through the past horizon at $r = r_+$, before reaching a turning point where $\dot{r}$ becomes positive and then finally reaching the shock. The geodesic length must be calculated in two halves, before and after the turn. Up to the turn, with $\dot{r} < 0$, we solve for $r$ and $u$ in terms of $\lambda$ as before, but using

$$\dot{u} = \frac{E + \sqrt{(1 - L^2/r^2)\, f(r) + E^2}}{f(r)} \tag{2.4.16}$$

[7] Creating this plot requires only a little more calculation than that needed for the calculation of geodesic lengths — we must also determine values of the $u$ coordinate along the geodesic and then convert to $U$ and $V$.

to calculate $u$ rather than $v$, since $v$ behaves poorly upon crossing the past horizon. We then convert $u$ to $v$ at the turn by adding $2r^*$ using the region III formula for $r^*$.

To handle the second half, we integrate $dr/\dot{r}$ from $r_{\text{turn}}$ to $r_+$ to get $\lambda$ at the shock, and hence the length of the geodesic up to this point. We numerically solve the differential equation for $r$ back from the shock to the turning point and use the result to solve for $v$. Geodesics for a range of negative values of $E$ are shown in figure 2.7.

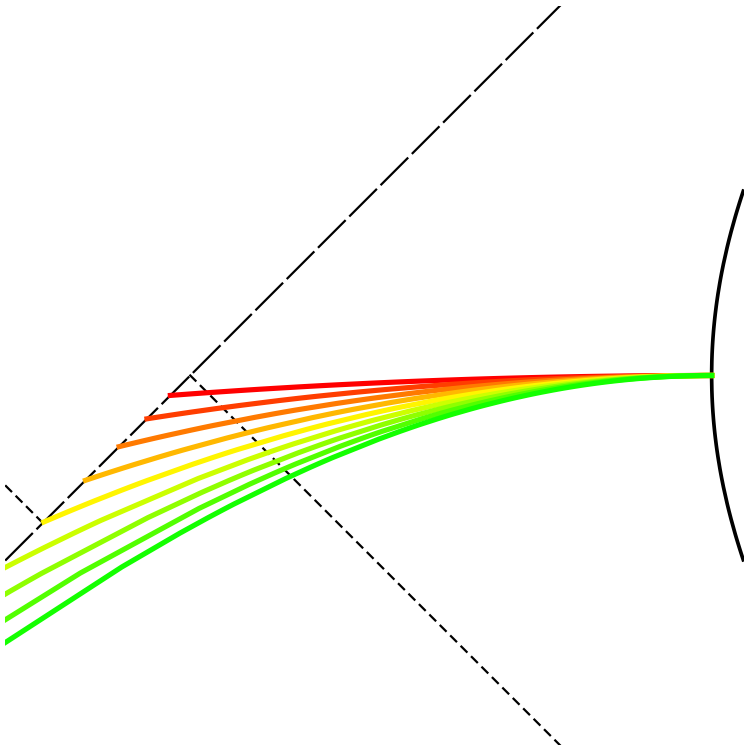

Figure 2.7: Geodesics for $L = 0$ and $E = -0.05, -0.1, \ldots, -0.45$. The red, topmost geodesic is for $E = -0.05$, with the hue changing gradually as $-E$ increases. Note that the geodesics all pass through the past horizon and reach a turning point before hitting the shock.

If we now calculate geodesics for a sufficient number of values of $E$ then we can estimate the value of $E$ required to hit any particular point on the shock. This allows us to calculate the length of full geodesics across the shock. If the perturbation gives a step change of $\alpha$ in the $V$ coordinate upon crossing the shock, then for each value of $V_{\text{shock}}$ we sum the length of geodesics from the right boundary to $(U, V) = (0, V_{\text{shock}})$ and from the left boundary to $(U, V) = (0, V_{\text{shock}} + \alpha)$. If we do this for, for example, $\alpha = 4$, then we obtain the results in figure 2.8. The lack of any extrema except for the one expected by symmetry, at $V_{\text{shock}} = -\alpha/2$, repeated for other values of $\alpha$, indicates that the geodesics joining matching points on the two boundaries cross the shock at the centre of the conformal diagram. This allows us to easily plot the geodesic length against $\alpha$, as in figure 2.9.

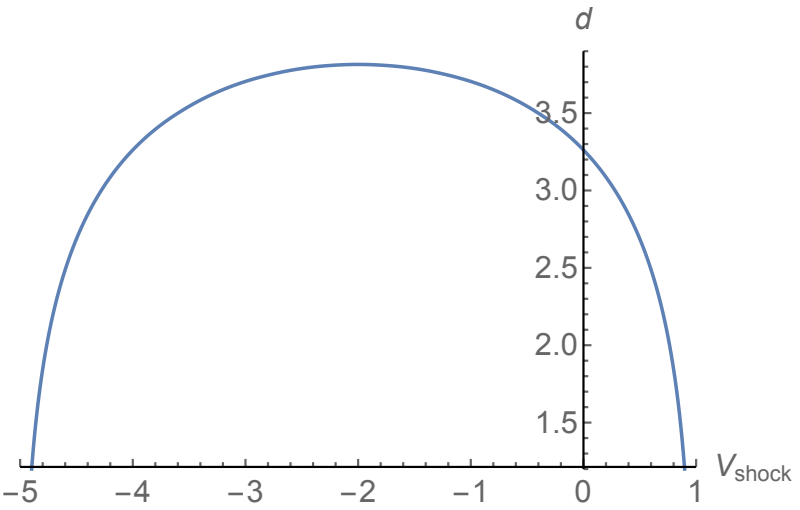


Figure 2.8: The sum of geodesic lengths from $(U, V, \phi) = (-1, 1, 0)$ to $(U, V, \phi) = (0, V_{\text{shock}}, 0)$ to the right of the shock and $(U, V, \phi) = (1, -1, 0)$ to $(U, V, \phi) = (0, V_{\text{shock}} + \alpha, 0)$ to the left, plotted against $V_{\text{shock}}$ for $\alpha = 4$. Geodesic length is extremal only at the centre of the perturbed conformal diagram at $V_{\text{shock}} = -\alpha/2$.

We see that the geodesic length increases monotonically with $\alpha$, becoming significant only for $\alpha$ of order one. Thus, as in the rotating case, the effect of the perturbation on correlation functions and mutual information at $t = 0$ is determined by the scrambling time at which $\alpha$ becomes of order one, $t_s \sim \kappa^{-1} \ln(r_+/\Delta r_+)$.

## 2.5 The butterfly effect in higher dimensions

Our investigations, and the original work on the butterfly effect by Shenker and Stanford [72], have focused on black holes in three bulk dimensions, corresponding to two-dimensional field theories. It would seem useful to extend the discussion to higher dimensions, as in the study of mutual information by Leichenauer [47]. However, there is a significant obstacle to doing so for correlation function calculations. In more than three bulk dimensions, the correlation functions in the unperturbed thermofield double state for $t \neq 0$ are not correctly reproduced by considering real geodesics in the real Lorentzian geometry; one needs to take complexified geodesics into account. This is shown by Fidkowski et al. [29], where it is revealed that, when considering equal-time correlation functions, the geodesics in the real Lorentzian geometry become null at some boundary time $t = -t_*$. This would correspond to a singular correlation function.

The correlations we have been considering in the perturbed black hole are at $t = 0$, but the calculation involves a geodesic on the right which goes from $t = 0$ on the boundary to a point on the shock at $V = -\alpha/2$ (and on the left, from $t = 0$

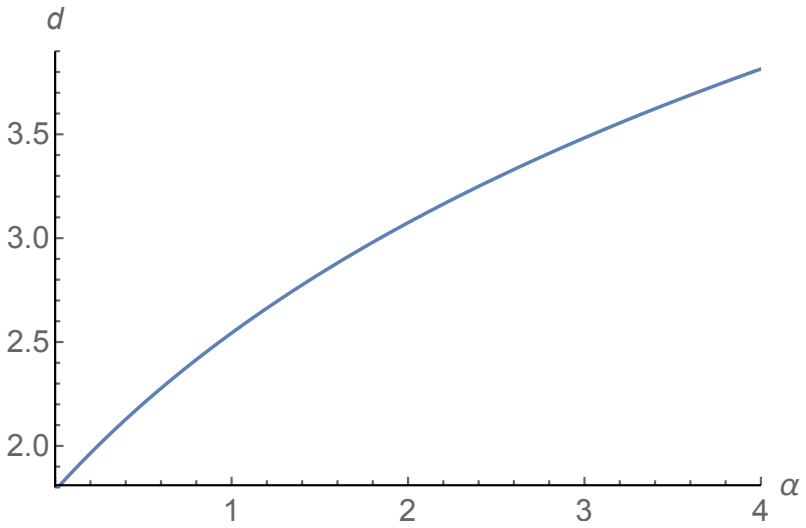


Figure 2.9: Geodesic length across the shock, plotted against the strength of the shock as given by $\alpha$.

on the boundary to a point on the shock at $V = \alpha/2$). If we considered extending this geodesic to the other boundary in the unperturbed geometry, it would meet the other boundary at some $t = -t_0$. Thus, this is just a time-translated version of the geodesic that Fidkowski et al. [29] concluded was not relevant to the calculation of the correlator on the real sheet.

The problem with using geodesics in the uncomplexified spacetime is further signalled by the fact that when we consider the geodesic from the boundary to the shock as a function of $\alpha$, there is a critical value of $\alpha$ beyond which there is no longer a spacelike geodesic which connects $t = 0$ on the boundary to $V = -\alpha/2$ on the shock. This is illustrated in figure 2.10. This critical value of $\alpha$ should correspond to the critical time $t_*$ in the work of Fidkowski et al. [29].

Thus, in higher dimensions, to calculate correlators in the perturbed geometry in the geodesic approximation, we would need to use complexified geodesics. However, the shock wave spacetime is not an analytic solution, so it does not have a unique complex extension allowing us to calculate the lengths of these complex geodesics. This problem could perhaps be addressed by moving away from the shock wave approximation and modelling the effects of the perturbation as some smooth deformation, but this will lead to considerable technical complication, so we leave this for future work.

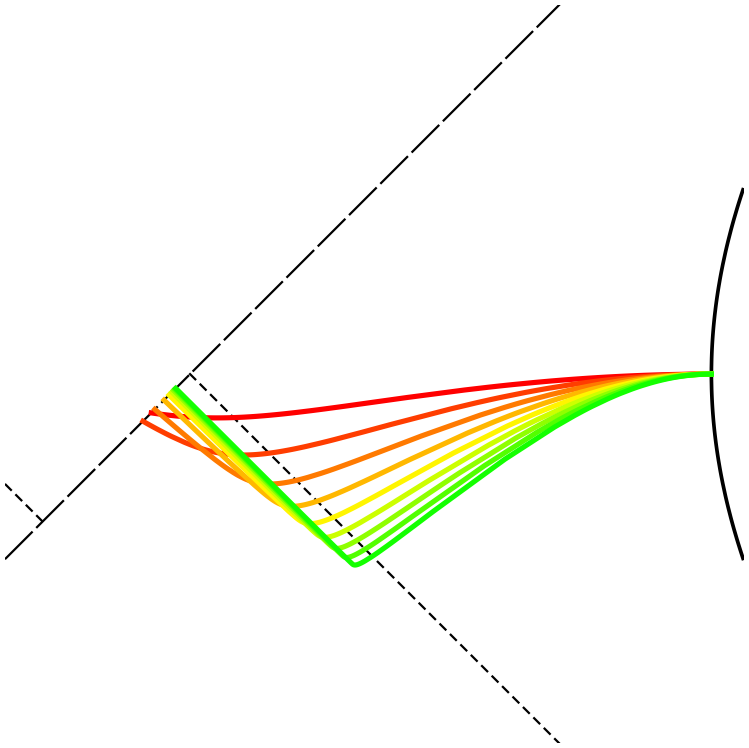

Figure 2.10: Geodesics for $L = 0$ and $E = -0.5, -1, \ldots, -4.5$ for the simple 3+1 dimensional black hole. The black hole mass, $M$, and the AdS length, $l$, are both set to 1. The red geodesic is for $E = -0.5$, with the hue changing gradually as $-E$ increases. As $-E$ increases, the intersection with the shock moves away from $V = 0$, reaches a critical point and then moves back towards, but does not reach, $V = 0$.

# Chapter 3

# Divergences in Holographic Complexity

## 3.1 Introduction

As mentioned in chapter 1, it was found that certain geometric features in the bulk could not be described simply in terms of correlation functions or entanglement entropy in the boundary theory. In particular, the continued expansion of the Einstein-Rosen bridge long after the boundary theory thermalizes, led Susskind [81] to propose a new relation between the bulk geometry and the quantum computational complexity of the boundary state. This proposal was later refined into the CV [79, 83, 82] and CA [18, 17] conjectures.

Evidence supporting these conjectures came from the study of black hole spacetimes, with a focus on the *rate of change* of the complexity. Both conjectures produce results for the complexity that grow linearly in time with

$$\frac{d\mathcal{C}}{dt} \propto M. \tag{3.1.1}$$

This is consistent with general expectations for the behaviour for excited states in the field theory. Moreover, the results saturated a proposed bound on the growth of complexity [17, 48], as predicted by a conjecture that black holes are not only the fastest scramblers in nature but also the fastest information processors. However, this emphasis on the rate of change of complexity meant that the divergences in complexity were effectively ignored — they cancelled in the calculation of the rate of change, given the static boundary spacetime.

In this chapter, prior to considering complexity for field theories on de Sitter boundaries, we look in more detail at the divergence structure of the two forms of holographic complexity. In both the CV and CA conjectures there are UV divergences, as the volume or action of the spacetime region in the bulk is divergent

near the boundary. We expect that, as for the holographic entanglement entropy [70, 69], these divergences are physical, signalling divergent contributions to the complexity associated with the UV degrees of freedom in the field theory. For the entanglement entropy, the leading divergence is proportional to the area of the entangling surface, and this can be understood as reflecting entanglement of UV modes across this boundary [15, 77]. While a detailed understanding of the divergences of the complexity from the field theory perspective does not yet exist, we can study the divergences in the holographic calculation, and see if they have a reasonable form. It is also interesting to compare the divergences between the CV and CA prescriptions, and see to what extent they compute different versions of complexity.

As our work on the divergence structure of the holographic complexity was completed, a preprint [20] of a paper appeared that also studied these divergences. Our research into these divergences, presented in this chapter, adds a simple observation to that work. There is a counterterm identified by Lehner et al. [46] that, when added to the action, cancels a coordinate-dependence in that prescription for the action. We find that adding this contribution also cancels the leading divergence in the CA prescription, so that the divergence structure of this action is the same as in the CV case. The leading divergence in both cases is then proportional to the volume of the boundary time slice, which appears reasonable from a field theory perspective. Considering subleading contributions, we find that in both cases they can be expressed in terms of the geometry of the boundary slice, but the CV and CA prescriptions differ.

Having already reviewed the CV and CA conjectures and the prescription for calculating the action [46] in chapter 1, we start by considering the divergences in the CV and CA calculations for AdS in Poincaré coordinates in section 3.2, showing how including the counterterm cancels the leading divergence in the CA calculation. Section 3.3 considers subleading contributions, showing that they have similar structures, depending on local geometric invariants of the boundary geometry, but noting that the two prescriptions will differ in general. This difference is illustrated in section 3.4 where we study the computation on global AdS.

## 3.2 UV divergences for AdS in Poincaré coordinates

The simplest case to consider is $\mathrm{AdS}_{d+1}$ in Poincaré coordinates,

$$ds^2 = \frac{\ell^2}{z^2}(dz^2 - dt^2 + d\vec{x}^2), \tag{3.2.1}$$

which is dual to the field theory in flat space. We consider a $d+1$ dimensional AdS space, with a $d$ dimensional boundary. If we ask for the complexity of the field theory on the $t=0$ surface, cut off at $z=\epsilon$, the Wheeler-DeWitt patch lies between $t=z-\epsilon$ and $t=-(z-\epsilon)$, as shown in figure 3.1. Note that although

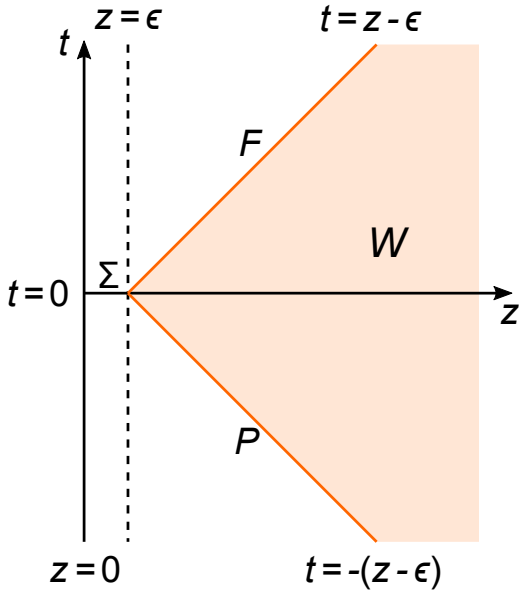


Figure 3.1: The Wheeler-DeWitt patch, $W$, in Poincaré coordinates, showing future and past boundaries $F$ and $P$ and the surface $\Sigma$ at $t=0, z=\epsilon$.

these coordinates do not cover the full spacetime, the Wheeler-DeWitt patch lies inside the region covered by this coordinate patch, as shown in figure 3.2, so we can calculate its action in these coordinates.

For the CV conjecture, the maximal volume slice with boundary at $t=0$ is simply the $t=0$ surface in the bulk, whose volume is

$$V(B) = \int dz\, d^{d-1}x\, \sqrt{h} = \ell^d V_{\vec{x}} \int_\epsilon^\infty \frac{dz}{z^d} = \frac{\ell^d V_{\vec{x}}}{(d-1)\epsilon^{d-1}}, \tag{3.2.2}$$

where $V_{\vec{x}}$ is the IR divergent coordinate volume in the $\vec{x}$ directions. Thus, the complexity calculated according to the CV prescription is, up to an overall constant,

$$\mathcal{C}_{\mathrm{V}} = \frac{\ell^{d-1} V_{\vec{x}}}{(d-1) G_{\mathrm{N}} \epsilon^{d-1}}. \tag{3.2.3}$$

This is proportional to the volume of the space the field theory lives in, in units of the cutoff. This has both an IR and a UV divergence, which is physically reasonable if we think of the complexity as defined using some product lattice state as the reference state. A Hadamard state in the field theory will not have such a product structure; the absence of high energy excitations implies short range entanglement/correlation in the state. Setting up this entangled state from the reference product state would

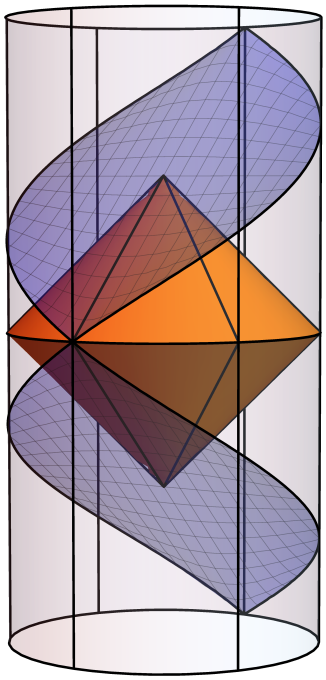

Figure 3.2: AdS, showing the region covered by Poincaré coordinates and the Wheeler-DeWitt patch of the $t = 0$ surface.

require a number of elementary operations that is expected to grow proportional to the number of lattice sites.

Turning to the CA conjecture, consider the Wheeler-DeWitt patch of this cutoff surface.[1] Referring back to (1.3.3), the action of the Wheeler-DeWitt patch with the prescription of Lehner et al. [46] is

$$S_W = \int_W (R - 2\Lambda)\sqrt{-g}\, dV - 2\int_F \kappa\, dS\, d\lambda + 2\int_P \kappa\, dS\, d\lambda - 2\oint_\Sigma a\, dS, \tag{3.2.4}$$

where $F$ ($P$) is the future (past) null boundary of the Wheeler-DeWitt patch, and $\Sigma$ is the surface at $t = 0$, $z = \epsilon$, as shown in figure 3.1. The light cones of the boundary surface are at $t = \pm(z - \epsilon)$, and $R - 2\Lambda = -2d/\ell^2$, so the volume integral is

$$S_{\text{Vol}} = -2\frac{d}{\ell^2}\int_\epsilon^\infty dz \int_{-(z-\epsilon)}^{z-\epsilon} dt\, \frac{\ell^{d+1}}{z^{d+1}} V_{\vec{x}} = -4\frac{\ell^{d-1} V_{\vec{x}}}{(d-1)\epsilon^{d-1}}. \tag{3.2.5}$$

This has a very similar structure to the volume in (3.2.2), but this term is negative, so it is clearly important to include the boundary contributions identified by Lehner et al. [46] to obtain a sensible result for the complexity.

In calculating (3.2.4), it is convenient to adopt an affine parametrization of

[1] We could alternatively take the original Wheeler-DeWitt patch of the surface at $t = 0, z = 0$ and cut off the corner at $z = \epsilon$, producing a small timelike boundary component. This would produce a different set of coefficients for subleading divergences [20].

the null surfaces, so that the integrals over the future and past boundaries do not contribute. Let us take the affine parameters along the null surfaces to be

$$\lambda = -\frac{\ell^2}{\alpha z} \text{ on } F, \quad \lambda = \frac{\ell^2}{\beta z} \text{ on } P, \tag{3.2.6}$$

where we introduce the arbitrary constants $\alpha, \beta$ to exhibit explicitly the remaining coordinate dependence. The future directed tangents to surfaces $F$ and $P$ are then

$$k = \frac{\alpha z^2}{\ell^2}(\partial_t + \partial_z), \qquad \bar{k} = \frac{\beta z^2}{\ell^2}(\partial_t - \partial_z). \tag{3.2.7}$$

Using (1.3.4), i.e. $a = \ln\left|k.\bar{k}/2\right|$, we find that the boundary corner term is

$$S_\Sigma = -2\frac{\ell^{d-1}V_{\vec{x}}}{\epsilon^{d-1}}\ln(\alpha\beta\epsilon^2/\ell^2). \tag{3.2.8}$$

Thus, the action calculated according to (3.2.4) is

$$S_W = \frac{\ell^{d-1}V_{\vec{x}}}{\epsilon^{d-1}}\left[-4\ln(\epsilon/\ell) - 2\ln(\alpha\beta) - \frac{4}{d-1}\right]. \tag{3.2.9}$$

This has two undesirable features: it depends on the normalization $\alpha$, $\beta$ of the affine parameters on the two null surfaces, and it diverges like $\epsilon^{-(d-1)}\ln\epsilon$, which is faster than the volume of the space the field theory lives in. These effects drop out if we consider the rate of change of the complexity as in (3.1.1), but they are both problematic if we want to consider the action as dual to the actual complexity of the state. The first implies that the identification will require some choice of normalization for the affine parameters, which seems strange; these are just coordinates and should have no physical content. The second implies the complexity would have a stronger than volume divergence, which seems not so easy to understand in terms of a simple lattice model.

Fortunately, both these problems are removed once we include the additional contribution (1.3.5). The metric on F has $\sqrt{\gamma} = \ell^{d-1}/z^{d-1}$, so the expansion is

$$\Theta = \frac{1}{\sqrt{\gamma}}\frac{\partial\sqrt{\gamma}}{\partial\lambda} = -\frac{1}{\sqrt{\gamma}}\alpha\frac{z^2}{\ell^2}\frac{\partial\sqrt{\gamma}}{\partial z} = (d-1)\alpha\frac{z}{\ell^2}, \tag{3.2.10}$$

with the result that, setting $c = \ell$ in (1.3.5), the surface counterterms are given by

$$\begin{aligned} S_F &= -2(d-1)\ell^{d-1}V_{\vec{x}}\int z^{-(d-2)}\ln\left(\alpha(d-1)z/\ell\right)\alpha d\lambda \\ &= 2(d-1)\ell^{d-1}V_{\vec{x}}\int_\epsilon^\infty z^{-d}\ln\left(\alpha(d-1)z/\ell\right)dz \\ &= 2\frac{\ell^{d-1}}{\epsilon^{d-1}}V_{\vec{x}}\left(\ln\left(\alpha(d-1)\epsilon/\ell\right) + \frac{1}{d-1}\right), \end{aligned} \tag{3.2.11}$$

and

$$S_P = 2\frac{\ell^{d-1}}{\epsilon^{d-1}} V_{\vec{x}} \left( \ln\left(\beta(d-1)\epsilon/\ell\right) + \frac{1}{d-1} \right). \tag{3.2.12}$$

We therefore get

$$S = S_W + \Delta S = S_{\text{Vol}} + S_\Sigma + S_F + S_P = 4\frac{\ell^{d-1}}{\epsilon^{d-1}} V_{\vec{x}} \ln(d-1). \tag{3.2.13}$$

The dependence on $\alpha$ and $\beta$ cancels out by construction, as the additional terms were introduced to eliminate the coordinate dependence in the unadjusted action (1.3.3). The surprise is that this also leads to the cancellation of the logarithmic divergence.[2] This provides a strong additional support for the idea that the counterterm (1.3.5) should be included in the calculation of the action. The result now has the same structure as that obtained in the CV calculation (3.2.3); since we do not understand the relation between the complexity and spacetime very precisely, the difference in the overall coefficient is not particularly significant.

## 3.3 Subleading divergences

If we consider asymptotically AdS spacetimes, there will also be subleading divergences. It is interesting to consider these contributions and investigate whether the cancellation of the leading logarithmic divergence, through the addition of the surface counterterms, also extends to subleading logarithmic terms. It is also interesting to compare the structure of divergences in the CV and CA prescriptions.

We consider an asymptotically $\text{AdS}_{d+1}$ solution of the vacuum Einstein equations. The metric in the asymptotic region can then be written in the Fefferman-Graham gauge [28, 30]

$$ds^2 = \frac{\ell^2}{z^2}(dz^2 + g_{\mu\nu}(x^\mu, z)\, dx^\mu\, dx^\nu), \tag{3.3.1}$$

where the metric along the boundary directions has a power series expansion in $z$,

$$g_{\mu\nu}(x^\mu, z) = g^{(0)}_{\mu\nu}(x^\mu) + z^2 g^{(1)}_{\mu\nu}(x^\mu) + \dots. \tag{3.3.2}$$

We can give a simple general argument which shows that the cancellation of the leading logarithmic term extends to all the terms of the form $\epsilon^{-n}\log\epsilon$. Logarithmic

[2] For the case $d = 1$, that is $\text{AdS}_2$, the null surfaces are one-dimensional, and there is no expansion, so we cannot define a term analogous to (1.3.5) to cancel the logarithmic divergence. In this case the CV calculation is also logarithmically divergent. It would be interesting to understand this better, as this case will emerge if we want to apply these complexity ideas to near-horizon geometries of near-extremal black holes.

divergences come from the corner contribution,

$$S_\Sigma = -2 \oint_\Sigma \ln \left| k \cdot \bar{k}/2 \right| \sqrt{\gamma}\, d^{d-1}\sigma, \tag{3.3.3}$$

and from the counterterm contributions on the two null surfaces. Considering the future surface, setting $c = \ell$ in (1.3.5), we get

$$S_F = -2 \int \Theta \ln |\ell\Theta| \sqrt{\gamma}\, d^{d-1}x\, d\lambda. \tag{3.3.4}$$

Now using the fact that the expansion is $\Theta = \frac{1}{\sqrt{\gamma}} \frac{\partial \sqrt{\gamma}}{\partial \lambda}$, we can rewrite this as

$$S_F = -2 \int \partial_\lambda \sqrt{\gamma} \ln |\ell\Theta|\ d^{d-1}x\, d\lambda, \tag{3.3.5}$$

and integrate by parts on $\lambda$. Since $\Sigma$ is a past endpoint of the future surface, we obtain

$$S_F = 2 \oint_\Sigma \sqrt{\gamma} \ln |\ell\Theta|\ d^{d-1}\sigma + 2 \int \sqrt{\gamma} \frac{\partial_\lambda \Theta}{\Theta}\, d^{d-1}x\, d\lambda, \tag{3.3.6}$$

dropping a boundary term at the other boundary of the null surface which is irrelevant to the asymptotic calculation. The second term will only contribute power-law divergences, so the logarithmic divergences will come solely from the integral over $\Sigma$. Note also that it is this integral over $\Sigma$ which cancels the coordinate-dependence in (1.3.3); the second term is coordinate-independent.[3] There is a similar contribution from the past surface;

$$S_P = 2 \int \partial_\lambda \sqrt{\gamma} \ln |\ell\Theta|\ d^{d-1}x\, d\lambda, \tag{3.3.7}$$

and the boundary term has the opposite sign because $\Sigma$ is a future boundary of the past surface, so

$$S_P = 2 \oint_\Sigma \sqrt{\gamma} \ln |\ell\Theta|\ d^{d-1}\sigma - 2 \int \sqrt{\gamma} \frac{\partial_\lambda \Theta}{\Theta}\, d^{d-1}x\, d\lambda. \tag{3.3.8}$$

The logarithmic divergences in the full action are then contained in the terms involving integrals on $\Sigma$,

$$S = \ldots + 2 \oint_\Sigma \left( \ln |\ell\Theta_F| + \ln |\ell\Theta_P| - \ln \left| k \cdot \bar{k}/2 \right| \right) \sqrt{\gamma}\, d^{d-1}\sigma. \tag{3.3.9}$$

We know from the previous calculation that the leading order logarithmic term cancels. Subleading terms coming from the expansion of $\sqrt{\gamma}$ will then also cancel. Subleading terms in the argument of the logarithm will give power law divergences,

[3] In fact, one could take an alternative prescription for resolving the issues in (1.3.3) where one just added the first term in (3.3.6), rather than the whole expression (1.3.5).

once we expand $\ln(\epsilon+B\epsilon^2+\ldots) = \ln\epsilon+\ln(1+B\epsilon+\ldots) \approx \ln\epsilon+B\epsilon+\ldots$. Thus, there are no subleading terms of the form $\epsilon^{-n}\ln\epsilon$; once we include (1.3.5) the divergences are a power series expansion in $\epsilon$.[4]

We will now extend the explicit calculation of the first subleading corrections to the action of Carmi et al. [20] to include the additional contribution along the null surfaces. We will see explicitly that the logarithmic terms cancel, as predicted by the general argument above. We assume we are in $d > 2$ where the term of order $z^2$ is determined locally by the boundary metric $g^{(0)}_{\mu\nu}$, [23, 76]

$$g^{(1)}_{\mu\nu}(x^\mu) = -\frac{\ell^2}{(d-2)}\left(R_{\mu\nu}\left[g^{(0)}\right] - \frac{g^{(0)}_{\mu\nu}}{2(d-1)}R\left[g^{(0)}\right]\right), \tag{3.3.10}$$

where $R_{\mu\nu}$ and $R$ are the Ricci tensor and Ricci scalar for the boundary metric. It should be straightforward to extend the analysis to further subleading orders, but we will see interesting differences already at the first subleading order.

We consider a boundary slice at $t = 0$, in the cutoff surface at $z = \epsilon$, and calculate subleading divergences in the complexity. As in Carmi et al. [20], we restrict consideration to cases where the boundary metric is

$$g^{(0)}_{\mu\nu}\,dx^\mu\,dx^\nu = -dt^2 + h_{ab}(t,\sigma^a)\,d\sigma^a\,d\sigma^b. \tag{3.3.11}$$

This is general enough to include many cases of interest, and considerably simplifies the determination of the Wheeler-DeWitt patch.

Carmi et al. [20] determined the subleading contributions to the volume of the maximal slice, finding them to be

$$\mathcal{C}_{\rm V} = \frac{\ell^{d-1}}{(d-1)G_{\rm N}\epsilon^{d-1}}\int d^{d-1}\sigma\,\sqrt{h}\Bigg[1 - \frac{d-1}{2(d-2)(d-3)}\epsilon^2\left(R^a_a - \frac{1}{2}R - \frac{(d-2)^2}{(d-1)^2}K^2\right) + \ldots\Bigg], \tag{3.3.12}$$

where $h$ is the determinant of the metric $h_{ab}$ in (3.3.11) at $t = 0$, $R^a_a = h^{ab}R_{ab}$ is the trace of the projection of the boundary Ricci tensor into the $t = 0$ surface, and $K$ is the trace of the extrinsic curvature of the $t = 0$ surface in the boundary metric (3.3.11). Thus, the first subleading divergence can be expressed in terms of local geometric features of the boundary metric. Carmi et al. [20] also evaluated the first

[4] This argument is valid for all the terms of the form $\epsilon^{-n}\log\epsilon$ for $n > 0$; once we reach the order in the Fefferman-Graham expansion where we encounter the free data in the asymptotic expansion, there may be contributions to either CV or CA calculations at order $\log\epsilon$.

subleading contributions to the action (1.3.3), obtaining

$$\begin{aligned}\mathcal{C}_{\rm A}(S_W) = &-\frac{\ell^{d-1}}{4\pi^2 G_{\rm N}(d-1)\epsilon^{d-1}}\int d^{d-1}\sigma\,\sqrt{h}\Big[1\\ &+\frac{\epsilon^2}{4(d-2)(d-3)}\left(4K^2+4K_{ab}K^{ab}+(d-7)R-2(d-3)R^a_a\right)\Big]\\ &+\frac{\ell^{d-1}}{4\pi^2 G_{\rm N}\epsilon^{d-1}}\log\left(\frac{\ell}{\sqrt{\alpha\beta}\epsilon}\right)\int d^{d-1}\sigma\,\sqrt{h}\left[1-\epsilon^2\frac{1}{2(d-2)}\left(R^a_a-\frac{1}{2}R\right)\right]+\ldots\end{aligned} \tag{3.3.13}$$

We want to consider the effect of adding the counterterm (1.3.5).

A key feature of the calculation of Carmi et al. [20] is that the assumption that the boundary metric has the form (3.3.11) implies that at first subleading order, the tangents to the null generators take the form

$$k=\frac{\alpha}{\ell^2}(z^2\partial_z+k^t\partial_t),\qquad \bar{k}=\frac{\beta}{\ell^2}(-z^2\partial_z+k^t\partial_t), \tag{3.3.14}$$

where $k^t$ is determined by requiring these to be null vectors, $k^\mu k_\mu = 0$, which gives $k^t = z^2 g_{tt}^{-1/2}$. This implies that the form of the affine parameter in (3.2.6) is unchanged to first subleading order.

Near the boundary, the induced metric on the surfaces of constant $\lambda$ in the null surfaces is thus $\gamma_{ab} = z^{-2}h_{ab} + g^{(1)}_{ab} + \ldots$. Following Carmi et al. [20], we write

$$\sqrt{\gamma}=\frac{\ell^{d-1}}{z^{d-1}}\sqrt{h}\left(\left[1+q_0^{(2)}z^2+\ldots\right]+\left[q_1^{(0)}+\ldots\right]t+\left[q_2^{(0)}+\ldots\right]t^2+\ldots\right), \tag{3.3.15}$$

keeping the first terms in an expansion for small $z$ and $t$, where $h$ is the determinant of $h_{ab}(\sigma^a, t=0)$. Along the null surface $t=(z-\epsilon)+\mathcal{O}(z^3)$,

$$\sqrt{\gamma}=\frac{\ell^{d-1}}{z^{d-1}}\sqrt{h}\left(1+q_1^{(0)}(z-\epsilon)+q_0^{(2)}z^2+q_2^{(0)}(z-\epsilon)^2+\ldots\right), \tag{3.3.16}$$

$$\begin{aligned}\partial_z\sqrt{\gamma}=&-\frac{\ell^{d-1}}{z^d}\sqrt{h}\Big((d-1)+q_1^{(0)}\left((d-2)z-(d-1)\epsilon\right)+q_0^{(2)}(d-3)z^2\\ &+q_2^{(0)}\left((d-3)z^2-2(d-2)z\epsilon+(d-1)\epsilon^2\right)+\ldots\Big),\end{aligned} \tag{3.3.17}$$

so the expansion is

$$\Theta=\frac{\alpha z}{\ell^2}\left[(d-1)-q_1^{(0)}z-2q_0^{(2)}z^2-2q_2^{(0)}z(z-\epsilon)+q_1^{(0)2}z(z-\epsilon)+\ldots\right] \tag{3.3.18}$$

Performing the integral over $z$, one finds

$$S_F = 2\frac{\ell^{d-1}}{\epsilon^{d-1}}\int_\Sigma d^{d-1}\sigma\,\sqrt{h}\Bigg[\ln(\alpha(d-1)\epsilon/\ell)(1+q_0^{(2)}\epsilon^2) + \frac{1}{(d-1)}\left(1-q_1^{(0)}\epsilon - q_0^{(2)}\frac{d-1}{d-3}\epsilon^2 - 2\frac{q_2^{(0)}}{d-3}\epsilon^2 + q_1^{(0)2}\frac{1}{2(d-3)}\epsilon^2\right)\Bigg]. \tag{3.3.19}$$

$S_P$ will have the same form, but with the sign of $q_1^{(0)}$ reversed, as the past surface is $t = -(z-\epsilon) + \mathcal{O}(z^3)$. Thus, the correction to the action is

$$S_F + S_P = 4\frac{\ell^{d-1}}{\epsilon^{d-1}}\int_\Sigma d^{d-1}\sigma\,\sqrt{h}\Bigg[\ln\left(\sqrt{\alpha\beta}(d-1)\epsilon/\ell\right)\left(1+q_0^{(2)}\epsilon^2\right) + \frac{1}{(d-1)}\left(1-q_0^{(2)}\frac{d-1}{d-3}\epsilon^2 - 2\frac{q_2^{(0)}}{d-3}\epsilon^2 + q_1^{(0)2}\frac{1}{2(d-3)}\epsilon^2\right)\Bigg]. \tag{3.3.20}$$

Using the geometric expressions obtained by Carmi et al. [20],

$$\begin{aligned} q_1^{(0)} &= K, \\ q_2^{(0)} &= \frac{1}{2}(K^2 + K_{ab}K^{ab} + R^a_a - R), \\ q_0^{(2)} &= -\frac{1}{2(d-2)}\left(R^a_a - \frac{1}{2}R\right), \end{aligned} \tag{3.3.21}$$

we can see that the logarithmic term will cancel with the contribution in (3.3.13), as expected, including the subleading correction. The power law terms will combine with those in (3.3.13) to give us a result for the complexity

$$\mathcal{C}_{\mathrm{A}}(S) = \frac{\ell^{d-1}}{4\pi^2 G_{\mathrm{N}}\epsilon^{d-1}}\int d^{d-1}\sigma\,\sqrt{h}\Bigg[\ln(d-1)\left(1-\frac{\epsilon^2}{2(d-2)}\left(R^a_a - \frac{1}{2}R\right)\right) - \frac{\epsilon^2 d}{2(d-1)(d-2)(d-3)}K^2 - \frac{\epsilon^2}{(d-2)(d-3)}K_{ab}K^{ab} + \frac{\epsilon^2 d}{2(d-1)(d-2)(d-3)}R\Bigg]. \tag{3.3.22}$$

We see that this has a similar structure to the CV result (3.3.12), but with different coefficients for the subleading terms.

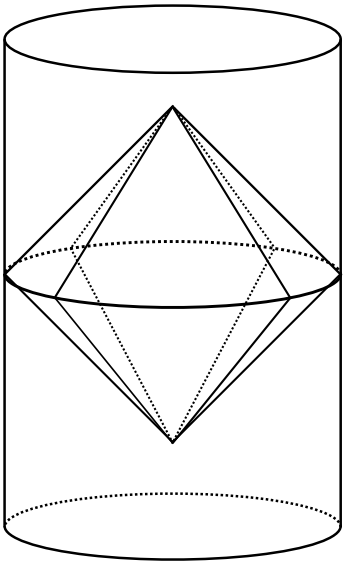

Figure 3.3: The Wheeler-DeWitt patch in global AdS.

## 3.4 Global AdS

A simple example which illustrates the difference between CV and CA is to consider pure AdS in global coordinates,

$$ds^2 = \frac{\ell^2}{\cos^2\theta}(-dt^2 + d\theta^2 + \sin^2\theta\, d\Omega_{d-1}^2). \tag{3.4.1}$$

We consider a slice of the boundary at $t = 0$, cutoff at $\theta = \theta_{\text{cut}} = \pi/2 - \epsilon$. The maximal volume slice is again $t = 0$ in the bulk, and the volume is simply

$$V(B) = \int d\theta\, d\Omega\, \sqrt{h} = \ell^d \Omega_{d-1} \int_0^{\theta_{\text{cut}}} \frac{d\theta}{\cos\theta} \tan^{d-1}\theta, \tag{3.4.2}$$

where $\Omega_{d-1}$ is the volume of a unit $S^{d-1}$.

We again calculate the action of the Wheeler-DeWitt patch of the cutoff boundary at $\theta = \theta_{\text{cut}}$, as depicted in figure 3.3. The future boundary is at $t = \theta_{\text{cut}} - \theta$, while the past boundary is at $t = \theta - \theta_{\text{cut}}$. The volume term in (3.2.4) is

$$\begin{aligned} S_{\text{Vol}} &= -\frac{4d}{\ell^2} \int_0^{\theta_{\text{cut}}} dt' \int_0^{t'} d\theta \int d\Omega_{d-1}\, \sqrt{-g} \\ &= -4d\Omega_{d-1}\ell^{d-1} \int_0^{\theta_{\text{cut}}} dt' \int_0^{t'} d\theta\, \frac{\sin^{d-1}\theta}{\cos^{d+1}\theta} \\ &= -4\Omega_{d-1}\ell^{d-1} \int_0^{\theta_{\text{cut}}} dt'\, \tan^d t'. \end{aligned} \tag{3.4.3}$$

In the first step, we wrote the volume term as twice the integral over the future half of the Wheeler-DeWitt patch. We choose an affine parameter $\lambda$, so that the

integrals over the future and past boundaries in the unadjusted action (1.3.3) do not contribute. An appropriate parameter is $\lambda = -\alpha^{-1}\ell \tan\theta$ on $F$ and $\lambda = \beta^{-1}\ell\tan\theta$ on $P$, where we have introduced the arbitrary parameters $\alpha$, $\beta$ purely so that we can see that they will cancel out once we add the counterterm. The future-pointing tangent is then

$$k = \frac{\alpha}{\ell}\cos^2\theta(\partial_t - \partial_\theta) \tag{3.4.4}$$

on $F$ and

$$\bar{k} = \frac{\beta}{\ell}\cos^2\theta(\partial_t + \partial_\theta) \tag{3.4.5}$$

on $P$, so the corner contribution to the action is

$$S_\Sigma = -2\Omega_{d-1}\ell^{d-1}\tan^{d-1}\theta_{\rm cut}\ln\left(\alpha\beta\cos^2\theta_{\rm cut}\right). \tag{3.4.6}$$

Adding the counterterm, the expansion on $F$ is

$$\begin{aligned}\Theta &= \frac{1}{\sqrt{\gamma}}\frac{\partial\sqrt{\gamma}}{\partial\lambda} = -\frac{1}{\sqrt{\gamma}}\frac{\alpha}{\ell}\cos^2\theta\frac{\partial\sqrt{\gamma}}{\partial\theta} = -\frac{\alpha}{\ell}\cos^2\theta\cot^{d-1}\theta\partial_\theta(\tan^{d-1}\theta)\\ &= -\frac{\alpha}{\ell}(d-1)\cot\theta,\end{aligned} \tag{3.4.7}$$

and similarly on $P$,

$$\Theta = \frac{\beta}{\ell}(d-1)\cot\theta. \tag{3.4.8}$$

Thus the surface terms are

$$\begin{aligned}S_F &= -2\Omega_{d-1}\ell^{d-1}\int\Theta\ln|\Theta|\tan^{d-1}\theta\,d\lambda\\ &= 2(d-1)\Omega_{d-1}\ell^{d-1}\int_0^{\theta_{\rm cut}}\frac{\tan^{d-2}\theta}{\cos^2\theta}\ln\left(\alpha(d-1)\cot\theta\right)\,d\theta,\\ &= 2\Omega_{d-1}\ell^{d-1}\left[\tan^{d-1}\theta_{\rm cut}\ln\left(\alpha(d-1)\cot\theta_{\rm cut}\right) + \frac{1}{(d-1)}\tan^{d-1}\theta_{\rm cut}\right]\end{aligned} \tag{3.4.9}$$

and

$$\begin{aligned}S_P &= 2\Omega_{d-1}\ell^{d-1}\int\Theta\ln|\Theta|\tan^{d-1}\theta\,d\lambda\\ &= 2\Omega_{d-1}\ell^{d-1}\left[\tan^{d-1}\theta_{\rm cut}\ln\left(\beta(d-1)\cot\theta_{\rm cut}\right) + \frac{1}{(d-1)}\tan^{d-1}\theta_{\rm cut}\right]\end{aligned} \tag{3.4.10}$$

so in total

$$\begin{aligned}S &= S_V + \Delta S = S_{\rm Vol} + S_\Sigma + S_F + S_P\\ &= -4\Omega_{d-1}\ell^{d-1}\int_0^{\theta_{\rm cut}}dt'\,\tan^d t' + 4\Omega_{d-1}\ell^{d-1}\tan^{d-1}\theta_{\rm cut}\left(\ln(d-1) + \frac{1}{d-1}\right).\end{aligned} \tag{3.4.11}$$

We see that while the leading UV divergence is the same as for the volume (3.4.2),

the integrals are different, so the functional dependence on $\theta_{\text{cut}}$ is different for CV and CA. The two conjectures for the complexity are inequivalent. However, as noted by Carmi et al. [20] (appendix C), the form of the subleading contributions in the CA calculation here depends on how we choose to cut off the Wheeler-DeWitt patch, so it is not clear how much physical meaning it carries.

# Chapter 4

# Complexity in de Sitter Space

## 4.1 Introduction

In initial studies, evidence for the CV and CA conjectures came from the study of AdS black holes, with the boundary spacetime taken to be simple Minkowski space. However, it is clearly of interest to consider holographic complexity in other settings, if only to provide additional tests for the conjectures. In this chapter, we consider solutions with are asymptotically AdS, but in a de Sitter slicing, dual to field theories in de Sitter space. This is an appealing test case, firstly because it provides a simple example where the field theory is in a time-dependent background, so we can study how the time-dependence of the complexity of the state is affected by time-dependent sources, and secondly because simple bulk duals are known.

This situation also has some features in common with the black hole case. In the field theory, we consider some de Sitter-invariant state on a de Sitter background. This is a globally pure state, but the state seen by a given observer will appear thermal. This thermal structure comes from entanglement between degrees of freedom at antipodal points in the de Sitter space, whose structure is similar to that between the two copies in a thermofield double state. In the bulk, the geometries dual to some such states have horizons, while other cases do not, so they provide another example where one can study the relation of bulk horizons and the behind the horizon geometry to the complexity. The entanglement structure in this case was investigated by Maldacena and Pimentel [52], providing important inspiration for our work. Complexity of these solutions was also previously considered by Barbón and Rabinovici [11].

In section 4.2, we discuss the general features we would expect in the complexity in de Sitter space from the field theory point of view and set up the holographic calculation, discussing general features of the asymptotically AdS spaces we consider and introducing a particular set of de Sitter $\times S^1$ examples that we will focus on. We

find that if we work in flat coordinates on the de Sitter space, the time dependence of the complexity is fixed by the de Sitter symmetry. This is a surprisingly simple behaviour, and qualitatively different from the time dependence of the entanglement entropy found by Maldacena and Pimentel [52]. For the de Sitter $\times S^1$ examples, there are explicitly known bulk geometries, which either end in a 'bubble of nothing', or have a bulk horizon, with a crunching FRW region beyond it.

In section 4.3, we discuss the calculation using the CV conjecture. We find that the growth rate of the complexity for the bubbles is smaller than for the black holes, as the spatial slice ends on the bubble. This is consistent with the proposed relation of growth rate to energy, as the bubbles have smaller energy than the black hole, although the bound is not saturated; for large bubbles the difference in complexity grows more slowly than the difference in energy.

In section 4.4, we perform calculations using the CA conjecture. We find that the growth rate for the complexity for the bubbles in this case is *larger* than for the black holes: this is due to a negative spacetime volume contribution to the action. This is contrary to the general expectations for the behaviour of the complexity. Furthermore, for small bubbles, there is a logarithmic growth in the complexity as the bubble shrinks, whereas the volume calculation approaches a finite limit. We note that the prescription we use for calculating the action is not unique, and consider options for modifying it. We give concluding remarks in section 4.5.

## 4.2 de Sitter complexity

In this section we set up the calculation of complexity for field theories in de Sitter. We first consider the expectations from the field theory side, and then describe the bulk geometries dual to field theories in de Sitter, which will be used in the following sections to evaluate the complexity using the CV and CA conjectures.

### 4.2.1 Field theory considerations

We will find it convenient to analyse the complexity in conformally flat coordinates on the de Sitter space,

$$ds^2 = \frac{1}{H^2\eta^2}(-d\eta^2 + d\vec{x}^2), \tag{4.2.1}$$

as there is a symmetry relating surfaces of different $\eta$. The surfaces of $\eta =$ constant are Cauchy surfaces for de Sitter, so we are measuring the complexity of the global pure state on the full de Sitter space. This is however a different physical question from asking about the $\tau =$ constant slices in global coordinates,

$$ds^2 = H^{-2}(-d\tau^2 + \cosh^2\tau\, d\Omega_{d-2}^2), \tag{4.2.2}$$

as they are different spacelike surfaces in the de Sitter space. It would be interesting to also study the situation in global coordinates, but we will not explore this here. We will consider the flat patch including the future boundary of de Sitter space, so in (4.2.1), $\eta \in (-\infty, 0)$, with the future conformal boundary at $\eta = 0$. We will write formulas for a $d-1$ dimensional de Sitter space, as in our most prominent examples, we take the $d$-dimensional boundary to be de Sitter$_{d-1} \times S^1$.

We have argued above that a volume law divergence for complexity in field theory is a generic expectation. In the context of de Sitter, this contribution to the complexity will grow with time, as the proper volume of the spatial slices of the universe grows. Relative to a fixed cutoff, the number of lattice sites will grow with the volume, and we would expect the UV divergent part of the complexity to be proportional to the proper volume. In the flat coordinates (4.2.1), this proper volume is infinite, due to the infinite volume in the spatial $\vec{x}$ directions. This is an IR divergence in addition to the UV divergence, as in the Poincaré-AdS calculation of the previous chapter.

In the holographic calculations, the volume of the bulk surface or action of the Wheeler-DeWitt patch will involve an integral over these spatial directions, so the IR divergence is simply the volume $V_{\vec{x}}$ in these directions, multiplied by some overall factor. It is plausible that this is true more generally, i.e. that $\mathcal{C} \propto V_{\vec{x}}$. Whenever this holds, we can use this simple relation to fix the time dependence of the complexity by symmetry. In the flat coordinates (4.2.1), there is a symmetry under $\eta \to \lambda\eta$, $\vec{x} \to \lambda\vec{x}$. The complexity of a de-Sitter invariant state should be invariant under this symmetry, which implies that if it is proportional to the spatial volume, the complexity of the state measured on a slice of fixed $\eta$ must be

$$\mathcal{C} = \frac{V_{\vec{x}}}{|\eta|^{d-2}} c(|\Psi\rangle), \tag{4.2.3}$$

where $c(|\Psi\rangle)$ is independent of time.

More generally, the holographic results for homogeneous boundary spaces will always be of the form

$$\mathcal{C} = V_\Sigma c \tag{4.2.4}$$

where $V_\Sigma$ is the proper volume of the boundary spatial slice, and $c$ is a "complexity density". In the black hole case this was a non-trivial function of time, which becomes linear at late times. For a de Sitter-invariant state the complexity density is constant by virtue of the symmetries.

This behaviour is qualitatively different to that seen in the study of the entanglement entropy in de Sitter by Maldacena and Pimentel [52]. There, the authors found that the entanglement entropy of a finite region in the $\vec{x}$ coordinates in the

spatial slice at constant $\eta$ generically has a finite part with time dependence

$$S_{\text{UV-finite}} = c_5 \frac{A_x}{\eta^{d-3}} + c_6 \log \eta + (\text{indep of } \eta), \tag{4.2.5}$$

where $A_x$ is the coordinate area, in the spatial $\vec{x}$ coordinates, of the boundary of the region considered. The first term is analogous to our result, while the second provided a signal of the existence of horizons in the bulk. The complexity is simpler because the holographic calculations always give us a complexity simply proportional to the volume $V_{\vec{x}}$. The complexity associated with subregions [1, 12, 6] could have a more complicated behaviour, but since we have less understanding of the expectations of the behaviour of subregion complexity, we will not consider it here.

This simplicity of the time dependence does not mean that everything is fixed by symmetry. As we will review below, in the holographic context there are multiple solutions with the same de Sitter asymptotics, corresponding to different de Sitter-invariant states on the same background. We would expect the difference between these states to be reflected in the complexity. Prompted by the bound (1.3.2), we will compare the difference in complexity to the difference in energy between the states.

### 4.2.2 Bulk solutions

We study the field theory holographically by considering asymptotically anti-de Sitter spacetimes with a de Sitter boundary. The simplest example is a pure conformal field theory, which is simply dual to $\text{AdS}_d$ in the de Sitter slicing,

$$ds^2 = \ell^2 \left( d\rho^2 + \frac{\sinh^2 \rho}{\eta^2} (-d\eta^2 + d\vec{x}^2) \right). \tag{4.2.6}$$

This is related to AdS in Poincaré coordinates (3.2.1) via

$$z = -\frac{\eta}{\sinh \rho}, \qquad t = \eta \coth \rho. \tag{4.2.7}$$

On the boundary, the $\eta$ and $t$ coordinates coincide, and the de Sitter and Poincaré coordinates are related simply by a conformal transformation that turns the $t = 0$ slice in Poincaré coordinates into the future boundary of the de Sitter space, with the flat patch lying in the $t < 0$ half of the Poincaré coordinates on the boundary. The de Sitter slices of constant $\rho$ in the coordinates (4.2.6) are surfaces of constant $t/z$ in the Poincaré coordinates, and there is a horizon at $\rho = 0$, as shown in figure 4.1.

More generally, for asymptotically AdS solutions, the de Sitter symmetry implies

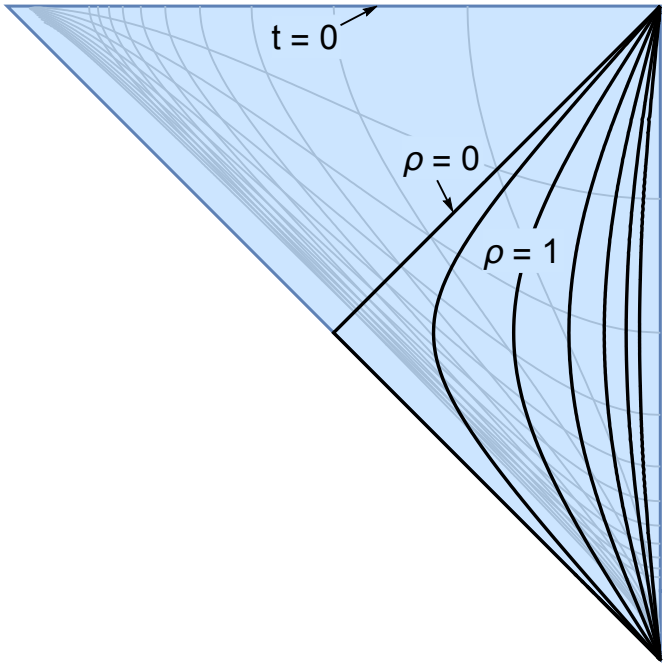


Figure 4.1: The region of AdS covered by the de Sitter slicing (4.2.6). The coordinates cover the right triangle, where surfaces of constant $\rho$ are plotted. The lower diagonal is the Poincaré horizon $z \to \infty, t \to -\infty$; the shaded region is the past half of the Poincaré patch. The de Sitter coordinates have an additional horizon at $\rho = 0$. The region beyond this can be described by an FRW geometry of the form (4.2.9). In pure AdS the horizontal line at the top is just $t = 0$ in Poincaré coordinates. In the de Sitter $\times S^1$ examples we consider later, this is a 'singularity' where the identification becomes null.

that we can write the bulk geometry as

$$ds^2 = \ell^2 \left( d\rho^2 + \frac{a^2(\rho)}{\eta^2} \left( -d\eta^2 + d\vec{x}^2 \right) \right), \tag{4.2.8}$$

for some function $a(\rho)$ such that $a \to \sinh \rho$ as $\rho \to \infty$.

There are two qualitatively different possibilities for the bulk geometry [52]: it could end at some $\rho$ with $a(\rho) > 0$; this is referred to as a 'gapped' phase, as it has the structure expected for a FT with an IR cutoff on de Sitter. Alternatively, the geometry could continue to a horizon, where $a(\rho) = 0$. This is referred to as an 'ungapped' phase. The pure AdS solution (4.2.6) is an example of an ungapped phase, but while pure AdS is smooth, generically for an ungapped phase we will have an FRW geometry beyond the horizon,

$$ds^2 = \ell^2 \left( -d\tau^2 + \frac{a^2(\tau)}{\eta^2} \left( d\eta^2 + d\vec{x}^2 \right) \right), \tag{4.2.9}$$

with $a(\tau)$ rising from zero at the horizon to some maximum value, and then returning to zero at a 'big crunch' singularity.

We will focus our analysis on some states where bulk geometries are known analytically, which are obtained by considering the field theory on de Sitter$_{d-1} \times S^1$. A geometry with this boundary can be obtained by double analytic continuation of the Schwarzschild-AdS black hole. This gives the 'bubble of nothing' spacetime [14, 7]

$$ds^2 = f(r)\, d\chi^2 + f(r)^{-1}\, dr^2 + \frac{r^2}{\eta^2}(-d\eta^2 + d\vec{x}^2), \tag{4.2.10}$$

with

$$f(r) = 1 + \frac{r^2}{\ell^2} - \frac{r_0^{d-2}}{r^{d-2}}. \tag{4.2.11}$$

If we do a Kaluza-Klein reduction over the $\chi$ circle, this provides an example of a geometry in the gapped phase. The reduced geometry is, however, singular, so it is simpler to analyse this case in the higher-dimensional geometry, where the geometry is smooth. The geometry ends at $r = r_+$, where $f(r_+) = 0$. The circle direction closes off smoothly at this radius if we identify $\chi$ with period

$$\Delta\chi = \frac{4\pi\ell^2 r_+}{r_+^2 d + \ell^2(d-2)}. \tag{4.2.12}$$

This coordinate system is valid at all $r \geq r_+$, so there is no horizon in the bulk. The quadratic relation between $\Delta\chi$ and $r_+$ implies that there is a maximum value of $\Delta\chi$ for which a bubble solution exists, $\Delta\chi_{\max} = 4\pi\ell/\sqrt{d(d-2)}$. For all smaller values of $\Delta\chi$, there are two bubble solutions, one with small $r_+$ and one with large $r_+$. The relationship between $r_0$ and $r_+$ is $r_0^{d-2} = r_+^{d-2}(1 + r_+^2/\ell^2)$.

An alternative geometry with the same asymptotics is obtained by setting $r_0 = 0$ in the above solution. This solution is simply AdS with a periodic identification (it is the analytic continuation of thermal AdS, where the time circle becomes the $\chi$ circle in our spacetime). This could be rewritten as

$$ds^2 = \cosh^2\rho d\chi^2 + \ell^2\left[d\rho^2 + \frac{\sinh^2\rho}{\eta^2}(-d\eta^2 + d\vec{x}^2)\right] \tag{4.2.13}$$

by setting $r = \ell \sinh\rho$. In this case we can choose the period of $\chi$ freely. The fact that the geometry is locally AdS$_{d+1}$ makes the analysis of this case particularly straightforward.

This is an example of an 'ungapped' phase, with a horizon in the bulk spacetime. There is a coordinate singularity at $r = \rho = 0$, but this is a horizon, and the geometry can be smoothly extended beyond it. This is clear if we consider the metric on surfaces of constant $\chi$: this is simply AdS in one lower dimension, in the de Sitter slicing (4.2.6). A good coordinate system which extends beyond this

horizon is thus obtained by passing to Poincaré coordinates on this lower-dimensional AdS space, making the coordinate transformation (4.2.7). The metric is then

$$ds^2 = \frac{t^2}{z^2}d\chi^2 + \frac{\ell^2}{z^2}(-dt^2 + dz^2 + d\vec{x}^2). \tag{4.2.14}$$

We see that the identification along $\chi$ becomes null at $t = 0$. As for a BTZ black hole, we cut off the spacetime at the 'singularity' where the circle identification becomes null, so the Penrose diagram for this spacetime is as shown in figure 4.1. In both solutions, it is the $\chi$ circle which is determining where we terminate the geometry, along a surface which would appear as a singularity from a dimensionally-reduced perspective.

The boundary stress tensor for these solutions was calculated by Balasubramanian and Ross [7] for $d = 4$. We work in a conformal frame where $\Delta\chi$ is the proper size of the $\chi$ circle, so the boundary metric is

$$ds_\partial^2 = d\chi^2 + \frac{\ell^2}{\eta^2}\left(-d\eta^2 + d\vec{x}^2\right). \tag{4.2.15}$$

The stress tensor is (recalling that we work in units where $16\pi G_N = 1$)

$$T^\chi_\chi = -\frac{3}{\ell^3}\left(r_0^2 + \ell^2/4\right), \quad T^\eta_\eta = T^{x_i}_{x_i} = \frac{1}{\ell^3}\left(r_0^2 + \ell^2/4\right). \tag{4.2.16}$$

The positive $T^\eta_\eta$ component corresponds to a negative energy density. For the values of $\Delta\chi$ where bubble solutions exist, we see that the bubbles have lower energy density than the locally AdS solution. The bubble with large $r_+$ is the lowest energy solution for a given $\Delta\chi$. This is analogous to the situation for a flat boundary with a circle direction, where the horizonless AdS soliton, to be seen in chapter 5, has a negative energy density, giving it lower energy than the identified Poincaré-AdS solution [38]. The difference in energy density between a bubble solution and the locally AdS solution is, for $d = 4$,

$$\Delta\rho = -\frac{r_0^2}{\ell^3} = -\frac{r_+^2\left(1 + r_+^2/\ell^2\right)}{\ell^3}. \tag{4.2.17}$$

We will compare the energy differences between these solutions to the complexity differences we calculate below. In the conformal frame adopted above, the energy of the state is simply

$$E = \frac{V_{\vec{x}}\,\Delta\chi\,\ell^{d-2}}{|\eta|^{d-2}}\rho. \tag{4.2.18}$$

It is then convenient to write the complexity as in (4.2.4), in terms of a complexity density $c$:

$$\mathcal{C} = \frac{V_{\vec{x}}\,\Delta\chi\,\ell^{d-2}}{|\eta|^{d-2}}c. \tag{4.2.19}$$

The first factor is the proper volume of a given slice of the boundary in the conformal frame above, and $c$ is the complexity density, which carries the state-dependent information, and is a constant independent of the boundary coordinates. The derivative with respect to proper time gives

$$\frac{d\mathcal{C}}{dt} = -\frac{\eta}{\ell}\frac{d\mathcal{C}}{d\eta} = (d-2)\frac{V_{\vec{x}}\,\Delta\chi\,\ell^{d-3}}{|\eta|^{d-2}}c, \tag{4.2.20}$$

so (1.3.2) becomes a relation between the complexity density and the energy density,

$$c \leq \frac{2\ell}{(d-2)\pi\hbar}\rho. \tag{4.2.21}$$

In the next sections, we test whether this bound can be satisfied and saturated in the different cases.

## 4.3 Holographic volume calculations

We now turn to the holographic calculation of the complexity for the spacetimes with de Sitter boundary introduced above. In this section, we calculate the complexity from the volume of the maximal spatial slice in the bulk, following the CV conjecture.

For the case of pure $\mathrm{AdS}_d$, we can use the coordinate transformation (4.2.7) to identify the slice of a cutoff boundary at some de Sitter time with a slice in Poincaré coordinates at fixed time, so the maximal volume surface is simply the constant-time surface in Poincaré coordinates. We take a boundary slice at $\eta = -\eta_0$ (so $\eta_0 > 0$) and $\rho = \rho_0$ in the flat de Sitter coordinates. This corresponds to $t = -t_0 = -\eta_0 \coth\rho_0$ and $z_0 = \eta_0/\sinh\rho_0$ in Poincaré coordinates. The maximal volume slice is the surface of constant $t$ (this surface is described by $\eta = -\eta_0 \tanh\rho/\tanh\rho_0$ in the de Sitter coordinates), whose volume is

$$V = \int_{t=t_0}\sqrt{h}\,dz\,d\vec{x} = \ell^{d-1}V_{\vec{x}}\int_{z_0}^{\infty}\frac{dz}{z^{d-1}} = \frac{\ell^{d-1}V_{\vec{x}}}{(d-2)z_0^{d-2}} = \ell\frac{V_{\vec{x}}}{(d-2)(H\eta_0)^{d-2}}, \tag{4.3.1}$$

where $H^{-1} = \ell\sinh\rho_0$ is the scale of the de Sitter space at the UV cutoff. This exhibits the expected UV divergence of the complexity.

Turning to theories where the conformal symmetry is broken, we consider the explicit examples of asymptotically locally $\mathrm{AdS}_{d+1}$ spaces with de $\mathrm{Sitter}_{d-1} \times S^1$ boundaries. The simpler case is the ungapped solution, as the bulk is locally AdS. We want to consider the maximal volume slice with boundary at $\eta = -\eta_0$ at large $\rho$ in the metric (4.2.13). This coordinate system does not cover the whole maximal volume slice; it will enter the region inside the 'horizon' at $\rho = 0$. Therefore to analyse this we use the coordinate transformation (4.2.7) to pass to the Poincaré

coordinates on the slices of constant $\chi$, so

$$ds^2 = \frac{t^2}{z^2}\, d\chi^2 + \frac{\ell^2}{z^2}(dz^2 - dt^2 + d\vec{x}^2). \tag{4.3.2}$$

We are looking for a maximal volume surface ending at $t = t_0 = -\eta_0$ as $z \to 0$. This will now not lie at fixed $t$. Let us take $t = t(z)$. Then

$$V = \ell^{d-1} \Delta\chi\, V_{\vec{x}} \int_{z_0}^{\infty} dz\, \frac{|t|\,\sqrt{1-\dot{t}^2}}{z^d}, \tag{4.3.3}$$

where again $z_0 = \eta_0/\sinh\rho_0$. Let us redefine the variables in this integration by $z = \eta_0 \bar{z}$, $t = \eta_0 \bar{t}(\bar{z})$. Then

$$V = \frac{\ell^{d-1}\Delta\chi\, V_{\vec{x}}}{\eta_0^{d-2}} \int_{\bar{z}_0}^{\infty} d\bar{z}\, \frac{|\bar{t}|\,\sqrt{1-\dot{\bar{t}}^2}}{\bar{z}^d}. \tag{4.3.4}$$

We see the time dependence required by the general symmetry argument. The remaining integral factor is a function only of the UV cutoff scale. In particular it will also be independent of the scale $\Delta\chi$, which enters here just as an overall multiplicative factor. Thus the complexity density in this case,

$$c = \frac{8(d-1)}{\pi} \int_{\bar{z}_0}^{\infty} d\bar{z}\, \frac{|\bar{t}|\,\sqrt{1-\dot{\bar{t}}^2}}{\bar{z}^d}, \tag{4.3.5}$$

is a pure numerical factor, depending only on the UV cutoff $\bar{z}_0 = 1/\sinh\rho_0$. Unlike the pure AdS case, however, this will have a finite contribution in addition to the UV divergent part.

We can solve the equations of motion arising from (4.3.5) with appropriate boundary conditions. We want $\bar{t} \to -1$ as $\bar{z} \to 0$. The minimal surface will approach this as $\bar{t} = -1 - \frac{1}{2(d-1)}\bar{z}^2 + \mathcal{O}(\bar{z}^4)$. There is a maximal volume slice behind the horizon; in the FRW patch coordinates,

$$ds^2 = \ell^2 \left( \cos^2\rho\, d\chi^2 - d\rho^2 + \frac{\sin^2\rho}{\eta^2}(d\eta^2 + d\vec{x}^2) \right), \tag{4.3.6}$$

this is at $\cos\rho_* = 1/\sqrt{d}$. This corresponds to $t = -z/\sqrt{d}$ in the Poincaré coordinates. Requiring that the slice approaches this surface at large $z$, we find numerically that for $d = 4$

$$c = \frac{24}{\pi}\left[ \frac{1}{3z_0^3} + \frac{1}{9z_0} - 0.03384 \right]. \tag{4.3.7}$$

The divergent terms are determined in terms of the boundary geometry by the calculations of Carmi et al. [20].

It is interesting to note that in more general ungapped geometries, there is non-trivial time dependence encoded in the scale factor $a(\tau)$ in the FRW region beyond

the horizon, but the complexity calculation is not hugely sensitive to this; as in this example, the maximal volume slice approaches a limiting surface where the scale factor is maximised, and the behaviour of the complexity will be mainly determined by this maximal value of the scale factor, and not its full time dependence.

Let us now consider the bubble of nothing, which provides an example of a gapped geometry. The metric is

$$ds^2 = f(r)\,d\chi^2 + \frac{dr^2}{f(r)} + \frac{r^2}{\eta^2}\left(-d\eta^2 + d\vec{x}^2\right). \tag{4.3.8}$$

We can describe the bulk maximal volume surface by $\eta = \eta_0 e^{s(r)}$ for some function $s(r)$, with $s(r) \to 0$ as $r \to \infty$. This surface closes off at $r = r_+$ where the $S^1$ shrinks to zero size. The induced metric on the surface is

$$ds^2 = f(r)\,d\chi^2 + \frac{dr^2}{f(r)}\left(1 - r^2 f(r) s'^2\right) + \frac{r^2}{\eta_0^2} e^{-2s}\,d\vec{x}^2. \tag{4.3.9}$$

To analyse smoothness at $r = r_+$, it is convenient to introduce a radial coordinate $\bar{r}$ with

$$\bar{r} = \int_{r_+}^{r} \frac{dr}{r\sqrt{f}}; \tag{4.3.10}$$

then the induced metric is

$$ds^2 = f(r)\,d\chi^2 + r^2\,d\bar{r}^2\left(1 - \left(\frac{ds}{d\bar{r}}\right)^2\right) + \frac{r^2}{\eta_0^2} e^{-2s}\,d\vec{x}^2, \tag{4.3.11}$$

and this will be smooth at $r = r_+$ for a suitable choice of period of $\chi$ if

$$\frac{ds(r_+)}{d\bar{r}} = 0. \tag{4.3.12}$$

The volume of this surface is

$$\begin{aligned} V &= \Delta\chi\, V_{\vec{x}} \int_{r_+}^{r_{\max}} dr \sqrt{1 - f(r)\frac{r^2}{\eta^2}\eta'^2}\left(\frac{r}{\eta}\right)^{d-2} \\ &= \frac{\Delta\chi\, V_{\vec{x}}}{\eta_0^{d-2}} \int_{r_+}^{r_{\max}} dr\, r^{d-2}\sqrt{1 - f(r) r^2 s'^2}\, e^{-(d-2)s} \\ &= \frac{\Delta\chi\, V_{\vec{x}}}{\eta_0^{d-2}} \int d\bar{r}\, r^{d-1}\sqrt{f}\sqrt{1 - \left(\frac{ds}{d\bar{r}}\right)^2}\, e^{-(d-2)s}, \end{aligned} \tag{4.3.13}$$

showing again that we get the time dependence required by symmetry. The integral is independent of $\eta_0$, but will now depend on $\Delta\chi$ through the dependence on $r_+$ in

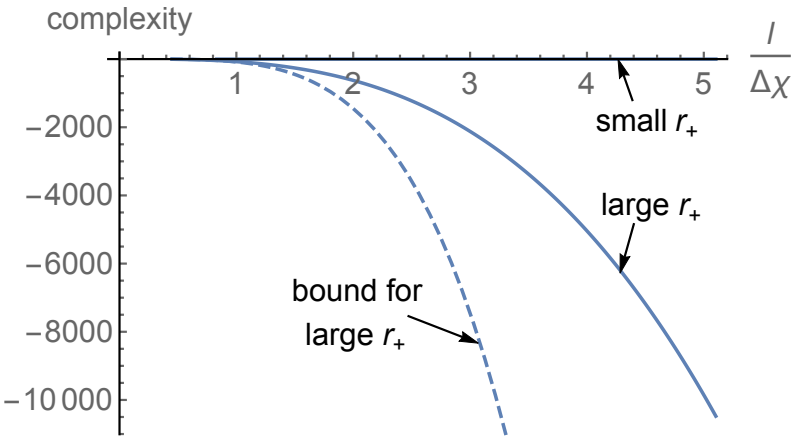


Figure 4.2: The difference in complexity between the two bubble of nothing solutions and the ungapped locally AdS solution, for $d = 4$. We plot the complexity density $c$ as a function of $\ell/\Delta\chi$ (working with the inverse period makes the graph clearer). The upper branch is the small $r_+$ solutions, and the lower is the large $r_+$ solution. The dashed curve at the bottom is the bound on the difference in complexity from the difference in energy for the large $r_+$ solution.

$f(r)$. Thus, the complexity density

$$c = \frac{8(d-1)}{\pi} \int d\bar{r} \left(\frac{r}{\ell}\right)^{d-1} \sqrt{f} \sqrt{1 - \left(\frac{ds}{d\bar{r}}\right)^2}\, e^{-(d-2)s} \tag{4.3.14}$$

is a function of $r_+$, and the result for the two bubbles for a given $\Delta\chi$ will be different. The UV divergent contributions are identical to the ungapped case; the $r_+$ dependence enters only in the finite term. Thus, the difference in complexity between different solutions with the same boundary is finite.

We can formulate the problem of extremising the integral in (4.3.13) by writing it as a first-order system, in terms of $s(r)$ and $q(r) = \frac{ds}{d\bar{r}}$. The system to solve is then

$$\begin{aligned} \frac{ds}{dr} &= \frac{q}{r\sqrt{f}} \\ \frac{dq}{dr} &= \left[\frac{d-2}{r\sqrt{f}} - q\left(\frac{d-1}{r} + \frac{1}{2}\frac{f'}{f}\right)\right](1-q^2) \end{aligned} \tag{4.3.15}$$

with the boundary conditions $q(r_+) = 0$, $s \to 0$ as $r \to \infty$.

We plot numerical results for the two families of bubble solutions as a function of $1/\Delta\chi$ in figure 4.2. We see that the solution with larger $r_+$ has a smaller volume slice for a given value of $\Delta\chi$, since the surface of the bubble lies closer to the boundary. This leads to a smaller complexity, so lowering the energy of the state has lowered the complexity growth rate, as we would expect. The difference in complexity is, however, smaller than that expected from the difference in energy. The solid curve in figure

4.2 plots the difference in the calculated complexity between the ungapped solution and the large $r_+$ bubble, while the dashed curve gives what would be expected if the bound, (4.2.21), were satisfied for both solutions. We see that the difference in complexity is smaller; hence if we assumed that the bubble solution satisfies the bound, the ungapped solution cannot saturate it. That is, the ungapped solution does not increase the complexity as fast as possible, given the energy difference from the large $r_+$ bubble, despite the presence of a horizon in the bulk.

This can be confirmed with an analytic argument. At large $r_+$, the function $f(r)$ is approximately

$$f(r) \approx \frac{r^2}{\ell^2} - \frac{r_+^d}{\ell^2 r^{d-2}} = \frac{r_+^2}{\ell^2}\tilde{r}^2\left(1 - \frac{1}{\tilde{r}^d}\right), \tag{4.3.16}$$

where we have set $r = r_+\tilde{r}$ in the second step to make the scaling clear. If we also define $s = \tilde{s}/r_+$, the volume integral becomes

$$V = \frac{\Delta\chi\, V_{\vec{x}}}{\eta_0^{d-2}} r_+^{d-1} \int_1^{\tilde{r}_{\max}} d\tilde{r}\, \tilde{r}^{d-2} \left[1 - \tilde{r}^4\left(1 - \frac{1}{\tilde{r}^d}\right)\left(\frac{d\tilde{s}}{d\tilde{r}}\right)^2\right]^{1/2} e^{-(d-2)\tilde{s}/r_+}, \tag{4.3.17}$$

where $\tilde{r}_{\max} = r_{\max}/r_+$. For large $r_+$, the exponential factor in the integral can be ignored. The function $\tilde{s}$ determined by extremising the integral then has no direct dependence on $r_+$. So dependence on $r_+$ enters only through the overall factor of $r_+^{d-1}$ and the cutoff $\tilde{r}_{\max} = r_{\max}/r_+$. The integral will have a UV divergence proportional to $\tilde{r}_{\max}^{d-1}$, which together with the $r_+^{d-1}$ prefactor gives the same $r_{\max}^{d-1}$ factor as before, so the UV divergent terms are independent of $r_+$, as they should be. The subleading divergences are absent in this approximation as our approximation for $f(r)$ neglects the curvature of the boundary. The finite contribution to the integral is independent of $r_+$, so the finite part of the volume will go as $r_+^{d-1}$ in this limit.

Thus, the difference in complexity between the ungapped solution and the large bubble will scale as $r_+^{d-1}$. This grows more slowly with $r_+$ than the difference in energy, which goes as $r_+^d$, confirming the numerical results shown in figure 4.2, and extending them to general $d$. A possible heuristic explanation of this behaviour of the complexity is that in a gapped theory, there is no structure on scales larger than $1/r_+$, so increasing $r_+$ is reducing the complexity by cutting out contributions at this scale, producing a reduction that scales like the volume in units of $1/r_+$. It would be interesting to understand the difference from the black hole case in more detail.

The volume of the slice in the bubble of small $r_+$ approaches a constant value for small $r_+$, that is, in the limit as $\Delta\chi \to \infty$. This is shown in figure 4.3. However, there is a small finite difference between it and the ungapped solution in this limit, even though the difference in energy goes to zero. Geometrically this is unsurprising; the ungapped solution has an additional region of spacetime behind the horizon, so it is not surprising that the volume of the slice is larger. This is also consistent with

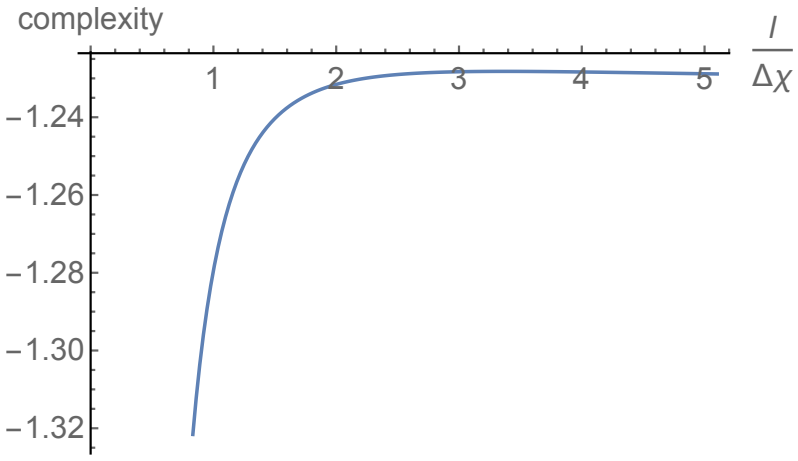


Figure 4.3: The difference in complexity between the bubble of nothing solution with small $r_+$ and the ungapped locally AdS solution, for $d = 4$. We plot the complexity density $c$, as a function of $\ell/\Delta\chi$. This is the same data as in figure 4.2, but plotted without the large $r_+$ data to zoom in on the difference in this case. We see that the difference does not approach zero for small $r_+$ (as we move to the right on the graph).

expectations from the black hole examples, that geometries with horizons will have more complexity for a given energy than those without.

## 4.4 Holographic action calculations

We now turn to the calculation of the complexity using the CA conjecture, calculating the action of the Wheeler-DeWitt patch for these examples. Unlike in the black hole cases, where the action calculation agreed with the volume calculation up to coefficients, the action calculation for these examples gives qualitatively different results to the volume calculation. We will find that the action of the bubble solutions increases at large $r_+$, where the volume decreased, and exhibits a logarithmic divergence at small $r_+$.

If we consider first pure AdS in de Sitter coordinates, the boundary slice at $\rho = \rho_0$, $\eta = \eta_0$ corresponds to $t = t_0 = -\eta_0 \coth \rho_0$ and $z_0 = \eta_0 / \sinh \rho_0$ in Poincaré coordinates, and the Wheeler-DeWitt patch and the calculation of the action are just as in chapter 3. The total action is as given in (3.2.13), i.e.[1]

$$S = 4\frac{\ell^{d-2}}{\epsilon^{d-2}} V_{\vec{x}} \ln(d-2) = 4\ln(d-2)\frac{V_{\vec{x}}}{(H\eta_0)^{d-2}}, \tag{4.4.1}$$

where, as before, $H^{-1} = \ell \sinh \rho_0$ is the scale of the de Sitter space at the UV cutoff.

[1]The difference in the power here is because previously we were discussing $\mathrm{AdS}_{d+1}$, whereas here we have chosen to consider $\mathrm{dS}_{d-1}$ slices in $\mathrm{AdS}_d$.

This has the same form as (4.3.1), up to the overall coefficient.

Let us turn now to the solutions with de Sitter$_{d-1} \times S^1$ boundaries. As before, the simpler case is the ungapped solution, which is locally AdS$_{d+1}$. To calculate the action of the Wheeler-DeWitt patch, it is again convenient to use the Poincaré coordinates, where the metric is

$$ds^2 = \frac{t^2}{z^2} d\chi^2 + \frac{\ell^2}{z^2}(dz^2 - dt^2 + d\vec{x}^2). \tag{4.4.2}$$

We want the action of the Wheeler-DeWitt patch for the boundary slice at $\rho = \rho_0$, $\eta = -\eta_0$, which corresponds to $t = -t_0 = -\eta_0 \coth \rho_0$ and $z_0 = \eta_0 / \sinh \rho_0$. Near the boundary the Wheeler-DeWitt patch looks just like in the case of pure AdS in Poincaré coordinates, with null surfaces at $dz = \pm dt$, but it is also cut off at $t = 0$ as seen in the conformal diagram of figure 4.1 and in figure 4.4.

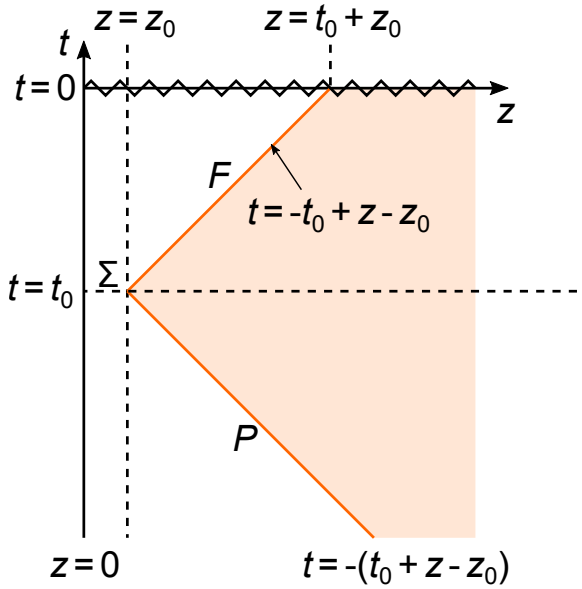


Figure 4.4: The Wheeler-DeWitt patch for the ungapped solution in Poincaré-like coordinates

The volume integral is

$$S_{\text{Vol}} = -2d\ell^{d-2} V_{\vec{x}}\, \Delta\chi \left( \int_{z_0}^{t_0+z_0} \frac{dz}{z^{d+1}} \int_{-(t_0+z-z_0)}^{-t_0+z-z_0} |t|\, dt + \int_{t_0+z_0}^{\infty} \frac{dz}{z^{d+1}} \int_{-(t_0+z-z_0)}^{0} |t|\, dt \right). \tag{4.4.3}$$

Taking the affine parametrization

$$\lambda = -\frac{\ell^2}{\alpha z} \text{ on } F, \qquad \lambda = \frac{\ell^2}{\beta z} \text{ on } P, \tag{4.4.4}$$

as before, we find the tangent vectors

$$k = \frac{\alpha z^2}{\ell^2}(\partial_t + \partial_z), \qquad \bar{k} = \frac{\beta z^2}{\ell^2}(\partial_t - \partial_z). \tag{4.4.5}$$

The corner contribution to the action is thus

$$S_\Sigma = -2\frac{\ell^{d-2}V_{\vec{x}}\,\Delta\chi\,t_0}{z_0^{d-1}}\ln(\alpha\beta z_0^2/\ell^2). \tag{4.4.6}$$

There is a contribution from the spacelike surface along $t=0$, from $z=t_0+z_0$ to $z=\infty$,

$$S_{\rm sing} = -2\int_{t_0+z_0}^{\infty} dz\,\sqrt{h}K = 2\ell^{d-2}V_{\vec{x}}\,\Delta\chi\int_{z_0+t_0}^{\infty}\frac{dz}{z^{d-1}}. \tag{4.4.7}$$

Along the null boundaries, we include the additional contribution (1.3.5), setting $c=\ell$ as before. The metric on $F$ has

$$\sqrt{\gamma} = \frac{\ell^{d-2}}{z^{d-1}}\,|t| = \frac{\ell^{d-2}}{z^{d-1}}(t_0-(z-z_0)), \tag{4.4.8}$$

so the expansion is

$$\Theta_F = \frac{1}{\sqrt{\gamma}}\frac{\partial\sqrt{\gamma}}{\partial\lambda} = -\frac{1}{\sqrt{\gamma}}\alpha\frac{z^2}{\ell^2}\frac{\partial\sqrt{\gamma}}{\partial z} = \frac{1}{\sqrt{\gamma}}\alpha\frac{z^2}{\ell^2}\ell^{d-2}\left((d-1)\frac{t_0+z_0}{z^d}-(d-2)\frac{1}{z^{d-1}}\right), \tag{4.4.9}$$

and hence the surface term is

$$S_{\rm F} = 2\ell^{d-2}V_{\vec{x}}\,\Delta\chi\int_{z_0}^{t_0+z_0}\left((d-1)\frac{t_0+z_0}{z^d}-(d-2)\frac{1}{z^{d-1}}\right)\ln(\ell\Theta_F)\,dz, \tag{4.4.10}$$

whereas on the past surface the expansion is

$$\Theta_P = \frac{1}{\sqrt{\gamma}}\alpha\frac{z^2}{\ell^2}\ell^{d-2}\left((d-1)\frac{t_0-z_0}{z^d}+(d-2)\frac{1}{z^{d-1}}\right), \tag{4.4.11}$$

and the integral runs to infinity, i.e.

$$S_{\rm P} = 2(d-2)\ell^{d-2}V_{\vec{x}}\,\Delta\chi\int_{z_0}^{\infty}\left((d-1)\frac{t_0-z_0}{z^d}+(d-2)\frac{1}{z^{d-1}}\right)\ln(\ell\Theta_P)\,dz. \tag{4.4.12}$$

Putting it all together, and setting $z_0=\eta_0/\sinh\rho_0$, $t_0=z_0\cosh\rho_0$, the action for the Wheeler-DeWitt patch is

$$S = 2\frac{V_{\vec{x}}\,\Delta\chi}{(H\eta_0)^{d-2}}\mathcal{I}(\rho_0), \tag{4.4.13}$$

where, as before, $H^{-1}=\ell\sinh\rho_0$, and the integral function $\mathcal{I}$ is

$$\begin{aligned}\mathcal{I} = \frac{1}{(d-2)(1+\cosh\rho_0)^{d-2}} &+ \int_1^{1+\cosh\rho_0}((d-1)(1+\cosh\rho_0)-(d-2)\bar{z})\ln(\theta_F)\frac{d\bar{z}}{\bar{z}^d}\\ &+\int_1^{\infty}((d-1)(\cosh\rho_0-1)+(d-2)\bar{z})\ln(\theta_P)\frac{d\bar{z}}{\bar{z}^d}.\end{aligned} \tag{4.4.14}$$

Here we have introduced new coordinates $\bar{t} = t/z_0$ and $\bar{z} = z/z_0$, and

$$\begin{aligned} \theta_F &= \bar{z}\frac{(d-1)(\cosh\rho_0+1)-(d-2)\bar{z}}{\cosh\rho_0+1-\bar{z}}, \\ \theta_P &= \bar{z}\frac{(d-1)(\cosh\rho_0-1)+(d-2)\bar{z}}{\cosh\rho_0-1+\bar{z}}. \end{aligned} \tag{4.4.15}$$

We see that, as for the volume calculation, the time dependence is as determined by the symmetry, and the period $\Delta\chi$ appears only as an overall factor.

The complexity density is

$$c = \frac{2}{\pi}\sinh^{d-2}\rho_0\,\mathcal{I}(\rho_0), \tag{4.4.16}$$

depending only on the UV cutoff as in the volume calculation (4.3.7). For $d = 3$,

$$\mathcal{I} = 2\ln 2\cosh\rho_0 + \frac{1+2\ln(2\cosh\rho_0)}{4\cosh\rho_0} + \mathcal{O}\left(\cosh^{-2}\rho_0\right). \tag{4.4.17}$$

For $d = 4$,

$$\mathcal{I} = 2\ln 3\cosh\rho_0 + \frac{1}{3\cosh\rho_0} + \frac{3+\ln 16}{27\cosh^2\rho_0} + \mathcal{O}\left(\cosh^{-3}\rho_0\right). \tag{4.4.18}$$

It is interesting to note that for more general solutions with some arbitrary function $a(\rho)$, the complexity density in the action calculation will depend non-trivially on $a(\rho)$, and not just on the value at the limiting surface, as in the volume calculation. The action of the Wheeler-DeWitt patch is a more sensitive probe of the bulk geometry than the volume of the maximal slice.

Consider now the action of the Wheeler-DeWitt patch in the bubble of nothing solutions. The main complication is in the position of the null boundaries. In the bubble metric (4.2.10), if we take a slice of the boundary at $\eta = -\eta_0$, the null boundaries are given by

$$\ln|\eta_{F,P}/\eta_0| = \mp\int_r^{r_{\max}} \frac{dr'}{r'\sqrt{f(r')}}, \tag{4.4.19}$$

where along the future boundary, $|\eta_F| < \eta_0$, while along the past boundary, $|\eta_P| > \eta_0$, with $|\eta_{F,P}| \to \eta_0$ as $r \to r_{\max}$. The volume integral is

$$\begin{aligned} S_{\rm Vol} &= -\frac{2d\,V_{\vec{x}}\,\Delta\chi}{\ell^2}\int_{r_+}^{r_{\max}} r^{d-1}\,dr\int_{\eta_P}^{\eta_F}\frac{d\eta}{|\eta|^{d-1}} \\ &= -\frac{2d\,V_{\vec{x}}\,\Delta\chi}{\ell^2(d-2)}\int_{r_+}^{r_{\max}} r^{d-1}\,dr\,\left(|\eta_F|^{-(d-2)}-|\eta_P|^{-(d-2)}\right). \end{aligned} \tag{4.4.20}$$

If we write[2]

$$F(r) = \int_r^{r_{\max}} \frac{dr'}{r'\sqrt{f(r')}}, \tag{4.4.21}$$

we can write this as

$$S_{\rm Vol} = -\frac{4d\, V_{\vec{x}}\, \Delta\chi}{\ell^2(d-2)\eta_0^{d-2}} \int_{r_+}^{r_{\max}} r^{d-1} \sinh\left((d-2)F(r)\right)\, dr. \tag{4.4.22}$$

The tangent to the null surface is

$$k = \alpha\left(-\frac{\eta}{r^2}\,\partial_\eta - \frac{\sqrt{f(r)}}{r}\,\partial_r\right) \tag{4.4.23}$$

on $F$ and

$$\bar{k} = \beta\left(-\frac{\eta}{r^2}\,\partial_\eta + \frac{\sqrt{f(r)}}{r}\,\partial_r\right) \tag{4.4.24}$$

on $P$. As before, $\alpha$, $\beta$ are some arbitrary positive constants. Note that $\eta < 0$, so the first terms are positive: these are future-pointing tangent vectors. The corner term in the action is then

$$S_\Sigma = -2V_{\vec{x}}\,\Delta\chi\sqrt{f(r_{\max})}\frac{r_{\max}^{d-2}}{\eta_0^{d-2}}\ln\left(\frac{\alpha\beta}{r_{\max}^2}\right). \tag{4.4.25}$$

The expansions are

$$\Theta_F = -\alpha\frac{\sqrt{f(r)}}{r}\frac{1}{\sqrt{\gamma}}\frac{\partial\sqrt{\gamma}}{\partial r} = -\alpha\frac{\sqrt{f(r)}}{r}\left(\frac{f'(r)}{2f(r)} + \frac{d-2}{r} - \frac{d-2}{r\sqrt{f(r)}}\right), \tag{4.4.26}$$

$$\Theta_P = \beta\frac{\sqrt{f(r)}}{r}\frac{1}{\sqrt{\gamma}}\frac{\partial\sqrt{\gamma}}{\partial r} = \beta\frac{\sqrt{f(r)}}{r}\left(\frac{f'(r)}{2f(r)} + \frac{d-2}{r} + \frac{d-2}{r\sqrt{f(r)}}\right), \tag{4.4.27}$$

so the surface integrals are

$$S_F = \frac{2V_{\vec{x}}\,\Delta\chi}{\eta_0^{d-2}}\int_{r_+}^{r_{\max}} \sqrt{f(r)}r^{d-2}e^{(d-2)F(r)}\left(\frac{f'(r)}{2f(r)} + \frac{d-2}{r} - \frac{d-2}{r\sqrt{f(r)}}\right)\ln|\ell\Theta_F|\, dr \tag{4.4.28}$$

and

$$S_P = \frac{2V_{\vec{x}}\,\Delta\chi}{\eta_0^{d-2}}\int_{r_+}^{r_{\max}} \sqrt{f(r)}r^{d-2}e^{-(d-2)F(r)}\left(\frac{f'(r)}{2f(r)} + \frac{d-2}{r} - \frac{d-2}{r\sqrt{f(r)}}\right)\ln|\ell\Theta_P|\, dr \tag{4.4.29}$$

[2]For $d = 4$, this can be written in terms of an elliptic integral,

$$F(r) = \frac{\ell}{r_+}F\left(i\sinh^{-1}\left(r/\sqrt{\ell^2 + r_+^2}\right)\middle|-1 - \frac{\ell^2}{r_+^2}\right).$$

So the total integral is

$$S = \frac{2V_{\vec{x}}\,\Delta\chi}{\eta_0^{d-2}}\Bigg[-\frac{2d}{\ell^2(d-2)}\int_{r_+}^{r_{\max}} r^{d-1}\sinh\left((d-2)F(r)\right)dr \\ - \sqrt{f(r_{\max})}r_{\max}^{d-2}\ln\left(\frac{\alpha\beta}{r_{\max}^2}\right) \\ + \int_{r_+}^{r_{\max}}\sqrt{f(r)}r^{d-2}e^{(d-2)F(r)}\left(\frac{f'(r)}{2f(r)}+\frac{d-2}{r}-\frac{d-2}{r\sqrt{f(r)}}\right)\ln|\ell\Theta_F|\,dr \\ + \int_{r_+}^{r_{\max}}\sqrt{f(r)}r^{d-2}e^{-(d-2)F(r)}\left(\frac{f'(r)}{2f(r)}+\frac{d-2}{r}-\frac{d-2}{r\sqrt{f(r)}}\right)\ln|\ell\Theta_P|\,dr\Bigg]. \tag{4.4.30}$$

The complexity density is

$$c = \frac{2}{\pi}\Bigg[-\frac{2d}{(d-2)}\int_{r_+}^{r_{\max}}\left(\frac{r}{\ell}\right)^{d-1}\sinh\left((d-2)F(r)\right)\frac{dr}{\ell} \\ - \sqrt{f(r_{\max})}\left(\frac{r_{\max}}{\ell}\right)^{d-2}\ln\left(\frac{\alpha\beta}{r_{\max}^2}\right) \\ + \int_{r_+}^{r_{\max}}\sqrt{f(r)}\left(\frac{r}{\ell}\right)^{d-2}e^{(d-2)F(r)}\left(\frac{f'(r)}{2f(r)}+\frac{d-2}{r}-\frac{d-2}{r\sqrt{f(r)}}\right)\ln|\ell\Theta_F|\,dr \\ + \int_{r_+}^{r_{\max}}\sqrt{f(r)}\left(\frac{r}{\ell}\right)^{d-2}e^{-(d-2)F(r)}\left(\frac{f'(r)}{2f(r)}+\frac{d-2}{r}-\frac{d-2}{r\sqrt{f(r)}}\right)\ln|\ell\Theta_P|\,dr\Bigg]. \tag{4.4.31}$$

As in the CV case, we want to compare the difference in complexity between the two bubble solutions and the ungapped solution to the difference in energy. The action is calculated numerically and plotted in figure 4.5, as a function of $r_+$. We see that the action *increases* relative to the ungapped solution, for both large and small bubbles. For large bubbles, the increase comes basically from the negative volume contribution; the smaller spacetime volume makes the negative contribution from (4.4.20) less significant, increasing the action. The surface contributions (4.4.28), (4.4.29) are numerically less important. Numerically, the bubble solutions always have a larger complexity than the ungapped solution. This is a surprising result; these solutions have lower energy, but larger complexity. For small bubbles, the increase comes from the additional surface terms we added on the null boundaries.

As in the volume calculation, we can obtain the scaling for large $r_+$ from an analytic argument. Taking the approximation for $f(r)$ in (4.3.16), we have $F(r) \approx \tilde{F}(\tilde{r})/r_+$, where

$$\tilde{F}(\tilde{r}) = \int_{\tilde{r}}^{\tilde{r}_{\max}}\frac{dr'}{r'^2\sqrt{1-r'^{-d}}}. \tag{4.4.32}$$

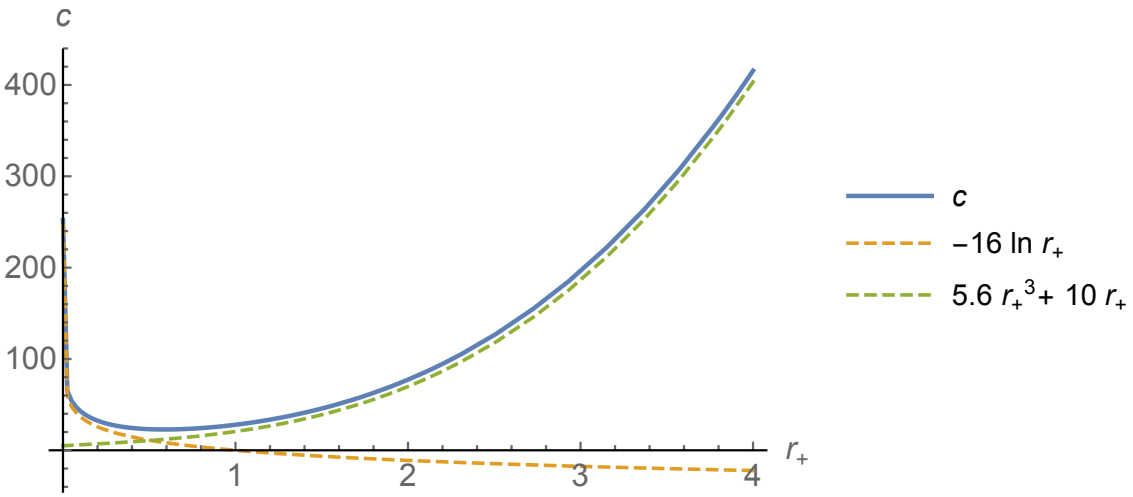


Figure 4.5: The complexity density of the gapped solutions relative to the ungapped solution, plotted as a function of $r_+/\ell$, for $d = 4$. The dotted curves indicate the asymptotics expected from the analytic discussion, with a fit to a function of the form $-a \ln r_+$ for small $r_+$ and $br_+^3 + cr_+$ for large $r_+$. We see that the action of the bubbles is always greater than the ungapped solution, and increases for both large and small bubbles at small $\Delta\chi$.

The volume integral is

$$S_{\rm Vol} = r_+^{d-1} \int_1^{\tilde{r}_{\rm max}} \tilde{r}^{d-1}(d-2)\tilde{F}(\tilde{r})\, d\tilde{r} \sim r_+^{d-1}(\tilde{r}_{\rm max}^{d-1}+\text{finite}) \sim r_{\rm max}^{d-1}+\mathcal{O}(r_+^{d-1}), \quad (4.4.33)$$

so the finite term is of order $r_+^{d-1}$. The corner term never makes a finite contribution. The contributions from $S_F$ and $S_P$ are a little more subtle; the expansions $\Theta_{F,P} \sim 1/r_+$, so in an expansion in $r_+$, $S_{F,P}$ have terms of order $r_+^{d-1} \ln r_+$, but these are total derivatives:

$$\begin{aligned} S_{F,P} &= r_+^{d-1} \ln r_+ \int \Theta_{F,P} \sqrt{\gamma}\, d\lambda\, d^{d-2}x + \mathcal{O}(r_+^{d-1}) \\ &= r_+^{d-1} \ln r_+ \int \partial_\lambda \sqrt{\gamma}\, d\lambda\, d^{d-2}x + \mathcal{O}(r_+^{d-1}) \\ &= r_{\rm max}^{d-1} \ln r_+ + \mathcal{O}(r_+^{d-1}). \end{aligned} \quad (4.4.34)$$

Crucially, there is no finite term in evaluating the total derivative integral, as $\sqrt{\gamma} = 0$ on the bubble. The divergent term combines with a $r_{\rm max}^{d-1} \ln \tilde{r}_{\rm max}$ divergence from the $r_+^{d-1}$ contribution to give the expected $r_{\rm max}^{d-1} \ln r_{\rm max}$ divergences in these integrals. So we have the leading UV divergences, which we know are independent of $r_+$ in general, and a finite term which comes just from the $r_+^{d-1}$ part. Thus the contributions from these surface integrals go as

$$S_{F,P} \sim r_{\rm max}^{d-1} \ln r_{\rm max} + r_{\rm max}^{d-1} + \mathcal{O}(r_+^{d-1}). \quad (4.4.35)$$

The finite contributions to the action at large $r_+$ will scale like $r_+^{d-1}$, just as in the volume calculation.

The crucial difference which we learn from the numerical analysis is that the sign is different. While in the volume calculation the finite contribution was reducing the volume as $r_+$ increased, here it is increasing the action. We can't fix this sign from the analytic scaling argument; it comes from the numerics.

We can also use a similar argument to show that the action of the small bubbles has a divergence at small $r_+$. To carefully analyse the integration in the limit of small $r_+$, we will use two different approximations to $f(r)$: for $r \ll \ell$, we can write

$$f(r) \approx 1 - \frac{r_+^{d-2}}{r^{d-2}} = 1 - \frac{1}{\tilde{r}^{d-2}}, \tag{4.4.36}$$

where we again introduce a rescaled coordinate $r = r_+\tilde{r}$, while for $r \gg r_+$, we can approximate

$$f(r) \approx 1 + \frac{r^2}{\ell^2}. \tag{4.4.37}$$

For small $r_+$, these two approximations have an overlapping region of validity. In calculating the action, we can therefore divide the integration over $r$ into two regions, $r_+ \leq r < a$, and $a \leq r \leq r_{\max}$, for some $a$ such that $r_+ \ll a \ll \ell$, and we use the first approximation in the small $r$ regime and the second in the large $r$ regime. The overlap of the two approximations implies that the result will be independent of the particular value of $a$ where we choose to make the division. At the end of the calculation we want to take $r_+ \to 0$ at fixed, large $a/r_+$. The leading contribution from the second regime will be independent of $r_+$, so it is the contribution from the first regime that concerns us.

For $r$ in the first region, $r_+ \leq r < a$, the approximation for $f(r)$ implies

$$F(r) \approx \int_{\tilde{r}}^{a/r_+} \frac{d\tilde{r}'}{\tilde{r}'\sqrt{1 - 1/\tilde{r}'^{d-2}}} + \int_a^{r_{\max}} \frac{dr'}{r'\sqrt{1 + r'^2/\ell^2}} = -\ln r_+ + \tilde{F}(\tilde{r}), \tag{4.4.38}$$

where $\tilde{F}$ is finite as $r_+ \to 0$. Thus the volume integral from the first region is

$$S_{\text{Vol}} \propto \int_{r_+}^{a} r^{d-1} \sinh\left((d-2)F(r)\right) dr \approx r_+^2 \int_1^{a/r_+} \tilde{r}^{d-1} e^{(d-2)\tilde{F}(\tilde{r})}\, d\tilde{r}, \tag{4.4.39}$$

so the contribution from this integral vanishes as $r_+, a \to 0$. The expansions in this region are

$$\Theta_{F,P} = \frac{\tilde{\theta}_{F,P}}{r_+^2}, \tag{4.4.40}$$

where $\tilde{\theta}_{F,P}$ is finite as $r_+ \to 0$. In the integral on the past surface, the exponential

in $F(r)$ makes the integrand small, so the contribution from the first region is finite:

$$S_P \propto \int_{r_+}^{a} r^{d-1} e^{-(d-2)F(r)} \Theta_P \ln|\ell\Theta_P|\, dr = r_+^{2d-5} \int_1^{a/r_+} \tilde{r}^{d-1} e^{-(d-2)\tilde{F}(\tilde{r})} \tilde{\theta}_P \ln\left|\ell\tilde{\theta}_P/r_+^2\right| d\tilde{r}. \tag{4.4.41}$$

The overall factor of $r_+$ ensures that this has no divergent contributions. However, in the integral on the future surface, the exponential in $F(r)$ cancels factors of $r_+$, giving

$$S_F \propto \int_{r_+}^{a} r^{d-1} e^{(d-2)F(r)} \Theta_F \ln|\ell\Theta_F|\, dr = \int_1^{a/r_+} \tilde{r}^{d-1} e^{(d-2)\tilde{F}(\tilde{r})} \tilde{\theta}_F \ln\left|\ell\tilde{\theta}_F/r_+^2\right| d\tilde{r}. \tag{4.4.42}$$

There is a logarithmic divergence in $r_+$ here. The coefficient is a total derivative, as

$$\Theta_F = -\alpha \frac{\sqrt{f}}{r} \frac{1}{\sqrt{\gamma}} \partial_r \sqrt{\gamma} = -\frac{1}{r^{d-1}\eta^{d-2}} \partial_r \sqrt{\gamma}, \tag{4.4.43}$$

so

$$\begin{aligned} S_F &\propto -2 \ln r_+ \int_{r_+}^{a} \partial_r \sqrt{\gamma}\, dr + \ldots \\ &= -2 \ln r_+ \sqrt{\gamma}(a) + \ldots \\ &= -2 \ln r_+ \frac{1}{\eta_0^{d-2}} + \ldots, \end{aligned} \tag{4.4.44}$$

where in the first step we used the vanishing of the volume in the $\chi$ direction at $r = r_+$, and in the second step it is useful to note that the determinant of $\gamma$ is approximately constant in the region $r_+ \ll r \ll \ell$, so the result is independent of the particular value of $a$ chosen. Thus, the complexity for small $r_+$ grows like $-\ln r_+$. This is confirmed by the numerical results, which show a growth at small $r_+$.

Thus, for small values of the period $\Delta\chi$, the CA calculation with our current prescription for the action gives that:

- For the ungapped solution, the complexity density is a constant, independent of $\Delta\chi$.
- For the small bubble, the complexity density has a finite contribution on top of the ungapped result which grows as $-\ln \Delta\chi$ at small $\Delta\chi$. In this regime the energy density for the small bubble approaches the same value as for the ungapped solution. This divergence comes from the additional term on the future null surface we added to restore reparametrization invariance and eliminate undesirable log divergences in the UV.
- For the large bubble, the complexity density has a finite contribution on top of the ungapped result which grows as $1/\Delta\chi^{d-1}$ at small $\Delta\chi$. The energy density for the large bubble is less than that of the ungapped solution by a

factor which grows as $1/\Delta\chi^d$. The action grows for larger bubbles because the volume integral makes a negative contribution to the action, and this dominates over the surface terms.

These results are unexpected, and qualitatively different from what we obtained in the CV calculation. This might lead us to question whether the calculation we are applying is correct. The action we have considered is the one constructed by Lehner et al. [46], with the additional surface term. This is the minimal action whose variation vanishes for arbitrary variations of the metric holding the intrinsic geometry of the boundary fixed, and which is reparametrization invariant. However, we are free to add boundary terms to the action which are functions only of the intrinsic geometry of the boundary, obtaining alternative actions whose variations also vanish. This includes reparametrization-invariant integrals along the null boundaries like the ones given in (1.3.5). If we add such a term along the null boundaries, it will only add a time-independent correction to the action in the Schwarzschild-AdS case, so it would not modify the success of Lehner et al. [46] in reproducing the expected behaviour (1.3.2). But it could modify the value of the $r_+$ dependent part in our calculation. The challenge is to find an appropriate well-motivated correction.

Note that although the ambiguity in the action we are considering here is the same one exploited in holographic renormalization, our case is different in that we are considering adding boundary terms on the boundary of the Wheeler-DeWitt patch, which extends into the interior of the spacetime. Thus, these modifications can affect the finite, state-dependent part of the action.

For our application to de Sitter in flat coordinates, the metric $\gamma_{ab}$ on the spatial slices of the null surface is flat, so it is challenging to find natural corrections which will change the answer. Integrals of the form (1.3.5) which involve the curvature of $\gamma$ will vanish in our case. If we take (1.3.5) with $f(\gamma)$ just a constant, this is a total derivative. We then have

$$S_N = f\int \Theta\sqrt{\gamma}\, d\lambda\, d\chi\, d^{d-2}x = f\int \partial_\lambda\sqrt{\gamma}\, d\lambda\, d\chi\, d^{d-2}x = f\int_\Sigma \sqrt{\gamma}\, d\chi\, d^{d-2}x, \quad (4.4.45)$$

so this term amounts to adding a counterterm at the corner. In the last step we used again the fact that the volume element on the $\chi$ circle vanishes at the bubble. Adding such counterterms at the corner does not change the finite part of the action. The only non-trivial structure on the null surface in our case is the expansion. We can construct new reparametrization-invariant integrands by considering non-polynomial combinations of the expansion and its derivative with respect to $\lambda$: for example, we could add a term like

$$S_N = \int \frac{\partial_\lambda\Theta}{\Theta}\sqrt{\gamma}\, d\lambda\, d\chi\, d^{d-2}x, \quad (4.4.46)$$

but such terms seem fairly contrived; it is difficult to see how such an action prescription would arise from a simple underlying principle. Thus, it appears challenging to give a satisfactory prescription for the action which would give results for the complexity that are qualitatively similar to those from the volume calculation in these bubble solutions.

## 4.5 Discussion

We have considered the holographic calculation of the complexity for a field theory on de Sitter space in a de Sitter-invariant state. The holographic dual can have different bulk solutions satisfying these boundary conditions, corresponding to different de Sitter-invariant states in the boundary field theory.

We find that the holographic complexity of these de Sitter-invariant states on a given spatial slice is a multiple of the proper volume of the slice. The de Sitter invariance fixes the multiplicative factor to be a state-dependent constant, independent of de Sitter time. Holographically, the states can have dual bulk solutions which have a horizon, corresponding to ungapped field theory states, or with no horizon, corresponding to gapped states. We have considered the particular case of field theory on de Sitter$_{d-1} \times S^1$, where explicit solutions of both kinds are known: the ungapped solution is locally AdS, and has a horizon in the bulk analogous to the one in the BTZ black hole. The gapped solutions are 'bubbles of nothing' obtained by double analytic continuation from Schwarzschild-AdS.

We found that in the CV calculation, the gapped solutions have lower complexity than the ungapped case, but the difference in complexity is smaller than the difference in energy, so the bound (1.3.2) on the growth of the complexity can be satisfied, but not saturated in both geometries. For the large bubbles, the difference in complexity scales as $r_+^{d-1}$, while the difference in energy scales as $r_+^d$. It would be interesting to understand why this bound is saturated for the field theory on flat space but not on these de Sitter spaces.

In the CA calculation, we found a surprising sign difference: the action *grows* for both larger bubbles (like $r_+^{d-1}$) and for smaller bubbles (like $-\ln r_+$), so the complexity of the bubbles is larger than that for the ungapped solution. This is not what we expected to find, and suggests that the prescription for the action we have used should be modified. The log divergence for smaller bubbles came from the new term which we argued in our previous work should be introduced to make the action reparametrization-independent. It could be cured by removing this term, although that would leave the problem of reparametrization-dependence and a different UV divergence in the action calculations compared to the volume calculations. The

growth of the action for large bubbles seems to come mainly from the volume term in the action. There is, in principle, freedom to modify the action prescription by adding boundary terms which depend just on the intrinsic geometry of the boundary of the Wheeler-DeWitt patch. But it is challenging to find natural modifications which will make a difference in our case. In the next chapter we will look at a simpler example that exhibits the same pathologies, with the aim of taking some initial steps in resolving the differences between the CV and CA results.

# Chapter 5

# Complexity of the AdS Soliton

Given the striking differences between the CV and CA calculations obtained for the 'bubble of nothing' solutions discussed in the previous chapter, it made sense to attempt to discover a simpler context in which similar discrepancies still exist. This chapter examines such a context. We consider field theory on a (flat) torus with antiperiodic boundary conditions for fermions on (at least) one cycle. The ground state for such boundary conditions is then dual to the AdS soliton [38], where the cycle with antiperiodic boundary conditions closes off smoothly in the bulk at a 'bubble', at a radius $r_+$ which is inversely proportional to the size of this cycle. In this chapter, we consider the CV and CA calculations of the complexity of this ground state. This is a simple adaptation of the calculations of the previous chapter — indeed, this geometry arises as a limit of the de Sitter geometries considered previously. Due to the flat (rather than de Sitter) boundary, we obtain a time-independent result in both cases. However, the result depends non-trivially on the size of the cycle with antiperiodic boundary conditions, through the dependence on the position of the 'bubble' in the bulk.

As in the previous chapter, we find striking differences between the CV and CA calculations. We will see that the straightforward CV calculation gives a smaller complexity for antiperiodic than for periodic boundary conditions (which correspond to plain AdS). The complexity for antiperiodic boundary conditions decreases monotonically as the circle radius decreases, bringing the bubble closer to the boundary. In contrast, the CA calculation results in larger complexity for the antiperiodic boundary conditions than for periodic, and this complexity initially increases with decreasing circle radius (while that radius is large compared with the UV cutoff scale). It eventually turns around and decreases, going to zero as the bubble approaches the boundary, as one would expect. While the complexity goes to zero in this limit in both CV and CA cases, we find that this involves different powers of the separation in the two cases.

The two proposals for holographic complexity thus give very different answers already in this simple context. It was therefore desirable to attempt to compare these holographic calculations with a more direct calculation of complexity in the boundary field theory. We extend the calculations of Jefferson and Myers [42] and Chapman et al. [21], who considered the free boson on a toroidal lattice, to the consideration of free fermions. This allows us to consider the change in complexity resulting from changing the fermion boundary conditions from periodic to antiperiodic. We find that in our simple lattice calculations, a larger result for complexity is found for antiperiodic boundary conditions than for periodic in (a limited) agreement with the CA calculation. It is worth emphasizing that the calculation we carry out has strong limitations and an important direction for future work is to refine the field theory calculation and see what effect this has on the behaviour we find.

We discuss the AdS soliton solution in section 5.1 and carry out the CV calculation, while the CA calculation is described in section 5.2. In section 5.3, we switch to working in the boundary theory, considering free fermions on a lattice and calculating the difference in complexity for the two boundary conditions on the fermions. Section 5.4 concludes this chapter with a brief summary of the results and a discussion of future directions.

## 5.1 The AdS soliton

If we consider a field theory defined on a flat torus, with periodic boundary conditions for the fermions (preserving supersymmetry), the holographic dual of the ground state is the pure AdS solution in Poincaré coordinates. Calculations of holographic complexity for this case were considered in chapter 3. If, however, we take antiperiodic boundary conditions for the fermions in one or more directions, then while the pure AdS solution is still a solution, it no longer corresponds to the ground state in the field theory. The holographic dual of the ground state is instead the AdS soliton [38],

$$ds^2 = \frac{r^2}{\ell^2}\left[-dt^2 + \left(1 - \frac{r_+^d}{r^d}\right) d\chi^2 + d\vec{x}^2\right] + \left(1 - \frac{r_+^d}{r^d}\right)^{-1} \frac{\ell^2}{r^2}\, dr^2, \tag{5.1.1}$$

where $\chi$ is the circle with antiperiodic boundary conditions (or if there is more than one such circle, the one with the smallest period). We take a $d$-dimensional boundary, so there are $d-2$ coordinates $\vec{x}$. Imposing smoothness at $r = r_+$ relates the parameter $r_+$ to the periodicity of $\chi$,

$$\Delta\chi = \frac{4\pi\ell^2}{r_+ d}. \tag{5.1.2}$$

This solution has a negative boundary energy,

$$E = -\frac{r_+^d \, \Delta\chi \, V_{\vec{x}}}{\ell^{d+1}} = -\frac{V_{\vec{x}} \ell^{d-1} (4\pi)^d}{d^d \, \Delta\chi^{d-1}}. \tag{5.1.3}$$

This can be understood as a Casimir energy for the ground state due to the periodicity of $\chi$. Because of the antiperiodic boundary conditions for the fermions, the Casimir energies of bosons and fermions fail to cancel.

Note that the dependence on $r_+$ can be converted into an overall scale by a change of coordinates: if we set

$$r = r_+ \tilde{r}, \qquad t = \frac{\tilde{t}}{r_+}, \qquad \chi = \frac{\tilde{\chi}}{r_+}, \qquad x^i = \frac{\tilde{x}^i}{r_+}, \tag{5.1.4}$$

the metric becomes

$$ds^2 = \frac{\tilde{r}^2}{\ell^2} \left[ -d\tilde{t}^2 + \left(1 - \frac{1}{\tilde{r}^d}\right) d\tilde{\chi}^2 + d\vec{\tilde{x}}^2 \right] + \left(1 - \frac{1}{\tilde{r}^d}\right)^{-1} \frac{\ell^2}{\tilde{r}^2} \, d\tilde{r}^2. \tag{5.1.5}$$

It is interesting to consider the complexity of the ground state for the field theory with these boundary conditions, and specifically its dependence on the size of the $\chi$ circle. For the CV conjecture, the maximum volume calculation is easily carried out. Because of the time-independence of the metric (5.1.1), the maximum volume slice will lie at constant $t$, so the volume is simply

$$V(B) = \int dr \, d^{d-2}x \, d\chi \, \sqrt{h} = V_{\vec{x}} \, \Delta\chi \int_{r_+}^{r_{\max}} dr \, \frac{r^{d-2}}{\ell^{d-2}} = \frac{V_{\vec{x}} \, \Delta\chi}{d-1} \frac{r_{\max}^{d-1} - r_+^{d-1}}{\ell^{d-2}}, \tag{5.1.6}$$

where we introduce a UV cutoff at $r = r_{\max}$. This gives us a complexity

$$\mathcal{C}_{\mathrm{V}} = \frac{8 V_{\vec{x}} \, \Delta\chi}{\pi} \frac{r_{\max}^{d-1} - r_+^{d-1}}{\ell^{d-1}}. \tag{5.1.7}$$

The first term is the same UV divergence we saw in the pure AdS solution in (3.2.3). If we take the difference, defining a 'complexity of formation' [22], we find a finite negative difference; changing the boundary conditions has lowered the complexity. Put another way, the pure AdS solution, which corresponds to some excited state with these boundary conditions, has higher complexity than the ground state. This seems a plausible result; adding excitations might be expected to generically increase the complexity of the state.

If we were to take $r_+ \to r_{\max}$, the complexity would go to zero. As this limit corresponds to the proper size of the $\chi$ circle at the UV cutoff scale vanishing, this seems physically reasonable. Note that the complexity vanishes linearly in $r_{\max} - r_+$ in this case.

## 5.2 Holographic action calculations

We now turn to the calculation of the complexity using the CA conjecture, calculating the action of the Wheeler-DeWitt patch for the AdS soliton. We will find that the action of the Wheeler-DeWitt patch initially increases with $r_+$, although it does ultimately go to zero as $r_+ \to r_{\max}$ as well.

The calculation of the action is quite similar to the calculation in the bubbles with de Sitter boundaries of the previous chapter, although somewhat simpler. Indeed, in the limit of large $r_+$, the Wheeler-DeWitt patch in those bubble solutions approaches the Wheeler-DeWitt patch in the AdS soliton.

The action will have an overall scaling as $r_+^{d-1}$, which is evident if we perform the calculation in the rescaled coordinates of (5.1.5). If the original coordinates have a UV cutoff at $r = r_{\max}$, then in the tilded coordinates $\tilde{r} \in (1, r_{\max}/r_+)$, so the result of the action integrals will be some function of $r_{\max}/r_+$, times the coordinate volume in the spatial directions

$$S = \tilde{V}_x \Delta\tilde{\chi} I(r_{\max}/r_+). \tag{5.2.1}$$

If we rewrite the spatial volume in terms of the original coordinates, we get an overall factor of $r_+^{d-1}$. Thus

$$S = V_{\vec{x}}\, \Delta\chi\, r_+^{d-1} I(r_{\max}/r_+). \tag{5.2.2}$$

If we take the UV cutoff large at fixed $r_+$, there will be a power series expansion in powers of $r_{\max}/r_+$. From the results of Carmi et al. [20], we know the divergent terms in this expansion will be determined by the local geometric invariants of the boundary. For the flat boundary we are considering, the only non-zero term is the leading divergence, proportional to the volume, which agrees with the result in the pure AdS case. Thus, in the large $r_{\max}$ limit, the action looks like

$$\begin{aligned} S &= 4V_{\vec{x}}\, \Delta\chi\, \ln(d-1) \frac{r_+^{d-1}}{\ell^{d-1}} \left[ \left( \frac{r_{\max}}{r_+} \right)^{d-1} + I_0 + \ldots \right] \\ &= \frac{4V_{\vec{x}}\, \Delta\chi}{\ell^{d-1}} \ln(d-1)(r_{\max}^{d-1} + I_0 r_+^{d-1} + \ldots), \end{aligned} \tag{5.2.3}$$

where the dots denote terms which vanish in the limit of large $r_{\max}$. Thus, as in the volume calculation above, there is a finite difference between the complexity with antiperiodic and periodic boundary conditions, determined by the numerical parameter $I_0$. We will calculate the action in detail to determine $I_0$; from our work in chapter 4, we expect it to be positive, in contrast to the CV calculation.

In our numerical calculation of the action, we choose to set $c = \ell/(d-1)$, rather than simply using $c = \ell$ as in the previous calculations. This is equivalent to using

$c = \ell$ but then adding a local integral over $\Sigma$,

$$S_{\rm ct} = -4\ln(d-1)\int_\Sigma \sqrt{h}\, dS = -\frac{4V_{\vec{x}}\,\Delta\chi}{\ell^{d-1}}\ln(d-1) r_{\rm max}^{d-1}\sqrt{1-\frac{r_+^d}{r_{\rm max}^d}}, \tag{5.2.4}$$

so that $S' = S + S_{\rm ct}$. In either case, the change has the effect of simplifying the calculation by cancelling the leading divergence; in plain AdS, the result of the complexity calculation becomes zero, while in the case of the AdS soliton, the new action has $I_0$ as its leading contribution at large $r_{\rm max}/r_+$. This change in the action is part of the remaining ambiguity unfixed by the prescription of Lehner et al. [46]. The interpretation of this kind of renormalization in terms of the complexity is unclear, but it is convenient for the numerics, and since the additional contribution to the action is a known function, one can remove it at the end of the calculation if desired. Note that the subleading contribution in $S_{\rm ct}$ is of order $r_+^d/r_{\rm max}$, so adding this term does not affect the finite contribution $I_0$.

We now turn to the details of the calculation of the action, which we will perform in the tilded coordinates with the metric (5.1.5). We will also drop the tildes to reduce clutter, with the exception that $V_{\vec{x}}$ and $\Delta\chi$ will keep their original values. So, our $r$ coordinate will range from 1 to $r_{\rm max}/r_+$. For convenience, we write

$$f(r) = 1 - \frac{1}{r^d}. \tag{5.2.5}$$

In the metric (5.1.5), if we take a slice of the boundary at $t = 0$, the null boundaries of the Wheeler-DeWitt patch are given by

$$t(r) = \pm\ell^2 \int_r^{r_{\rm max}/r_+} \frac{dr'}{r'^2\sqrt{f(r')}}. \tag{5.2.6}$$

The volume integral is

$$S_{\rm Vol} = -\frac{2d\, V_{\vec{x}}\,\Delta\chi\, r_+^{d-1}}{\ell^{d+1}}\int_1^{r_{\rm max}/r} dr\, r^{d-1} 2t(r), \tag{5.2.7}$$

where the factor of $r_+^{d-1}$ comes from noting that $\tilde{V}_{\vec{x}}\Delta\tilde{\chi} = r_+^{d-1}V_{\vec{x}}\,\Delta\chi$. If we write

$$F(r) = \int_r^{r_{\rm max}/r_+} \frac{dr'}{r'^2}\left(1-\frac{1}{r'^d}\right)^{-1/2}, \tag{5.2.8}$$

then this becomes

$$S_{\rm Vol} = -\frac{4d\, V_{\vec{x}}\,\Delta\chi\, r_+^{d-1}}{\ell^{d-1}}\int_1^{r_{\rm max}/r_+} r^{d-1}F(r)\, dr. \tag{5.2.9}$$

The tangent to the null surface is

$$k = \alpha \left( \frac{\ell}{r^2} \partial_t - \frac{\sqrt{f(r)}}{\ell} \partial_r \right) \tag{5.2.10}$$

on $F$ and

$$\bar{k} = \beta \left( \frac{\ell}{r^2} \partial_t + \frac{\sqrt{f(r)}}{\ell} \partial_r \right) \tag{5.2.11}$$

on $P$, where $\alpha$, $\beta$ are some arbitrary positive constants. The corner term in the action is

$$S_\Sigma = -\frac{2V_{\vec{x}}\,\Delta\chi}{l^{d-1}} r_{\max}^{d-1} \sqrt{f(r_{\max}/r_+)} \ln\left( \frac{\alpha\beta r_+^2}{r_{\max}^2} \right). \tag{5.2.12}$$

The expansions are

$$\Theta_F = -\alpha \frac{\sqrt{f(r)}}{\ell} \frac{1}{\sqrt{\gamma}} \frac{\partial\sqrt{\gamma}}{\partial r} = -\alpha \frac{\sqrt{f(r)}}{\ell} \left( \frac{f'(r)}{2f(r)} + \frac{d-1}{r} \right), \tag{5.2.13}$$

$$\Theta_P = \beta \frac{\sqrt{f(r)}}{\ell} \frac{1}{\sqrt{\gamma}} \frac{\partial\sqrt{\gamma}}{\partial r} = \beta \frac{\sqrt{f(r)}}{\ell} \left( \frac{f'(r)}{2f(r)} + \frac{d-1}{r} \right), \tag{5.2.14}$$

so the surface integrals are

$$S_{\rm F} = 2V_{\vec{x}}\,\Delta\chi \frac{r_+^{d-1}}{\ell^{d-1}} \int_1^{r_{\max}/r_+} \sqrt{f(r)} r^{d-1} \left( \frac{f'(r)}{2f(r)} + \frac{d-1}{r} \right) \ln\left| \frac{\ell\Theta_F}{d-1} \right| dr \tag{5.2.15}$$

and

$$S_{\rm P} = 2V_{\vec{x}}\,\Delta\chi \frac{r_+^{d-1}}{\ell^{d-1}} \int_1^{r_{\max}/r_+} \sqrt{f(r)} r^{d-1} \left( \frac{f'(r)}{2f(r)} + \frac{d-1}{r} \right) \ln\left| \frac{\ell\Theta_P}{d-1} \right| dr \tag{5.2.16}$$

So the total integral is

$$\begin{aligned} S' = \frac{2V_{\vec{x}}\,\Delta\chi}{\ell^{d-1}} \Bigg[ & -2r_+^{d-1} d \int_1^{r_{\max}/r_+} r^{d-1} F(r)\, dr \\ & - \sqrt{f(r_{\max}/r_+)} r_{\max}^{d-1} \ln\left( \frac{\alpha\beta r_+^2}{r_{\max}^2} \right) \\ & + r_+^{d-1} \int_1^{r_{\max}/r_+} \sqrt{f(r)} r^{d-1} \left( \frac{f'(r)}{2f(r)} + \frac{d-1}{r} \right) \ln\left| \frac{\ell\Theta_F}{d-1} \right| dr \\ & + r_+^{d-1} \int_1^{r_{\max}/r_+} \sqrt{f(r)} r^{d-1} \left( \frac{f'(r)}{2f(r)} + \frac{d-1}{r} \right) \ln\left| \frac{\ell\Theta_P}{d-1} \right| dr \Bigg]. \end{aligned} \tag{5.2.17}$$

This integral is a function of $r_{\max}$ and $r_+$, which is homogeneous of degree $d-1$. It is straightforward to evaluate these expressions numerically for fixed values of the parameters. In figure 5.1, we plot the action as a function of $r_+$ at fixed $r_{\max}$; in

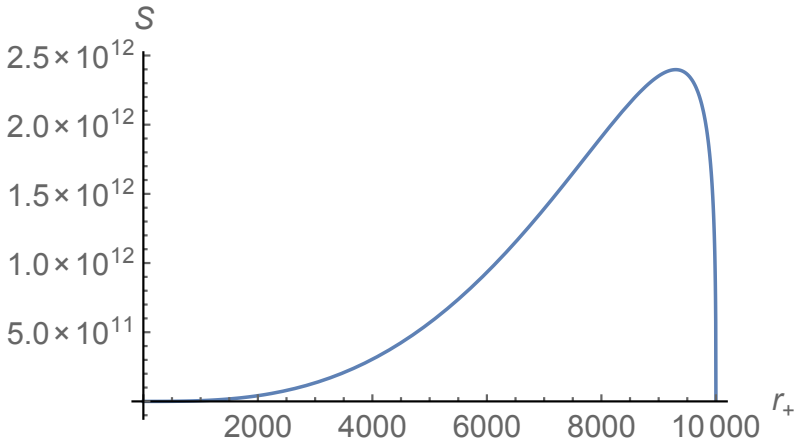


Figure 5.1: The action, omitting the overall factor of $2V_{\vec{x}}\,\Delta\chi/\ell^{d-1}$, as a function of $r_+$ at fixed $r_{\max} = 10000$. We see that it initially increases with $r_+$, but eventually decreases to zero as $r_+ \to r_{\max}$. The initial increase scales as $r_+^{d-1}$, as indicated by the general scaling argument, with $I_0$ found to be approximately 1.27.

figure 5.2, we plot the action as a function of $r_{\max}$ at fixed $r_+$.

We see that the action initially increases at small $r_+$, indicating that $I_0$ is positive. This is qualitatively different from the behaviour of the volume (5.1.6). As before, the increase comes from the negative volume contribution; increasing $r_+$ decreases the volume of the Wheeler-DeWitt patch, while the volume contribution to the action is negative.

In the CA calculation, the complexity for antiperiodic boundary conditions is higher than for periodic boundary conditions. Equally, the complexity for the excited state represented by the pure AdS solution with antiperiodic boundary conditions is lower than that of the ground state.

We see that numerically the action goes to zero as $r_+ \to r_{\max}$. It is interesting to compare the approach to zero in this regime to the volume calculation (5.1.6). Suppose $r_{\max} - r_+ \ll r_+$, and define $\epsilon = r_{\max}/r_+ - 1$. Set $r = r_+(1+\epsilon z)$, so $z \in (0,1)$. Then

$$f(r) \approx (r - r_+) f'(r_+) \approx \epsilon z d, \tag{5.2.18}$$

and $F(r) \sim \int dr/\sqrt{f(r)}$ scales as $\sqrt{\epsilon}$, so that the volume contribution to the action scales as $\epsilon^{3/2}$. The contributions from $\Sigma$ scale as $\sqrt{f}$, that is as $\sqrt{\epsilon}$, but the slowest falloff comes from the expansion contributions on the null surfaces:

$$\Theta_{F,P} \sim \frac{f'}{\sqrt{f}} \sim \frac{1}{\sqrt{\epsilon}}, \tag{5.2.19}$$

so

$$S_{F,P} \sim \int \frac{f'}{\sqrt{f}} \ln \left| \frac{\ell \Theta_{F,P}}{d-1} \right| dr \sim \sqrt{\epsilon} \ln \epsilon. \tag{5.2.20}$$

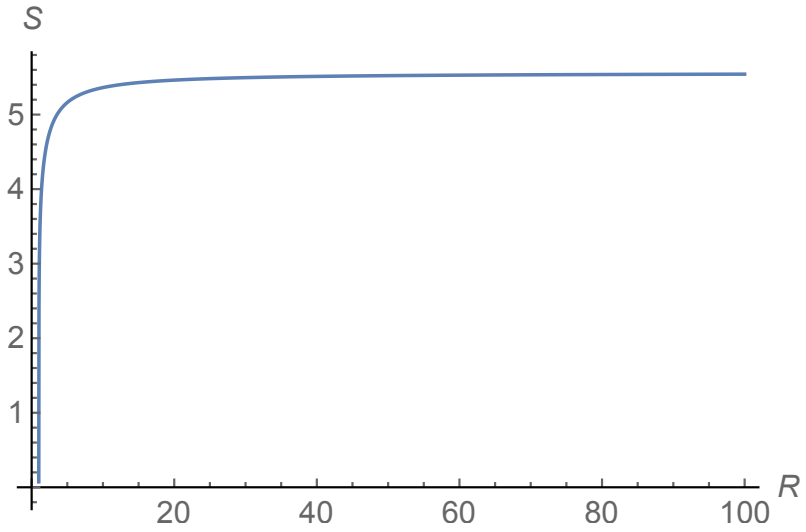


Figure 5.2: The action, omitting the overall factor of $2V_{\vec{x}}\,\Delta\chi/\ell^{d-1}$, as a function of $r_{\max}$ at fixed $r_+ = 1$. We see that it is a monotonically increasing function of $r_{\max}$, which seems physically reasonable behaviour for the complexity.

Thus, the action goes to zero more slowly than the volume, as

$$\sqrt{r_{\max} - r_+}\,\ln(r_{\max} - r_+). \tag{5.2.21}$$

## 5.3 Lattice calculations

We have found that, as for the 'bubble of nothing' case of chapter 4, the holographic complexity calculations for the AdS soliton give qualitatively different results for the two calculation methods. It is interesting to understand what notions of complexity we can identify in the field theory that could reproduce these behaviours. Since the AdS soliton is distinguished by the boundary conditions for fermions, we want to consider a fermionic theory. We do so on a rectangular lattice, considering both the case where the fermions have conventional periodic boundary conditions on all the spatial directions, and the case with antiperiodic boundary conditions on one spatial direction and periodic boundary conditions in the remaining directions. We study the difference between the complexity with the antiperiodic boundary conditions and the complexity with the periodic boundary conditions as a function of the size of the spatial direction with the changing boundary conditions. These results can then be compared with the results of the holographic complexity calculations.

Complexity for fermionic field theories was previously considered by Jordan et al. [43]. Our analysis will also draw inspiration from the recent study of scalar field theories by Jefferson and Myers [42], in which connections to the holographic calculation were also considered.

### 5.3.1 Free fermion theory

We will first review the details that we need of the lattice fermion theory. We consider a theory of a single free fermion $\psi(\vec{x})$ on a spatial lattice. We will discuss explicitly lattices in two and three dimensional spacetimes. The generalisation to higher dimensions has some additional technical complications, so we leave it to an appendix.

The simplest case is two dimensions. Then the lattice has a single spatial direction; we can take either periodic or antiperiodic boundary conditions on this direction. The absence of additional spatial directions with periodic boundary conditions makes this case rather special.[1] We have $N$ lattice sites, $x_i = ia$, $i = 0, \ldots, N$, with $x_N = x_0$, and the boundary condition is $\psi(x_N) = \pm\psi(x_0)$ for the periodic and antiperiodic cases respectively. The Hamiltonian of the free fermion theory is

$$H = a\sum_{i=0}^{N-1}\Bigg[m\bar{\psi}(x_i)\psi(x_i) - i\bar{\psi}(x_i)\gamma^1\frac{\psi(x_i+a)-\psi(x_i-a)}{2a} - r\bar{\psi}(x_i)\frac{\psi(x_i+a)-2\psi(x_i)+\psi(x_i-a)}{2a}\Bigg], \quad (5.3.1)$$

where the last term is the Wilson term, used to prevent fermion doubling [84], and $r > 0$ is the Wilson parameter[2]. The fermion $\psi$ has two components, we define $\bar{\psi} = \psi^\dagger\gamma^0$, and we work with the gamma matrix representation[3]

$$\gamma^0 = \begin{pmatrix} 0 & -i \\ i & 0 \end{pmatrix}, \qquad \gamma^1 = \begin{pmatrix} 0 & -i \\ -i & 0 \end{pmatrix}. \quad (5.3.2)$$

We will primarily work in momentum space, writing

$$\psi(x_j) = \frac{1}{\sqrt{N}}\sum_{i=0}^{N-1} e^{-ip_i x_j}\psi(p_i), \quad (5.3.3)$$

where the momentum lives in the dual lattice or Brillouin zone; for periodic boundary conditions,

$$p_i = \frac{2\pi}{Na}i, \qquad i \in \mathbb{Z}_N, \quad (5.3.4)$$

[1] From the holographic perspective, with a two-dimensional boundary the AdS soliton is actually global $AdS_3$, and the geometry in the bulk does not change as we vary $\Delta_\chi$.

[2] The addition of the Wilson term — an irrelevant operator — to the action does not change the continuum limit. It does, however, impose a mass proportional to $r/a$ to the spurious fermion species that arise in the lattice theory due to fermion doubling [32].

[3] Note that our Clifford algebra conventions correspond to taking the lattice theory's spacetime metric to be $ds^2 = dt^2 - dx^2$, the opposite sign convention to our holographic discussion. We have adopted this convention for consistency with standard references.

while for antiperiodic boundary conditions

$$p_i = \frac{2\pi}{Na}\left(i + \frac{1}{2}\right). \tag{5.3.5}$$

The Hilbert space can be written as a tensor product of the Hilbert space $\mathcal{H}_p$ acted on by the fermionic operators $\psi(p)$ at each momentum. The Hamiltonian in momentum space is

$$H = a\sum_{p\in\Omega}\left[m\bar{\psi}(p)\psi(p) + \frac{\sin(pa)}{a}\bar{\psi(p)}\gamma^1\psi(p) + \frac{2r}{a}\sin^2\left(\frac{pa}{2}\right)\bar{\psi}(p)\psi(p)\right], \tag{5.3.6}$$

where $\Omega$ is the lattice of momentum values in (5.3.4) or (5.3.5) depending on the boundary conditions. The term in the Hamiltonian at a given momentum has eigenspinors[4]

$$u = \frac{1}{\sqrt{2E}}\begin{pmatrix}\sqrt{E-P}\\ i\sqrt{E+P}\end{pmatrix}, \qquad v = \frac{1}{\sqrt{2E}}\begin{pmatrix}\sqrt{E+P}\\ -i\sqrt{E-P}\end{pmatrix}, \tag{5.3.7}$$

with eigenvalues $\pm E$, where

$$P = \frac{\sin(pa)}{a}, \qquad M = m + \frac{2r}{a}\sin^2\left(\frac{pa}{2}\right), \qquad E = \sqrt{M^2+P^2}. \tag{5.3.8}$$

Thus, the fermion can be written in terms of ladder operators as

$$\psi(p) = u(p)a(p) + v(p)b^\dagger(p), \tag{5.3.9}$$

and the ground state is the state annihilated by $a(p_i), b(p_i)$ for all $p_i$; it is the tensor product of the ground state in each $\mathcal{H}_p$.

For the three dimensional case, we can find a representation of the Clifford algebra by enlarging that used in two dimensions by adding

$$\gamma^2 = \begin{pmatrix} i & 0\\ 0 & -i\end{pmatrix}. \tag{5.3.10}$$

The fermions still have two components. We will take the direction with variable boundary conditions to be the $x$ direction. The spatial lattice has $N_x$ sites in the $x$ direction with lattice spacing $a_x$, and $N_y$ sites in the $y$ direction with lattice spacing $a_y$. The momentum vector then lives in a lattice

$$\vec{p} = \left(\frac{2\pi}{N_x a_x}i, \frac{2\pi}{N_y a_y}j\right) \tag{5.3.11}$$

[4]Usually the convention for negative energy states associates them with momentum $-p$ (see, e.g. Peskin and Schroeder [60]); the convention here will be more convenient for our calculations.

for periodic boundary conditions, and

$$\vec{p} = \left( \frac{2\pi}{N_x a_x} \left( i + \frac{1}{2} \right), \frac{2\pi}{N_y a_y} j \right) \tag{5.3.12}$$

for antiperiodic boundary conditions, where in both cases $i \in \mathbb{Z}_{N_x}$, $j \in \mathbb{Z}_{N_y}$. The Hilbert space is a tensor product of spaces $\mathcal{H}_{\vec{p}}$ associated with each lattice site. The Hamiltonian is

$$H = a_x a_y \sum_{\vec{p} \in \Omega} \Bigg[ m \bar{\psi}(\vec{p}) \psi(\vec{p}) + \frac{\sin(p_x a_x)}{a_x} \bar{\psi}(\vec{p}) \gamma^1 \psi(\vec{p}) + \frac{\sin(p_y a_y)}{a_y} \bar{\psi}(\vec{p}) \gamma^2 \psi(\vec{p}) + 2r \left[ a_x^{-1} \sin^2 \left( \frac{p_x a_x}{2} \right) + a_y^{-1} \sin^2 \left( \frac{p_y a_y}{2} \right) \right] \bar{\psi}(\vec{p}) \psi(\vec{p}) \Bigg], \tag{5.3.13}$$

where $\Omega$ is the relevant momentum lattice. The eigenspinors at a given momentum are

$$u = \frac{1}{\sqrt{2E}} \begin{pmatrix} \sqrt{E - P_x} \\ i e^{i\beta_y} \sqrt{E + P_x} \end{pmatrix}, \qquad v = \frac{1}{\sqrt{2E}} \begin{pmatrix} \sqrt{E + P_x} \\ -i e^{i\beta_y} \sqrt{E - P_x} \end{pmatrix}, \tag{5.3.14}$$

with eigenvalues $\pm E$, where

$$P_i = \frac{\sin(p_i a_i)}{a_i}, \quad M = m + 2r \sum_i a_i^{-1} \sin^2 \left( \frac{p_i a_i}{2} \right), \quad E = \sqrt{M^2 + \vec{P}^2} \tag{5.3.15}$$

and

$$e^{i\beta_y} = \frac{M + i P_y}{\sqrt{M^2 + P_y^2}}. \tag{5.3.16}$$

Thus, the fermion can again be written as

$$\psi(\vec{p}) = u(\vec{p}) a(\vec{p}) + v(\vec{p}) b^\dagger(\vec{p}), \tag{5.3.17}$$

and the ground state is the state annihilated by $a(\vec{p}), b(\vec{p})$ for all $\vec{p}$; it is the tensor product of the ground state in each $\mathcal{H}_{\vec{p}}$.

### 5.3.2 Complexity

We wish to evaluate the complexity of the ground state in the free fermionic theories reviewed in the previous subsection. There are two key choices we need to make: we need to choose a reference state, and we need to define a measure of the complexity of the transformation from the reference state to the physical ground state.

Jordan et al. [43] take the reference state to be the ground state of the fiducial Hamiltonian

$$H_0 = a_x a_y \sum_{\vec{x}} m_0 \bar{\psi}(\vec{x})\psi(\vec{x}) = a_x a_y \sum_{\vec{p}\in\Omega} m_0 \bar{\psi}(\vec{p})\psi(\vec{p}), \tag{5.3.18}$$

where the kinetic and Wilson terms are removed from the physical Hamiltonian. This Hamiltonian could also be viewed as a high-mass limit of our original Hamiltonian, where the momentum dependence becomes negligible. This is a useful choice as the resulting reference state is a tensor product state in the position space representation and in the momentum space representation, so both the reference and target states are tensor products in the momentum space representation. A similar choice was made in the scalar case by Jefferson and Myers [42], where the reference state was taken to be a fixed Gaussian at each spatial lattice site; the tensor product of these Gaussian states in the spatial basis is also a tensor product of Gaussian states in the momentum basis.

For the two and three-dimensional cases, the eigenspinors of this Hamiltonian are simply

$$u_0 = \frac{1}{\sqrt{2}} \begin{pmatrix} 1 \\ i \end{pmatrix}, \qquad v_0 = \frac{1}{\sqrt{2}} \begin{pmatrix} 1 \\ -i \end{pmatrix}. \tag{5.3.19}$$

We can easily see that these are the high mass or low-momentum limit of the eigenspinors of the physical Hamiltonian found in the previous subsection. We write the spinor operator as

$$\psi(\vec{p}) = u_0 a_0(\vec{p}) + v_0 b_0^\dagger(\vec{p}), \tag{5.3.20}$$

and we take the reference state to be the state annihilated by all the $a_0(\vec{p}), b_0(\vec{p})$ for all $\vec{p}$.

The physical creation and annihilation operators can be related to $a_0$ and $b_0$ by making use of the orthonormality of our eigenspinors, taking inner products in the spinor indices. In the two and three-dimensional cases,

$$a(p) = u^\dagger(\vec{p})\psi(\vec{p}) = u^\dagger u_0 a_0(\vec{p}) + u^\dagger v_0 b_0^\dagger(\vec{p}), \tag{5.3.21}$$

$$b^\dagger(p) = v^\dagger(\vec{p})\psi(\vec{p}) = v^\dagger u_0 a_0(\vec{p}) + v^\dagger v_0 b_0^\dagger(\vec{p}). \tag{5.3.22}$$

The key point is that this is a Bogoliubov-style transformation, mixing creation and annihilation operators, so the vacuum state with respect to $a(p)$, $b(p)$ will be a mixture of particle states with respect to $a_0(p)$, $b_0(p)$. For a given momentum,

$$|00\rangle_{\text{phys}} = u^\dagger u_0 \, |00\rangle_0 - u^\dagger v_0 \, |11\rangle_0 \, . \tag{5.3.23}$$

We note that this is a mixture of states with even numbers of fermions in the reference

basis, so the transformation between the reference ground state and the physical ground state involves only fermion bilinears, so we do not need to worry about the difficulties of simulating fermionic gates reviewed for example by Jordan et al. [43].

The relationship between the different creation and annihilation operators then allows us to determine how the physical vacuum can be written in terms of reference basis states. For two dimensions, this gives

$$\begin{aligned}|00\rangle_{\text{phys}} &= \frac{1}{2\sqrt{E}}\left[\left(\sqrt{E+P}+\sqrt{E-P}\right)|00\rangle_0 - \left(\sqrt{E+P}-\sqrt{E-P}\right)|11\rangle_0\right] \\ &= \sqrt{\frac{E+M}{2E}}\,|00\rangle_0 - \sqrt{\frac{E-M}{2E}}\,|11\rangle_0\,.\end{aligned} \tag{5.3.24}$$

For three dimensions, we have

$$\begin{aligned}|00\rangle_{\text{phys}} = \frac{1}{2\sqrt{E}}\Big[&\left(e^{-i\beta_y}\sqrt{E+P_x}+\sqrt{E-P_x}\right)|00\rangle_0 \\ &- \left(e^{-i\beta_y}\sqrt{E+P_x}-\sqrt{E-P_x}\right)|11\rangle_0\Big].\end{aligned} \tag{5.3.25}$$

By changing the phase of the physical ground state, we can simplify this to

$$|00\rangle_{\text{phys}} = \sqrt{\frac{E+M}{2E}}\,|00\rangle_0 - e^{i\phi_2}\sqrt{\frac{E-M}{2E}}\,|11\rangle_0\,, \tag{5.3.26}$$

where

$$e^{i\phi_2} = \frac{P_x - iP_y}{P_x + iP_y}. \tag{5.3.27}$$

Note that unlike the scalar case in [42], there is no dependence on the mass scale $m_0$ in the fiducial Hamiltonian. The reference ground state is the same, independent of which $H_0$ we choose.

Having fixed the reference state, we now wish to compute the complexity of the least complex unitary operator $U$ such that the physical ground state $|\psi\rangle = U\,|\psi\rangle_0$, where $|\psi\rangle_0$ is the reference state. Ideally, to respect the locality of the field theory, we would like to do this calculation taking as an elementary gate set some set of unitary operators which act on nearest neighbour sites in the spatial lattice. However, this calculation is extremely difficult, so following Jefferson and Myers [42], we will make the simplifying assumption that we can take the elementary gate set to include unitary operators acting on the individual *momentum* sites in the momentum lattice. (Such operators can be built from a linear combination of operators acting on pairs of lattice sites in the spatial lattice, but we need to include arbitrary pairs of sites.)

Making this assumption allows us to exploit the special structure of our states: our ground state is the product of the ground state $|\vec{0}\rangle_{\text{phys}}$ in $\mathcal{H}_p$ at each momentum, and our reference state is the product of $|\vec{0}\rangle_0$ in $\mathcal{H}_p$ at each momentum, so it is plaus-

ible that the least complex unitary will also have a tensor product decomposition, $U = \otimes_p U_p$. That is, we expect, as in the work of Jefferson and Myers [42], that the path of least complexity with such an elementary gate set will not involve introducing entanglement between different momenta at intermediate scales. Identifying the appropriate unitary $U$ then reduces to identifying an appropriate $U_p$ at each momentum.

In the two and three-dimensional cases, the transformations (5.3.24), (5.3.25) from the reference state to the physical ground state at a given momentum can be implemented by a unitary transformation on the two-dimensional subspace of the Hilbert space spanned by $|00\rangle_0$, $|11\rangle_0$. (We assume that considering more general transformations in $\mathcal{H}_p$ that take us out of this subspace will not reduce the complexity.) Such unitary transformations can be parametrized as

$$U_p = e^{i\alpha} \begin{pmatrix} e^{i\phi_1} \cos\theta & e^{i\phi_2} \sin\theta \\ -e^{-i\phi_2} \sin\theta & e^{-i\phi_1} \cos\theta \end{pmatrix}. \tag{5.3.28}$$

Requiring that the unitary maps $|00\rangle_0$ to $|00\rangle_{\text{phys}}$ fixes the first column of $U_p$, giving three constraints on the parameters (since the target state is normalized, its form in terms of $|00\rangle_0$ and $|11\rangle_0$ involves three free parameters); that leaves one free parameter in $U_p$, which we need to minimize over.

As for Jefferson and Myers [42], we will be inspired by the geometric view of quantum computation of Nielsen et al. [58, 59, 25] to take a geodesic distance in a suitable metric in the space of unitaries as a proxy for the complexity. In the space at a given momentum, we will take the usual metric on $U(2)$,

$$ds^2 = -\frac{1}{2} \operatorname{tr}(dU\, U^{-1}\, dU\, U^{-1}) = d\alpha^2 + d\theta^2 + \cos^2\theta\, d\phi_1^2 + \sin^2\theta\, d\phi_2^2. \tag{5.3.29}$$

The remaining parameter in $U_p$ is determined by minimizing the distance from the identity in this metric.[5]

To calculate the overall complexity, we need to combine the complexities of the individual $U_p$ to obtain a complexity for $U$. We will simply sum up the complexities of each of the $U_p$:

$$\mathcal{C}(U) = \sum_{p \in \Omega} \mathcal{C}(U_p); \tag{5.3.30}$$

in the geometrical language of [58], this corresponds to taking an $F_1$ or 'Manhattan' metric, where the total distance is the sum of the distances along each of the basis directions. This is a natural choice for the calculation of complexity; it can be thought of as adding contributions from the different elementary gates acting on

[5] This minimization to determine an appropriate $U_p$ becomes more difficult in higher dimensions; see the discussion for four dimensions in the appendix.

each $\mathcal{H}_p$.

It is worth noting however that working in the Manhattan metric makes geometric analysis more challenging, which is why Nielsen et al. [59, 25] sought to replace it with a Riemannian metric with suitable cost factors on directions not corresponding to the elementary gate set. Notably, the Manhattan metric, unlike a Riemannian metric, depends on the choice of basis, so our choice to use gates acting on momentum subspaces in the Hilbert space rather than gates acting on pairs of position subspaces becomes significant. Even though the unitaries acting on a momentum subspace can be written as a linear combination of unitaries acting on position subspaces, taking one rather than the other as the basis in a Manhattan metric leads to a different formula for the complexity.

The choice of a Manhattan metric is supported by the results of Jefferson and Myers [42], who found that it reproduces the UV divergence structure of the holographic calculation. The same will be true in our fermionic calculation; the complexity defined by (5.3.30) is roughly proportional to the number of lattice sites, which we can interpret as the volume in units of the UV cutoff, reproducing the divergence in the holographic calculation. A Riemannian metric built by combining the metrics (5.3.29) would by contrast give a result scaling roughly as the square root of the number of sites. We will, however, not consider these divergent contributions further; our focus is on evaluating the finite difference between the complexities with periodic and antiperiodic boundary conditions,

$$\Delta\mathcal{C} = \mathcal{C}_{\text{anti}} - \mathcal{C}_{\text{per}}. \tag{5.3.31}$$

We now implement this programme for the two- and three-dimensional cases. In the two-dimensional case, the unitary of minimum distance which realises the transformation (5.3.24) is simply a rotation,

$$U_p = \begin{pmatrix} \cos\theta & \sin\theta \\ -\sin\theta & \cos\theta \end{pmatrix} \tag{5.3.32}$$

with

$$\cos\theta = \sqrt{\frac{E+M}{2E}}. \tag{5.3.33}$$

The distance from the identity in the standard metric is simply $\theta$, so we take $\mathcal{C}(U_p) = \theta(p)$. This amounts to taking an infinitesimal rotation in this direction as an element of the elementary gate set.

We sum over the contributions from the individual momenta, and take the difference between antiperiodic and periodic boundary conditions to calculate $\Delta\mathcal{C}$ in (5.3.31). We plot this difference as a function of $L = aN$ in figure 5.3. We see that the difference is positive, as for the holographic CA calculation, but unlike the

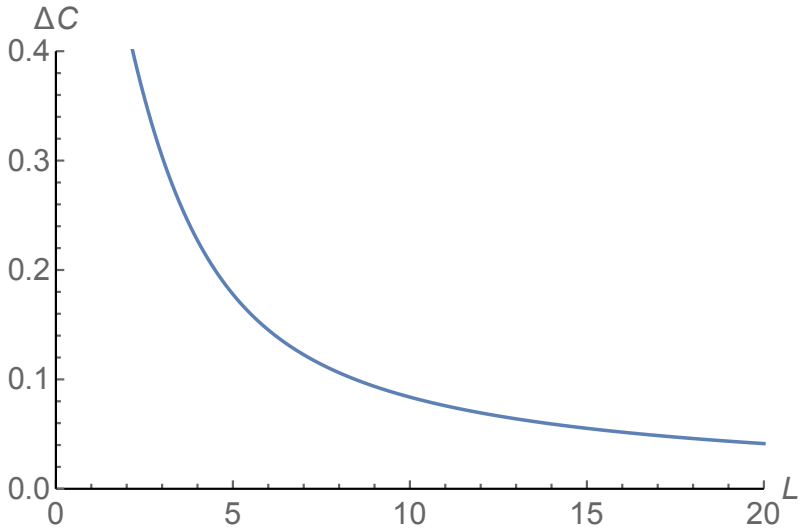


Figure 5.3: The difference, $\Delta\mathcal{C}$, between the complexity of the ground states for a fermion with antiperiodic boundary conditions and a fermion with periodic boundary conditions on a one-dimensional spatial lattice, as a function of the size of the circle. We see that the difference is positive, and decreases as we increase the size of the circle. (Lattice spacing is fixed at 0.002, so that the number of sites increases with the size of the circle. Parameter $r$ associated with the Wilson term is set to 0.1, while $m = 1.0$.)

holographic CV calculation.

We find that the difference decreases as the size of the circle increases. This is unlike the holographic calculation; there, the difference in complexity went as $\Delta\chi\, r_+^{d-1} \propto r_+^{d-2}$ (see (5.2.2)), so in $d = 2$, the difference in the holographic calculation is independent of the size of the circle. This is because in $d = 2$ the AdS soliton is actually global $AdS_3$, and the finite part is the difference in volume or action between the $M = 0$ BTZ black hole and global $AdS_3$, which is some finite constant.

In the three-dimensional case, the simplest unitary realising the transformation (5.3.26) has $\alpha = 0, \phi_1 = 0$,

$$\cos\theta = \sqrt{\frac{E+M}{2E}}, \qquad e^{i\phi_2} = \frac{P_x - iP_y}{P_x + iP_y}, \tag{5.3.34}$$

and the complexity is again $\mathcal{C}(U_p) = \theta(p)$. We add up these contributions for each site in the momentum lattice, and take the difference between antiperiodic and periodic boundary conditions to calculate $\Delta\mathcal{C}$ in (5.3.31). We plot this difference as a function of $L_x$ in figure 5.4. We see that the difference is again positive, and decreases as a function of the size of the circle. In this case this is also the behaviour expected holographically. Holographically, the complexity would fall off as $1/L_x$. The numerical results for the lattice computation exhibit a faster falloff than in the

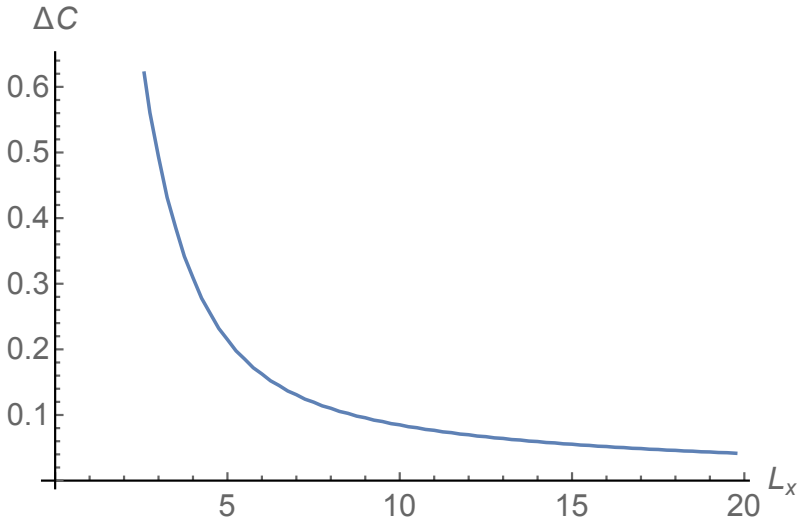


Figure 5.4: The difference $\Delta\mathcal{C}$ between the complexity of the ground states for a fermion with antiperiodic boundary conditions in one direction and a fermion with periodic boundary conditions in both directions on a two-dimensional spatial lattice, as a function of the size of the circle with the varying boundary conditions. (Lattice spacing is set to 0.0004 in both directions, while $r = 0.1$ and $m = 1.0$.)

2D case, but they are not well fit by a simple power law.

We have found that, with our definition of the complexity, the complexity for antiperiodic boundary conditions is higher than for periodic boundary conditions. It seems surprising that the generic expectation that raising the energy increases the complexity is not borne out in this case. It is possible that the key ingredient in the increase in complexity in the antiperiodic case is the difference in the momentum lattices: in the antiperiodic case, the lowest momentum value is non-zero. Since the reference Hamiltonian is the zero-momentum limit of the physical Hamiltonian, this increase in the minimum momentum value may be responsible for the increase in complexity of the ground state relative to the reference state.

In our calculation, we decomposed the unitary in terms of operators acting on different momentum subspaces of the Hilbert space. An important problem for the future is to study the decomposition in terms of operators acting on position subspaces and see if this modifies the results. Our use of the Manhattan metric makes this choice of basis particularly salient, and ultimately one would like to include appropriate penalty factors for non-local transformations in the position space decomposition.

## 5.4 Discussion

We have studied, for a field theory on a torus, the dependence of the complexity of the ground state on the boundary conditions for fermions, both holographically and in a simple lattice model. We compared the results for antiperiodic and periodic boundary conditions for the fermions. In the holographic calculation, the former corresponds to the AdS soliton, where the spacetime closes off at a radius $r_+$ determined by the size $\Delta\chi$ of the circle with antiperiodic boundary conditions, while the latter corresponds to a simple Poincaré-AdS geometry.

Without doing any calculations, we can argue that the holographic complexity for antiperiodic boundary conditions in the regime where $r_+$ is small compared to the UV cutoff $r_{\max}$ will have the form

$$\mathcal{C}_{\text{anti}} \propto V_{\vec{x}}\, \Delta\chi (r_{\max}^{d-1} + I_0 r_+^{d-1} + \ldots), \tag{5.4.1}$$

where $V_{\vec{x}}$ is the volume in the remaining spatial dimensions, $d$ is the spacetime dimension of the field theory, $I_0$ is a purely numerical coefficient, and the suppressed terms vanish in the limit as $r_{\max} \to \infty$. Since the result for periodic boundary conditions is simply $\mathcal{C}_{\text{per}} \propto V_{\vec{x}}\, \Delta\chi\, r_{\max}^{d-1}$, the difference between periodic and antiperiodic boundary conditions is finite.

By explicit calculation, we find that the result in the complexity volume (CV) calculation is $I_0 = -1$, while for the complexity action (CA) calculation $I_0$ is roughly 1.27. This provides a qualitative distinction between these two bulk calculations. In the CV calculation, the change in boundary conditions reduces the complexity, while in the CA calculation it increases it. We initially thought a decrease was the more intuitive result, as the ground state with antiperiodic boundary conditions has lower energy than the one with periodic boundary conditions. However, the ground state is far from maximum complexity, so it is important to understand the overall effect of the change in boundary conditions.

We investigated this in a simple lattice calculation for a free fermion, extending the work of Jefferson and Myers [42] for bosons. The complexity of the fermion ground state is divergent, as for bosons, but the difference between the complexity for antiperiodic and periodic boundary conditions is finite. We find that this is positive, as in the holographic CA calculation.

These results thus seem to support the holographic action calculations over the volume calculations. However, in the lattice calculation, there are a number of choices and approximations that we needed to make to render the calculation feasible, and improving this calculation is an important goal for future work. In particular, we would like to move from considering a basis of elementary operations that acts on the factors in a momentum space decomposition of the Hilbert space to one that acts

in a position space decomposition, and ultimately to incorporate spatial locality into the calculation by penalizing operations that are not acting on nearest neighbour sites in position space.

It would also be interesting to study the dependence of the complexity on other changes in the ground state, for example if we deform the field theory by relevant or marginal operators.

# Chapter 6

# Conclusions

This thesis summarizes work on two projects, on the related areas of quantum chaos in gauge/gravity duality and holographic complexity. The first of these projects, described in detail in chapter 2 extended the research of Shenker and Stanford [72] by considering both rotating and charged black holes. Emphasis was placed on the holographic analysis of how perturbations to the boundary field theory result in changes to the two-point correlation functions between the two boundaries. The results obtained were not unexpected. Similar shock wave geometries were obtained to that seen by Shenker and Stanford [72], with associated elongation of the geodesics passing through the wormhole and the resultant effect on the dual theory of a reduction of the correlation (and local entanglement) between points on the two copies of the CFT. A brief look at generalizing the geodesic calculations to higher dimensional cases revealed added difficulties — geodesics would need to calculated in complexified spacetime — so this was left to future research, though one suspects that the results would be similar, qualitatively at least, to the $2 + 1$ dimensional case.

In contrast, our work on holographic complexity produced some surprises and hence this makes up the bulk of the thesis. We started, in chapter 3, by looking at the divergence structure of both the CV and the CA forms of the holographic complexity. Part of the aim was to prepare for the analysis of holographic complexity with de Sitter boundaries (chapter 4), where such divergences are not expected to simply cancel when analysing the rate of change of the complexity. However, a bigger motivation for this analysis was the expectation that these divergent contributions correspond to an integral, physical part of the field theory complexity, in much the same way as the divergent part of the holographic entanglement entropy correspond to contributions from UV modes across the boundary being considered.

Calculations of the divergences in the CV case were straightforward. In contrast, as previously noted by Lehner et al. [46], calculating the action of the Wheeler-

DeWitt patch is not as simple as was initially supposed, requiring a prescription for the contributions of null boundaries and corners between such surfaces, and including an ambiguity in the result. Now, while this ambiguity is not necessarily a bad thing, given the ambiguities in the field theory definition of complexity, coordinate-dependence of the prescription is undesired. We therefore emphasized the need for a counterterm, mentioned by Lehner et al. [46] in appendix B, to eliminate the coordinate dependence. A welcome bonus was that use of this counterterm also eliminated the unphysical-looking leading divergence and other subleading logarithmic divergences.

Examination of the divergences of the two prescriptions revealed similar overall structure, but with different coefficients for subleading terms. However, given that the subleading contributions to the action depend on how we cut off the Wheeler-DeWitt patch, it was not clear how much weight to assign to this finding. However, subsequent work analysing complexity in de Sitter space, summarized in chapter 4, led to a bigger surprise. Most notably, the CV and CA prescriptions produced qualitatively different results when comparing gapped solutions (dual to 'bubble of nothing' spacetimes) with ungapped (dual to a spacetime with a horizon). The CV prescription, suggested lower complexity for the gapped solutions, which might be expected given their lower energy. The CA prescription suggested higher complexity.

The unexpected results for de Sitter boundaries led us to consider a simpler case in chapter 5: the AdS soliton. The quantitative differences found in chapter 4 were shown to extend to this simpler situation, with the comparison in this case being between the AdS soliton and plain AdS in the bulk, or, on the boundary, between a fermionic theory on a torus with antiperiodic boundary conditions in one direction, and a similar fermionic theory with periodic boundary conditions in all directions. Given the simpler setting, we could investigate the discrepancy further by attempting a direct calculation of complexity in the boundary field theory, extending the lattice-based approach developed by Jefferson and Myers [42]. While there must be some caveats, due to choices and approximations required to make the lattice calculation feasible, the results provide some tentative support for the CA prescription, agreeing with the assessment that the complexity is greater for antiperiodic boundary conditions.

One naturally wonders what these results imply for the two holographic complexity conjectures. Initially, one is inclined to believe that one (or both) of the conjectures are wrong in some way, though one wonders whether to believe in the CV conjecture that produced what, at first, seemed the more intuitive results, or the CA conjecture that is supported by our rudimentary lattice calculations. However, there are (at least) two reasons for delaying judgement. Firstly, the definition of the quantum computational complexity of a state depends on the selection of

some fiduciary reference state (or states). As a result, given states $|A\rangle$ and $|B\rangle$, it is entirely possible for a state $|A\rangle$ to have the higher complexity according to one definition of complexity, but to have lower complexity than state $|B\rangle$ according to a second definition. Secondly, there remains the possibility that some modification to the prescription for the calculation of the action might eliminate these qualitative differences. These questions will be the subject of future research.

# Appendix A

# Lattice fermions in higher dimensions

Here we discuss the lattice fermion theory in the four dimensional case in some detail, and comment on the extension to higher dimensions. In these cases the dimension of $\mathcal{H}_p$ is larger, and as a consequence the transformation between the reference state and the physical ground state is more involved. In four dimensions, we take the Dirac representation of the Clifford algebra, with

$$\gamma^0 = \begin{pmatrix} \mathbb{1} & 0 \\ 0 & -\mathbb{1} \end{pmatrix}, \qquad \gamma^i = \begin{pmatrix} 0 & \sigma^i \\ -\sigma^i & 0 \end{pmatrix}, \tag{A.1}$$

where each entry represents a $2 \times 2$ matrix, and $\sigma^i$ are the Pauli matrices. The fermions then have four components. We will take the direction with variable boundary conditions to be the $x$ direction again. The spatial lattice has $N_x$ sites in the $x$ direction with lattice spacing $a_x$, $N_y$ sites in the $y$ direction with lattice spacing $a_y$, and $N_z$ sites in the $z$ direction with lattice spacing $a_z$. The momentum vector then lives in a lattice

$$\vec{p} = \left( \frac{2\pi}{N_x a_x} i, \frac{2\pi}{N_y a_y} j, \frac{2\pi}{N_z a_z} k \right) \tag{A.2}$$

for periodic boundary conditions, and

$$\vec{p} = \left( \frac{2\pi}{N_x a_x} \left( i + \frac{1}{2} \right), \frac{2\pi}{N_y a_y} j, \frac{2\pi}{N_z a_z} k \right) \tag{A.3}$$

for antiperiodic boundary conditions, where in both cases $i \in \mathbb{Z}_{N_x}$, $j \in \mathbb{Z}_{N_y}$, $k \in \mathbb{Z}_{N_z}$. The Hilbert space is a tensor product of spaces $\mathcal{H}_{\vec{p}}$ associated with each lattice site.

The Hamiltonian is

$$H = a_x a_y a_z \sum_{\vec{p}\in\Omega} \Bigg[ m\bar{\psi}(\vec{p})\psi(\vec{p}) + \sum_i \frac{\sin(p_i a_i)}{a_i} \bar{\psi}(\vec{p})\gamma^i \psi(\vec{p}) + 2r \sum_i a_i^{-1} \sin^2\left(\frac{p_i a}{2}\right) \bar{\psi}(\vec{p})\psi(\vec{p}) \Bigg], \quad \text{(A.4)}$$

where $\Omega$ is the relevant lattice. A convenient choice of eigenstates are

$$u^1 = \frac{1}{\sqrt{2E(E+M)}} \begin{pmatrix} M+E \\ 0 \\ P_z \\ P_x + iP_y \end{pmatrix}, \qquad u^2 = \frac{1}{\sqrt{2E(E+M)}} \begin{pmatrix} 0 \\ M+E \\ P_x - iP_y \\ -P_z \end{pmatrix}, \quad \text{(A.5)}$$

with eigenvalue $E$, and

$$v^1 = \frac{1}{\sqrt{2E(E+M)}} \begin{pmatrix} -P_z \\ -P_x - iP_y \\ M+E \\ 0 \end{pmatrix}, \qquad v^2 = \frac{1}{\sqrt{2E(E+M)}} \begin{pmatrix} -P_x + iP_y \\ P_z \\ 0 \\ M+E \end{pmatrix}, \quad \text{(A.6)}$$

with eigenvalue $-E$, where

$$P_i = \frac{\sin(p_i a_i)}{a_i}, \qquad M^2 = m^2 + 2r \sum_i a_i^{-1} \sin^2\left(\frac{p_i a_i}{2}\right), \qquad E = \sqrt{M^2 + \vec{P}^2}. \quad \text{(A.7)}$$

Writing the fermion as

$$\psi(\vec{p}) = u^\alpha(\vec{p}) a^\alpha(\vec{p}) + v^\alpha(\vec{p}) b^{\alpha\dagger}(\vec{p}), \quad \text{(A.8)}$$

$\alpha = 1, 2$, the ground state is the state annihilated by $a^\alpha(\vec{p}), b^\alpha(\vec{p})$ for all $\vec{p}$; it is the tensor product of the ground state in each $\mathcal{H}_{\vec{p}}$.

Taking the reference Hamiltonian $H_0 = a_x a_y a_z \sum_{\vec{p}\in\Omega} m_0 \bar{\psi}(\vec{p})\psi(\vec{p})$, the diagonal structure of $\gamma^0$ makes the eigenspinors even simpler; they are just

$$u_0^1 = \begin{pmatrix} 1 \\ 0 \\ 0 \\ 0 \end{pmatrix}, \quad u_0^2 = \begin{pmatrix} 0 \\ 1 \\ 0 \\ 0 \end{pmatrix}, \quad v_0^1 = \begin{pmatrix} 0 \\ 0 \\ 1 \\ 0 \end{pmatrix}, \quad v_0^2 = \begin{pmatrix} 0 \\ 0 \\ 0 \\ 1 \end{pmatrix}. \quad \text{(A.9)}$$

The positive frequency eigenspinors for the physical Hamiltonian overlap with both of the negative frequency eigenspinors of the reference Hamiltonian. Thus

$$a^\alpha(p) = u^{\alpha\dagger}(\vec{p})\psi(\vec{p}) = u^{\alpha\dagger} u_0^\beta a_0^\beta(\vec{p}) + u^{\alpha\dagger} v_0^\beta b_0^{\beta\dagger}(\vec{p}), \quad \text{(A.10)}$$

$$b^{\alpha\dagger}(p) = v^{\alpha\dagger}(\vec{p})\psi(\vec{p}) = v^{\alpha\dagger}u_0^\beta a_0^\beta(\vec{p}) + v^{\alpha\dagger}v_0^\beta b_0^{\beta\dagger}(\vec{p}), \tag{A.11}$$

where

$$\begin{aligned}
u^{\alpha\dagger}u_0^\beta &= \sqrt{\frac{E+M}{2E}}\delta^{\alpha\beta}, & v^{\alpha\dagger}v_0^\beta &= \sqrt{\frac{E+M}{2E}}\delta^{\alpha\beta}, \\
u^{1\dagger}v_0^1 &= \frac{P_z}{\sqrt{2E(E+M)}}, & u^{1\dagger}v_0^2 &= \frac{P_x - iP_y}{\sqrt{2E(E+M)}}, \\
u^{2\dagger}v_0^1 &= \frac{P_x + iP_y}{\sqrt{2E(E+M)}}, & u^{1\dagger}v_0^2 &= -\frac{P_z}{\sqrt{2E(E+M)}}, \\
v^{1\dagger}u_0^1 &= -\frac{P_z}{\sqrt{2E(E+M)}}, & v^{1\dagger}u_0^2 &= \frac{-P_x + iP_y}{\sqrt{2E(E+M)}}, \\
v^{2\dagger}u_0^1 &= -\frac{P_x + iP_y}{\sqrt{2E(E+M)}}, & v^{1\dagger}u_0^2 &= \frac{P_z}{\sqrt{2E(E+M)}}.
\end{aligned} \tag{A.12}$$

Using these relations, we find that the physical ground state is[1]

$$\begin{aligned}
|0000\rangle_{\text{phys}} = \frac{1}{2E}\big[&(E+M)\,|0000\rangle_0 + P_z\,|0011\rangle_0 + (P_x + iP_y)\,|0110\rangle \\
&- (P_x - iP_y)\,|1001\rangle_0 - P_z\,|1100\rangle_0 - (E-M)\,|1111\rangle_0\big].
\end{aligned} \tag{A.13}$$

We want a unitary realising the transformation (A.13). This is in a six-dimensional subspace of the Hilbert space $\mathcal{H}_p$, so we're looking for a $U(6)$ transformation $U_p$. The ambiguity in the choice of $U_p$ corresponds to left multiplication by a $U(5)$ transformation which fixes $|\vec{0}\rangle_{\text{phys}}$. Minimizing over this $U(5)$ ambiguity to find the $U_p$ closest to the origin in the standard metric on $U(6)$ is non-trivial; we have not carried out the calculation explicitly.

However, we can simplify the problem considerably by noting that the momentum space Hamiltonian (A.4) is

$$H = a_x a_y a_z \sum_{\vec{p}\in\Omega} \left[ M\bar{\psi}(\vec{p})\psi(\vec{p}) + \sum_i P_i \bar{\psi}(\vec{p})\gamma^i\psi(\vec{p}) \right], \tag{A.14}$$

which looks just like the continuum Hamiltonian for a fermion of mass $M$ and momentum $\vec{P}$. As a result, we would expect the distance between the physical vacuum and the reference state in $\mathcal{H}_p$ to be invariant under the symmetries of a continuum theory, and depend only on $P^2$. If we make this assumption, we can determine the dependence on $P^2$ by considering a case with a single momentum component.

[1]Each bit in, e.g. $|0011\rangle_0$, is associated with an annihilation operator, with the order of the bits corresponding with the order $a_0^1$, $b_0^1$, $a_0^2$, $b_0^2$. So $|0011\rangle_0$ is created from the reference state $|0000\rangle_0$ by first applying $b_0^{2\dagger}$ and then $a_0^{2\dagger}$.

For example, take just $P_z$. Then

$$u^1 = \frac{1}{\sqrt{2E(E+M)}} \begin{pmatrix} M+E \\ 0 \\ P_z \\ 0 \end{pmatrix}, \quad u^2 = \frac{1}{\sqrt{2E(E+M)}} \begin{pmatrix} 0 \\ M+E \\ 0 \\ -P_z \end{pmatrix}, \tag{A.15}$$

with eigenvalue $E$, and

$$v^1 = \frac{1}{\sqrt{2E(E+M)}} \begin{pmatrix} -P_z \\ 0 \\ M+E \\ 0 \end{pmatrix} \quad v^2 = \frac{1}{\sqrt{2E(E+M)}} \begin{pmatrix} 0 \\ P_z \\ 0 \\ M+E \end{pmatrix}, \tag{A.16}$$

and $u^1, v^1$ are a mixture of $u_0^1, v_0^1$, while $u^2, v^2$ are a mixture of $u_0^2, v_0^2$. As a result, we can decompose the Hilbert space $\mathcal{H}_p$ as a tensor product of the space acted on by $a^1, b^1$ and the space acted on by $a^2, b^2$, and the physical ground state in $\mathcal{H}_p^1$ is

$$|00\rangle_{\text{phys},1} = \sqrt{\frac{E+M}{2E}} |00\rangle_0 - \sqrt{\frac{E-M}{2E}} |11\rangle_0 , \tag{A.17}$$

while the physical ground state in $\mathcal{H}_p^2$ is

$$|00\rangle_{\text{phys},2} = \sqrt{\frac{E+M}{2E}} |00\rangle_0 + \sqrt{\frac{E-M}{2E}} |11\rangle_0 . \tag{A.18}$$

Thus, the transformation from the reference state to the physical ground state is a product of a rotation in $\mathcal{H}_p^1$ and a rotation in $\mathcal{H}_p^2$. These individually are the same as the two-dimensional case. The complexity is then just the combination of the contributions from $\mathcal{H}_p^1$ and $\mathcal{H}_p^2$. Thinking of this as calculated in the Riemannian metric on the unitaries on $\mathcal{H}_p$, the minimum distance would be obtained by rotating in the two factors simultaneously, giving $\mathcal{C}(U_p) = \sqrt{2}\theta$, where[2]

$$\cos\theta = \sqrt{\frac{E+M}{2E}}. \tag{A.19}$$

We obtained this result by considering a momentum where only $P_z$ was non-zero, but if we assume the complexity is a function only of $P^2$, we can apply this result to all the momenta in the lattice. We can check that we get the same answer by taking a different component, that is taking only $P_x$ or $P_y$ nonzero.

We add up these contributions for each site in the momentum lattice, and take

[2]If we combined the contributions from $\mathcal{H}_p^1$ and $\mathcal{H}_p^2$ in a Manhattan metric, we would have $\mathcal{C}(\vec{p}) = 2\theta$. This seems less appropriate as the way $\mathcal{H}_p$ splits up into a tensor product depends on which component of the momentum we consider; for example taking $P_x$ decomposes $\mathcal{H}_p$ into a subspace acted on by $a^1, b^2$ and a subspace acted on by $a^2, b^1$. But this overall numerical difference is in any case unimportant for our considerations.

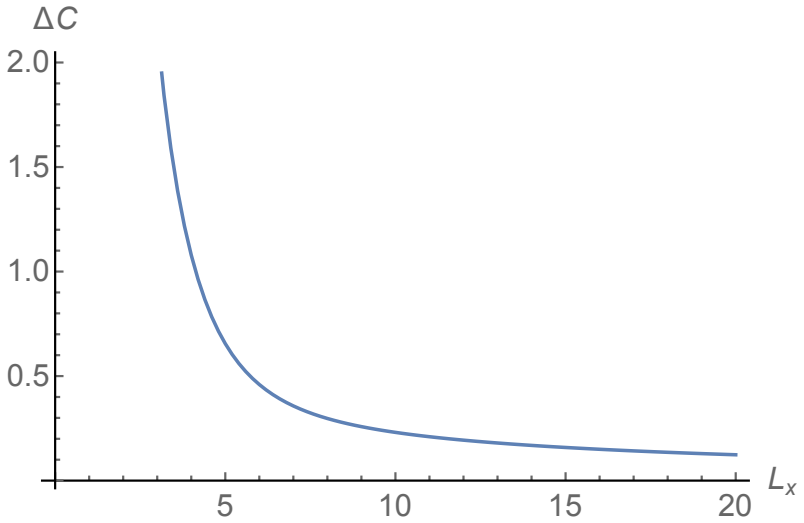


Figure A.1: The difference $\Delta\mathcal{C}$ between the complexity of the ground states for a fermion with antiperiodic boundary conditions in one direction and a fermion with periodic boundary conditions in all directions on a three-dimensional spatial lattice, as a function of the size of the circle with the varying boundary conditions.

the difference between antiperiodic and periodic boundary conditions to calculate $\Delta\mathcal{C}$ in (5.3.31). We plot this difference as a function of $L_x$ in figure A.1. We see that the difference is again positive, and decreases as a function of the size of the circle. In this case this is also the behaviour expected holographically. Holographically, the complexity would fall off as $1/L_x^2$. The numerical results for the lattice computation are closer to $1/L_x$.

We can calculate the complexity in higher dimensions along similar lines. As we increase the spacetime dimension, the dimension of the spinor representation increases, so the calculation for generic momentum values gets more complicated, but we can proceed by doing the calculation in the case where the momentum has only one non-zero component, assuming the complexity at a given momentum is a function only of $P^2$. In the general case, will will take $P$ to be parallel to the $x^1$ axis.

The key, in the 4d case, was that $u^1$, $v^1$ were found to be a mixture of $u_0^1$, $v_0^1$ only, while $u^2$, $v^2$ were a mixture of $u_0^2$, $v_0^2$, allowing us to decompose the Hilbert space into two 2-bit factors. Since the final result should not depend on the representation of the gamma matrices, we select a representation that continues to allow this type of decomposition for higher dimensional cases, e.g. a representation where

$$\gamma^0 = \begin{pmatrix} \mathbb{1}_{n\times n} & 0 \\ 0 & -\mathbb{1}_{n\times n} \end{pmatrix}, \qquad \gamma^1 = \begin{pmatrix} 0 & \mathbb{1}_{n\times n} \\ -\mathbb{1}_{n\times n} & 0 \end{pmatrix}. \tag{A.20}$$

Note that $(\gamma^0)^2 = \mathbb{1}$, $(\gamma^1)^2 = -\mathbb{1}$ and $\{\gamma^0, \gamma^1\} = 0$ as required of gamma matrices[3].

We now follow the approach of Peskin and Schroeder [60, p46] — that is, we find eigenspinors $u^i(p)$, $v^i(p)$ by applying a boost to $u_0^i, v_0^i$ in the spinor representation. The generator of the boost in the $x^1$ direction is given by (3.26) of [60],

$$S^{01} = \frac{i}{4}\left[\gamma^0, \gamma^1\right] = \frac{i}{2}\begin{pmatrix} 0 & \mathbb{1} \\ \mathbb{1} & 0 \end{pmatrix}, \tag{A.21}$$

and we get (see (3.49) of [60])

$$u^i(p) = \exp\left[\frac{\eta}{2}\begin{pmatrix} 0 & \mathbb{1} \\ \mathbb{1} & 0 \end{pmatrix}\right] u_0^i, \tag{A.22}$$

where $\eta$ is the rapidity, satisfying

$$\begin{aligned} M\sinh\eta &= P^1, \\ M\cosh\eta &= E. \end{aligned} \tag{A.23}$$

Calculating how the boost applies to $v_i(p)$ requires some care. Recall that our $v_i(p)$ corresponds to $v_i(-p)$ in [60], so we must apply the boost in the opposite direction. We get

$$v_i(p) = \exp\left[-\frac{\eta}{2}\begin{pmatrix} 0 & \mathbb{1} \\ \mathbb{1} & 0 \end{pmatrix}\right] v_0^i. \tag{A.24}$$

Note that, given the form of $\gamma^0$, the basis vectors $u_0^i$ and $v_0^i$ can simply be the

[3] In order to create a complete set of matrices, with $\gamma^0$ and $\gamma^1$ as given in (A.20), we start with $d = 2$, defining

$$\gamma^0_{(2)} = \begin{pmatrix} 1 & 0 \\ 0 & -1 \end{pmatrix}, \quad \gamma^1_{(2)} = \begin{pmatrix} 0 & 1 \\ -1 & 0 \end{pmatrix}, \quad \gamma^*_{(2)} = \gamma^0_{(2)}\gamma^1_{(2)} = \begin{pmatrix} 0 & 1 \\ 1 & 0 \end{pmatrix},$$

where $\gamma^*$ plays the role of $\gamma^5$ for $d = 4$. For even dimensions, we define the gamma matrices recursively.

$$\begin{aligned} \gamma^a_{(d+2)} &= \gamma^a_{(d)} \otimes \mathbb{1}_{2\times 2}, && (a < d), \\ \gamma^d_{(d+2)} &= \gamma^*_{(d)} \otimes i\sigma^1, \\ \gamma^{d+1}_{(d+2)} &= \gamma^*_{(d)} \otimes i\sigma^2, \\ \gamma^*_{(d+2)} &= i^{d/2}\gamma^0_{(d+2)}\gamma^1_{(d+2)}\cdots\gamma^{d+1}_{(d+2)}. \end{aligned}$$

One can then easily check that these gamma matrices satisfy the Clifford algebra.

In an odd number, $d+1$, of dimensions, we simply define

$$\begin{aligned} \gamma^a_{(d+1)} &= \gamma^a_{(d)}, && (a < d), \\ \gamma^d_{(d+1)} &= i\gamma^*_{(d)}. \end{aligned}$$

standard unit vectors, i.e.

$$u_0^1 = \begin{pmatrix} 1 \\ 0 \\ 0 \\ \vdots \\ 0 \\ \cdots \\ 0 \\ 0 \\ \vdots \\ 0 \end{pmatrix}, \quad u_0^2 = \begin{pmatrix} 0 \\ 1 \\ 0 \\ \vdots \\ 0 \\ \cdots \\ 0 \\ 0 \\ \vdots \\ 0 \end{pmatrix}, \quad \ldots \quad v_0^1 = \begin{pmatrix} 0 \\ 0 \\ 0 \\ \vdots \\ 0 \\ \cdots \\ 1 \\ 0 \\ \vdots \\ 0 \end{pmatrix}, \text{ etc.} \tag{A.25}$$

Expanding the exponential, we have

$$u_i(p) = \cosh \frac{\eta}{2} \begin{pmatrix} \mathbb{1} & 0 \\ 0 & \mathbb{1} \end{pmatrix} u_0^i + \sinh \frac{\eta}{2} \begin{pmatrix} 0 & \mathbb{1} \\ \mathbb{1} & 0 \end{pmatrix} u_0^i \tag{A.26}$$

and similar for $v_i(p)$. But note that this is just[4]

$$\begin{aligned} u_i(p) &= \cosh\left(\frac{\eta}{2}\right) u_0^i + \sinh\left(\frac{\eta}{2}\right) v_0^i, \\ v_i(p) &= \cosh\left(\frac{\eta}{2}\right) v_0^i - \sinh\left(\frac{\eta}{2}\right) u_0^i, \end{aligned} \tag{A.27}$$

So, as in the calculations for $d = 4$, we find that

$$u^{i\dagger}(p)u_0^j = u^{i\dagger}(p)v_0^j = v^{i\dagger}(p)u_0^j = v^{i\dagger}(p)v_0^j = 0 \tag{A.28}$$

whenever $i \neq j$. As a result, the problem of writing the vacuum state $|00\ldots0\rangle$ in terms of the disconnected lattice states $|\cdot\cdot\ldots\cdot\rangle_0$ can be decomposed into a collection of $n$ 2-bit subproblems as before. Continuing the calculation reveals that each subproblem is the same as the subproblems of the 4d case. As before, if the subproblem complexities are combined using a Riemannian metric, we get $\mathcal{C}(U_p) = \sqrt{n}\theta$ where

$$\cos\theta = \sqrt{\frac{E+M}{2E}}, \tag{A.29}$$

by rotating in all of the factors of the Hilbert space simultaneously.

[4]Note the different normalization.

# Bibliography


[1] Mohsen Alishahiha. Holographic complexity. *Phys. Rev. D*, 92:126009, 2015, arXiv:1509.06614.

[2] Ahmed Almheiri, Donald Marolf, Joseph Polchinski, Douglas Stanford, and James Sullya. An apologia for firewalls. *JHEP*, 09:18, 2013, arXiv:1304.6483.

[3] Ahmed Almheiri, Donald Marolf, Joseph Polchinski, and James Sullya. Black holes: complementarity or firewalls? *JHEP*, 02:062, 2013, arXiv:1207.3123.

[4] Martin Ammon and Johanna Erdmenger. *Gauge/Gravity Duality: Foundations and Applications*. Cambridge University Press, 2015.

[5] Tomás Andrade, Sebastian Fischetti, Donald Marolf, Simon F. Ross, and Moshe Rozali. Entanglement and correlations near extremality: CFTs dual to Reissner-Nordström $AdS_5$. *JHEP*, 04:023, 2014, arXiv:1312.2839.

[6] Elaheh Bakhshaei, Ali Mollabashi, and Ahmad Shirzad. Holographic subregion complexity for singular surfaces. *Eur. Phys. J. C*, 77(10):665, 2017, arXiv:1703.03469.

[7] Vijay Balasubramanian and Simon F. Ross. The dual of nothing. *Phys. Rev. D*, 66:086002, 2002, arXiv:hep-th/0205290.

[8] Vijay Balasubramanian, Borun D. Chowdhury, Bartłomiej Czech, and Jan de Boer. Entwinement and the emergence of spacetime. *JHEP*, 01:048, 2015, arXiv:1406.5859.

[9] Máximo Bañados, Marc Henneaux, Claudio Teitelboim, and Jorge Zanelli. Geometry of the 2+1 black hole. *Phys. Rev. D*, 48(4):1506–1525, 1993, arXiv:gr-qc/9302012.

[10] Tom Banks, Michael R. Douglas, Gary T. Horowitz, and Emil Martinec. AdS dynamics from conformal field theory. 1998, arXiv:hep-th/9808016.

[11] José L. F. Barbón and Eliezer Rabinovici. Holographic complexity and spacetime singularities. *JHEP*, 01:084, 2016, arXiv:1509.09291.

[12] Omer Ben-Ami and Dean Carmi. On volumes of subregions in holography and complexity. *JHEP*, 11:129, 2016, arXiv:1609.02514.

[13] David Berenstein and Antonio M. García-García. Universal quantum constraints on the butterfly effect. 2015, arXiv:1510.08870.

[14] Danny Birmingham and Massimiliano Rinaldi. Bubbles in anti-de Sitter space. *Phys. Lett. B*, 544:316–320, 2002, arXiv:hep-th/0205246.

[15] Luca Bombelli, Rabinder K. Koul, Joohan Lee, and Rafael D. Sorkin. Quantum source of entropy for black holes. *Phys. Rev. D*, 34(2):373–383, 1986.

[16] Dominic Brecher, Jianyang He, and Moshe Rozali. On charged black holes in anti-de Sitter space. *JHEP*, 04:004, 2005, arXiv:hep-th/0410214.

[17] Adam R. Brown, Daniel A. Roberts, Leonard Susskind, Brian Swingle, and Ying Zhao. Complexity, action, and black holes. *Phys. Rev. D*, 93:086006, 2016, arXiv:1512.04993.

[18] Adam R. Brown, Daniel A. Roberts, Leonard Susskind, Brian Swingle, and Ying Zhao. Holographic Complexity Equals Bulk Action? *Phys. Rev. Lett.*, 116: 191301, 2016, arXiv:1509.07876.

[19] Pasquale Calabrese and John Cardy. Entanglement entropy and quantum field theory. *J. Stat. Mech.*, 2004:P06002, 2004, arXiv:hep-th/0405152.

[20] Dean Carmi, Robert C. Myers, and Pratik Rath. Comments on holographic complexity. *JHEP*, 03:118, 2017, arXiv:1612.00433.

[21] Shira Chapman, Michal P. Heller, Hugo Marrochio, and Fernando Pastawski. Towards Complexity for Quantum Field Theory States. 2017, arXiv:1707.08582.

[22] Shira Chapman, Hugo Marrochio, and Robert C. Myers. Complexity of formation in holography. *JHEP*, 01:062, 2017, arXiv:1610.08063.

[23] Sebastian de Haro, Sergey N. Solodukhin, and Kostas Skenderis. Holographic Reconstruction of Spacetime and Renormalization in the AdS/CFT Correspondence. *Commun. Math. Phys.*, 217(3):595–622, 2001, arXiv:hep-th/0002230.

[24] Oliver DeWolfe. TASI Lectures on Applications of Gauge/Gravity Duality. 2018, arXiv:1802.08267.

[25] M. R. Dowling and M. A. Nielsen. The geometry of quantum computation. *Quantum Information and Computation*, 8(10):861–899, 2008, arXiv:quant-ph/0701004.

[26] Tevian Dray and Gerard 't Hooft. The gravitational shock wave of a massless particle. *Nucl. Phys. B*, B253:173–188, 1985.

[27] Netta Engelhardt and Aron C. Wall. Extremal surface barriers. *JHEP*, 03:068, 2014, arXiv:1312.3699.

[28] Charles Fefferman and C. Robin Graham. *The Ambient Metric*. Princeton University Press, 2012, arXiv:0710.0919.

[29] Lukasz Fidkowski, Veronika Hubeny, Matthew Kleban, and Stephen Shenker. The black hole singularity in AdS/CFT. *JHEP*, 02:014, 2004, arXiv:hep-th/0306170.

[30] C. Robin Graham and Edward Witten. Conformal anomaly of submanifold observables in AdS/CFT correspondence. *Nucl. Phys. B*, 546(1–2):52–64, 1999, arXiv:hep-th/9901021.

[31] S. S. Gubser, I. R. Klebanov, and A. M. Polyakov. Gauge theory correlators from non-critical string theory. *Phys. Lett. B*, 428(1–2):105–114, 1998, arXiv:hep-th/9802109.

[32] Rajan Gupta. Introduction to lattice QCD. 1998, arXiv:hep-lat/9807028.

[33] Guy Gur-Ari, Masanori Hanada, and Stephen H. Shenker. Chaos in classical D0-brane mechanics. *JHEP*, 02:091, 2016, arXiv:1512.00019.

[34] Thomas Hartman and Juan Maldacena. Time evolution of entanglement entropy from black hole interiors. *JHEP*, 05:014, 2013, arXiv:1303.1080.

[35] Sean A. Hartnoll. Lectures on holographic methods for condensed matter physics. *Class. Quant. Grav.*, 26:224002, 2009, arXiv:0903.3246.

[36] Patrick Hayden and John Preskill. Black holes as mirrors: quantum information in random subsystems. *JHEP*, 09:120, 2007, arXiv:0708.4025.

[37] Matthew Headrick. General properties of holographic entanglement entropy. *JHEP*, 03:85, 2014, arXiv:1312.6717.

[38] Gary T. Horowitz and Robert C. Myers. AdS-CFT correspondence and a new positive energy conjecture for general relativity. *Phys. Rev. D*, 59:026005, 1998, arXiv:hep-th/9808079.

[39] Veronika E. Hubeny. The AdS/CFT Correspondence. 2015, arXiv:1501.00007.

[40] Veronika E. Hubeny, Mukund Rangamani, and Tadashi Takayanagi. A covariant holographic entanglement entropy proposal. *JHEP*, 07:062, 2007, arXiv:0705.0016.

[41] W. Israel. Thermo-field dynamics of black holes. *Phys. Lett. A*, 57(2):107–110, 1976.

[42] Robert A. Jefferson and Robert C. Myers. Circuit complexity in quantum field theory. *JHEP*, 10:107, 2017, arXiv:1707.08570.

[43] Stephen P. Jordan, Keith S. M. Lee, and John Preskill. Quantum Algorithms for Fermionic Quantum Field Theories. 2014, arXiv:1404.7115.

[44] Igor R. Klebanov. TASI Lectures: Introduction to the AdS/CFT Correspondence. 2006, arXiv:hep-th/0009139.

[45] Nima Lashkari, Douglas Stanford, Matthew Hastings, Tobias Osborne, and Patrick Hayden. Towards the fast scrambling conjecture. *JHEP*, 04:022, 2013, arXiv:1111.6580.

[46] Luis Lehner, Robert C. Myers, Eric Poisson, and Rafael D. Sorkin. Gravitational action with null boundaries. *Phys. Rev. D*, 94:084046, 2016, arXiv:1609.00207.

[47] Stefan Leichenauer. Disrupting entanglement of black holes. *Phys. Rev. D*, 90: 046009, 2014, arXiv:1405.7365.

[48] Seth Lloyd. Ultimate physical limits to computation. *Nature*, 406:1047–1054, 2000.

[49] Jorma Louko, Donald Marolf, and Simon F. Ross. Geodesic propagators and black hole holography. *Phys. Rev. D*, 62:044041, 2000, arXiv:hep-th/0002111.

[50] Juan Maldacena. The Large-$N$ Limit of Superconformal Field Theories and Supergravity. *Int. J. Theor. Phys.*, 38(4):1113–1133, 1999, arXiv:hep-th/9711200. [*Adv. Theor. Math. Phys.*, 2(2):231–252, 1998].

[51] Juan Maldacena. Eternal black holes in anti-de Sitter. *JHEP*, 04:021, 2003, arXiv:hep-th/0106112.

[52] Juan Maldacena and Guilherme L. Pimentel. Entanglement entropy in de Sitter space. *JHEP*, 02:038, 2013, arXiv:1210.7244.

[53] Juan Maldacena and Leonard Susskind. Cool horizons for entangled black holes. *Fortsch. Phys.*, 61(9):781–811, 2013, arXiv:1306.0533.

[54] Juan Maldacena, Stephen H. Shenker, and Douglas Stanford. A bound on chaos. *JHEP*, 08:106, 2016, arXiv:1503.01409.

[55] Donald Marolf and Joseph Polchinski. Gauge-Gravity Duality and the Black Hole Interior. *Phys. Rev. Lett.*, 111:171301, 2013, arXiv:1307.4706.

[56] John McGreevy. Holographic duality with a view toward many-body physics. 2010, arXiv:0909.0518.

[57] Horaţiu Năstase. *Introduction to the AdS/CFT Correspondence*. Cambridge University Press, 2015.

[58] M. A. Nielsen. A geometric approach to quantum circuit lower bounds. *Quantum Information and Computation*, 6(3):213–262, 2006, arXiv:quant-ph/0502070.

[59] M. A. Nielsen, M. R. Dowling, M. Gu, and A. M. Doherty. Quantum computation as geometry. *Science*, 311:1133–1135, 2006, arXiv:quant-ph/0603161.

[60] Michael E. Peskin and Daniel V. Schroeder. *An Introduction to Quantum Field Theory*. Westview Press, 1995.

[61] Alfonso V. Ramallo. Introduction to the AdS/CFT correspondence. 2013, arXiv:1310.4319.

[62] Alan Reynolds and Simon F. Ross. Divergences in holographic complexity. *Class. Quant. Grav.*, 33:105004, 2017, arXiv:1612.05439.

[63] Alan P. Reynolds and Simon F. Ross. Butterflies with rotation and charge. *Class. Quant. Grav.*, 33:215008, 2016, arXiv:1604.04099.

[64] Alan P. Reynolds and Simon F. Ross. Complexity in de Sitter space. *Class. Quant. Grav.*, 34:175013, 2017, arXiv:1706.03788.

[65] Alan P. Reynolds and Simon F. Ross. Complexity of the AdS soliton. *Class. Quant. Grav.*, 35:095006, 2018, arXiv:1712.03732.

[66] Daniel A. Roberts and Douglas Stanford. Two-dimensional conformal field theory and the butterfly effect. *Phys. Rev. Lett.*, 115(13):131603, 2015, arXiv:1412.5123.

[67] Daniel A. Roberts and Brian Swingle. Lieb-Robinson Bound and the Butterfly Effect in Quantum Field Theories. *Phys. Rev. Lett.*, 117:091602, 2016, arXiv:1603.09298.

[68] Daniel A. Roberts, Douglas Stanford, and Leonard Susskind. Localized shocks. *JHEP*, 03:051, 2015, arXiv:1409.8180.

[69] Shinsei Ryu and Tadashi Takayanagi. Aspects of holographic entanglement entropy. *JHEP*, 08:045, 2006, arXiv:hep-th/0605073.

[70] Shinsei Ryu and Tadashi Takayanagi. Holographic Derivation of Entanglement Entropy from the anti-de Sitter Space/Conformal Field Theory Correspondence. *Phys. Rev. Lett.*, 96:181602, 2006, arXiv:hep-th/0603001.

[71] Yasuhiro Sekino and Leonard Susskind. Fast scramblers. *JHEP*, 10:065, 2008, arXiv:0808.2096.

[72] Stephen H. Shenker and Douglas Stanford. Black holes and the butterfly effect. *JHEP*, 03:067, 2014, arXiv:1306.0622.

[73] Stephen H. Shenker and Douglas Stanford. Multiple shocks. *JHEP*, 12:046, 2014, arXiv:1312.3296.

[74] Stephen H. Shenker and Douglas Stanford. Stringy effects in scrambling. *JHEP*, 05:132, 2015, arXiv:1412.6087.

[75] Nilanjan Sircar, Jacob Sonnenschein, and Walter Tangarife. Extending the scope of holographic mutual information and chaotic behavior. *JHEP*, 05:091, 2016, arXiv:1602.07307.

[76] Kostas Skenderis. Lecture notes on holographic renormalization. *Class. Quant. Grav.*, 19(22):5849–5876, 2002, arXiv:hep-th/0209067.

[77] Mark Srednicki. Entropy and Area. *Phys. Rev. Lett.*, 71(5):666–669, 1993, arXiv:hep-th/9303048.

[78] Douglas Stanford. Many-body chaos at weak coupling. *JHEP*, 10:009, 2016, arXiv:1512.07687.

[79] Douglas Stanford and Leonard Susskind. Complexity and shock wave geometries. *Phys. Rev. D*, 90:126007, 2014, arXiv:1406.2678.

[80] Leonard Susskind. Addendum to Fast Scramblers. 2011, arXiv:1101.6048.

[81] Leonard Susskind. Computational complexity and black hole horizons. *Fortsch. Phys.*, 64(1):24–43, 2016, arXiv:1403.5695.

[82] Leonard Susskind. Entanglement is not enough. *Fortsch. Phys.*, 64(1):49–71, 2016, arXiv:1411.0690.

[83] Leonard Susskind and Ying Zhao. Switchbacks and The Bridge to Nowhere. 2014, arXiv:1408.2823.

[84] Kenneth G. Wilson. Confinement of quarks. *Phys. Rev. D*, 10(8):2445–2459, 1974.

[85] Edward Witten. Anti de Sitter Space and Holography. *Adv. Theor. Math. Phys.*, 2(2):253–291, 1998, `arXiv:hep-th/9802150`.